Title
Investigating roles for prefrontal intemeurons in avoidance-related circuits

Author
Lee, Anthony

Publication Date
2017

Peer reviewed|Thesis/dissertation

Investigating roles for prefrontal interneurons in avoidance-related circuits

by

Anthony Lee

DISSERTATION

Submitted in partial satisfaction of the requirements for the degree of

DOCTOR OF PHILOSOPHY

in

Neuroscience

in the

GRADUATE DIVISION

of the

ACKNOWLEDGMENTS

I cannot overstate my gratitude for those that have supported me throughout the last 5 years of graduate school training. My family (mom, dad, sister) and friends provided strength when I felt weak, and labmates offered conviction when I felt lost. I cannot thank them enough. I would like to especially mention Tosha, Ian, Steven, Toby, Scott, Nick, and Celia. They made the lab feel like an extended family. Thank you for the memories.

In Chapter 2, I am grateful for Steven being a fun, patient teacher, and a willing, supportive co-author. You cannot find a better collaborator.

In Chapter 3, Daniel taught me how to clone and make viral constructs. He is the nicest scientist I personally know, and I cannot wait to hear how his new lab takes off.

In Chapter 4, Ian helped introduce photometry to the lab, and Francisco graciously offered MATLAB code for calcium imaging datasets. You will not find two more different people in one room.

Throughout my PhD, Vikaas has always been optimistic and patient. In the tumultuous times of every graduate school experience, it brings incredible comfort knowing that your advisor can be a constant.

And finally, I could not have finished graduate school the person I am without my wife, Shelley. Words escape how much she has meant to me, so I will best leave those indelible things unsaid.

ABSTRACT

How neurons in the mammalian brain give rise to complex behaviors is a fundamental challenge in neuroscience research. Circuits in the prefrontal cortex (PFC) direct higher-order cognitive and motivated behaviors such as decision-making and impulse control, and dysfunction of these circuits gives rise to neuropsychiatric disorders such as schizophrenia, anxiety disorders, and autism. Recent studies and new technologies have fueled a renaissance in understanding the function of these circuits by using neuronal subtypes as entry points into these circuits, but our knowledge of how these circuits function remains limited. In this dissertation, three studies are presented that advance new insights regarding the cellular connectivity, composition, and network information processing of subtypes of inhibitory neurons. In the first study, we examined how inhibition differs between projection-specific pyramidal neurons in layer 5 of PFC. Using in vitro patch-clamp electrophysiology and optogenetics, we found that subcortically-projecting pyramidal neurons receive significantly greater inhibition than callosally-projecting pyramidal neurons. This selective inhibition is likely attributed to increased inhibition from parvalbumin (PV) interneurons onto the subcortically-projecting pyramidal neurons, since optogenetic activation of another interneuron subtype, the somatostatin (SOM) interneuron, did not reveal differences in inhibition. In the second study, we challenged the definition that all inhibitory neurons are “interneurons”, that is that they only target neighboring neurons in the local circuit and do not form distant connections with neurons in other brain regions. Using transgenic mouse lines in combination with viral tracing and in vitro patch-clamp electrophysiology, we found a population of prefrontal inhibitory neurons with long-range projections distributed across many subcortical regions. These long-range inhibitory neurons are exclusively GABAergic and do not co-release excitatory glutamate. Furthermore, activation of

the LRG terminals in the nucleus accumbens resulted in acute avoidance behaviors, demonstrating that these neurons may be involved in influencing motivated behaviors. Our third study investigates roles for prefrontal VIP neurons in local and distributed anxiety networks. Fiber photometry of VIP neurons reflect increased activity in anxiogenic regions of the elevated plus maze (EPM) and inhibition of these neurons resulted in increased open arm exploration. Multi-site recordings of local field potentials showed that theta synchrony between ventral hippocampus (vHPC) and PFC was disrupted when prefrontal VIP neurons were inhibited. Finally, using combined optogenetic-endoscope imaging, we found that VIP neurons control the gain of anxiety-generated changes in prefrontal microcircuit activity. These findings highlight the specialized natures of interneuron subtypes in the mammalian brain, and provide evidence for how their microcircuit functions subserve complex behaviors.

TABLE OF CONTENTS

LIST OF FIGURES

1. Introduction

1.1 Roles of prefrontal cortex in behavior

The prefrontal cortex (PFC) of the mammalian brain is responsible for higher-order cognitive control and emotional processing. Our understanding of PFC function in humans is often popularly illustrated by Phineas Gage, the 19th century American railroad worker who destroyed much of his left frontal lobe when an iron rod completely penetrated through his skull. Following the accident, he assumed a completely different personality: more vulgar and impulsive, prone to indecision and vacillations between plans, an inability to attend or establish emotional "equilbrium." Yet Phineas Gage also survived with no apparent motor deficits (he walked away from the accident), exhibited no speech impediments, and possessed normal learning and memory (Demasio et al., 1994). Since the case study of Gage, numerous studies in animal models have confirmed that PFC deficits result in changes of "personality" – impairments of working memory, cognitive flexibility, and the processing of emotion (Shah and Treit, 2004; Kjelstrup et al., 2002). Accordingly, neuropsychiatric diseases such as autism, schizophrenia, anxiety disorders, and PTSD have all been attributed to dysfunction of PFC.

What endows the PFC with its wide-ranging functions may perhaps also be the biggest challenge to understanding how it works. Complexity is abound at all levels - cellular, circuit, and network. However, by focusing on characterizing the function of specific, individual neuronal subtypes, we may make advances in our understanding of PFC function. In this vein, I pursue three main questions in this dissertation: 1) Do pyramidal neurons form subtype-specific forms of excitation and inhibition? 2) Can we identify and characterize long-range GABAergic neurons in the PFC? 3) How do VIP neurons regulate anxiety-like behaviors in local and distributed networks?

1.2 Subtypes of excitatory and inhibitory neurons

Ever since the seminal findings from Ramon y Cajal, neuroscience has focused on characterizing the subtypes of neurons that comprise the "wiring diagram" of the circuit in a particular brain region. The average human brain is estimated to contain 100 billion neurons, each neuron forming thousands of downstream connections with nearby and distant partners. Thus, most attempts to dissect brain circuitry involve reducing the challenge to more manageable units - such as synaptic machinery, neurotransmitter function, or projection targets of neuronal subtypes. By simplifying the complexity to the level of neuronal subtypes, fundamental principles of brain organization and function may emerge.

Neurons can differ in many ways – neurotransmitter identity, laminar distribution, pre- and post-synaptic partners, intrinsic firing properties, neuromodulation, etc. At the most basic level, neurons can be divided into excitatory and inhibitory neurons, releasing glutamate and GABA, respectively. As their name suggests, excitatory neurons depolarize their post-synaptic partners, while inhibitory neurons hyperpolarize their targets. Furthermore, recent advances have highlighted an incredible diversity of GABAergic neurons, based on their morphology, electrophysiology properties, and/or characteristic histological markers. Using histological markers, three non-overlapping groups of interneurons have been identified: those that express parvalbumin (PV), somatostatin (SOM), and vasoactive intestinal peptide (VIP) proteins. Together, these three interneurons comprise ~80% of all interneurons in the cortex (Rudy et al., 2011), and have proven useful in demonstrating the utility of using neuronal subtypes as an "entry point" into complex neuronal circuits.

PV neurons, comprising 40% of cortical interneurons, migrate from the medial ganglionic eminence (MGE) during embryonic development and reside mainly in deeper cortical

layers, where they form inhibitory connections onto the somas and axon initial segments of pyramidal neurons (Rudy et al., 2011), Based on the subcellular targeting of their terminals, PV neurons are suggested to modulate the output of pyramidal neurons. Functionally, PV neurons are both necessary and sufficient for the generation of gamma oscillations (Cardin et al., 2009; Sohal et al., 2009), and dysfunction of these neurons has been linked to schizophrenia in humans and rodent models. SOM interneurons, comprising 30% of cortical interneurons, also develop and migrate from the MGE, but form connections onto distal dendrites of neurons, suggesting that they may regulate how pyramidal neurons receive inputs. VIP interneurons, comprising 12% of cortical interneurons, migrate from the caudal ganglionic eminence and form inhibitory connections onto other interneurons, forming unique disinhibitory circuits that have been shown to mediate long-term inputs onto distant circuits (Pi et al., 2013; Lee et al., 2013).

Similar to how inhibitory neurons can be classified into neuronal subtypes, there is also present a diversity of excitatory neurons. Classification based on local and distant inputs and outputs, intrinsic firing properties, transcription factor expression, and laminar specification can unmask many categories of excitatory neurons (Harris and Shepherd, 2015). For example, recent work has identified at least two subtypes of layer 5 pyramidal neurons in the PFC – those that project subcortically (Type A) vs callosally (Type B) (Gee et al., 2012; Seong and Carter, 2012). These pyramidal neurons differ not only in their anatomy, but also have different compositions of dopamine receptors and intrinsic electrophysiological properties. Type A neurons display thick-tufted dendritic shafts, contain strong Ih current, and express D2-receptors.

Characterizing how the different subtypes of excitatory and inhibitory neurons behave in isolation, and as part of the larger circuit, will be essential to further our understanding of mPFC function. Despite these recent advances in describing subtypes of neurons, much remains

unknown. For example, how do these subtypes of excitatory and inhibitory neurons modulate each other – is there an underlying logic or are their connections stochastic? Are inhibitory neurons limited to only synapses onto local neurons? Do these neuronal subtypes differ in how they process local vs distant inputs? This dissertation attempts to partly address each of these specific questions. In Chapter 2, I look at whether the two identified pyramidal neurons – Type A and B – receive subtype-specific forms of excitation and inhibition. In Chapter 3, I examine whether all cortical GABAergic neurons are only "interneurons" and only connections to local excitatory neurons. In Chapter 4, I focus on potential roles of VIP neurons in regulating anxiety circuits.

1.3 Anatomy of mPFC circuitry

The rodent medial prefrontal cortex (mPFC) can be divided into prelimbic (PL) and infralimbic (IL) regions. Although the homologies of rodent and human mPFC are often debated, recent work using comparative projection mapping between rodent and non-human primates suggest that PL and IL may be analogous to NHP a32 and a25, respectively (Heilbronner et al., 2016). Based on their afferent and efferent topography, the PL region is believed to participate in executing cognitive functions (e.g. working memory), whereas the IL is believed to influence visceromotor activities (e.g. anxiety). There is a general gradient along the dorsalventral axis of the PFC from primarily sensorimotor inputs to more limbic inputs (Hoover and Vertes, 2007). The main sources of afferent projections to mPFC are from the orbitomedial prefrontal, insular, and entorhinal cortices, the ventral hippocampus, amygdala, the mediadorsal thalamus and monoaminergic nuclei of the brainstem (Hoover and Vertes, 2007). Besides the major efferent projection to medialdorsal thalamus, mPFC targets include the lateral septum, olfactory tubercle, basal forebrain, nucleus accumbens, subregions of the amygdala, hypothalamus, and raphe nuclei

of brainstem (Cite Vertes 2003). Clear inferences regarding the functions of these subregions based on their synaptics projections are complicated, however, by numerous reciprocal connections between PL and IL (Gabbott et al., 2003), and these subregions may play antagonistic roles by synapsing onto subtype-specific neurons with opposing functions in downstream circuits (Sierra Mercado, Padilla-Coreano, and Quirk, 2011).

Both PL and IL are heterotypic cortices that contain four layers: I, II/III, V, VI (from superficial to deep). Although the layer specificity of efferent projections vary slightly depending on the origin of the projection (Little and Carter, 2012), it is believed that layer V and VI neurons comprise the principal output neurons of the mPFC microcircuit. Furthermore, the characteristic laminar distribution and physiological properties of cortical interneurons is largely similar compared to that of homotypic cortex found in the neocortex (Pi et al., 2013). Thus, VIP neurons are largely confined to superficial layers I and II/III and inhibit other SOM cells, whereas PV and SOM neurons reside mainly in layers II/III to VI and inhibit the soma and distal dendrites, respectively (Lee et al., 2010).

In Chapter 2 of this dissertation, I restrict the investigation of subtype-specific excitation and inhibition onto layer V neurons. In Chapter 3, I characterize the projection targets of prefrontal long-range GABAergic neurons across widespread subcortical brain regions and demonstrate the in vivo effects of stimulating these projects in the NAcc. In Chapter 4, I look at the layer II/III VIP neurons and attempt to uncover how inhibition of these neurons affects processing of vHPC inputs.

1.4 Prefrontal networks involved in innate, motivated behaviors

Because of its anatomical hub and the various behavioral manifestations arising from its dysfunction, the mPFC is proposed to engage in “top-down” control of various sub-cortically

driven processes. In particular, the mPFC is involved in both reward-seeking and anxiety-like behaviors.

The circuitry for reward-seeking behaviors centers on the well-supported roles of the nucleus accumbens (NAcc), where dopaminergic reinforcement signals are integrated with inputs containing environmental or contextual cues to induce synaptic plasticity of motor outputs (Britt et al., 2012). Drug addiction is believed to be a pathological association of drug reinforcement and environmental cues (Kauer and Malenka, 2007). Because of its major projections to the NAcc, the mPFC has been proposed to impart executive control on these reward-seeking behaviors. Indeed, inhibition of rat PL reduces reinstatement of drug-seeking behavior, while silencing rat IL inhibits cocaine-seeking in extinguished rats (cite Peters et Kalivas, 2008).

Beyond the well-documented findings of the basolateral amygdala (BLA) in fear expression, the mPFC and ventral hippocampus (vHPC) also play key roles in regulating anxiety-like behavior. Lesions of mPFC and vHPC are anxiolytic in the elevated plus maze (EPM) (Kjelstrup et al., 2002; Shah and Treit, 2003). In particular, theta synchrony seems to be crucial in conveying anxiogenic information from the vHPC to mPFC since inhibiting vHPC inputs is both anxiolytic and disrupts theta synchrony (Padilla-Coreano et al., 2016).

In Chapter 3, I purpose that acute activation of prefrontal GABAergic terminals in the NAcc may elicit avoidance behaviors. In Chapter 4, I examine how inhibiting prefrontal VIP neurons disrupts theta synchrony between vHPC and mPFC and results in anxiolytic behavior.

2. Subtype-specific forms of excitation and inhibition onto prefrontal pyramidal neurons

2.1 Abstract

Layer 5 pyramidal neurons comprise at least two subtypes: thick-tufted, subcortically-projecting Type A neurons, with prominent h-current, and thin-tufted, callosally-projecting Type B neurons, which lack prominent h-current. Using optogenetic stimulation, we find that these subtypes receive distinct forms of input that could subserve divergent functions. Repeatedly stimulating callosal inputs evokes progressively smaller excitatory responses in Type B but not Type A neurons. Callosal inputs also elicit more spikes in Type A neurons. Surprisingly, these effects arise via distinct mechanisms. Differences in the dynamics of excitatory responses reflect differences in presynaptic input, whereas differences in spiking depend on postsynaptic mechanisms. We also find that fast-spiking parvalbumin interneurons, but not somatostatin interneurons, preferentially inhibit Type A neurons, which leads to greater feedforward inhibition in this subtype. These differences may enable Type A neurons to detect salient inputs that are focused in space and time, while Type B neurons integrate across these dimensions.

2.2 Introduction

Patterns of network activity emerge from the organization of connections in neural circuits. Thus, it is critically important to determine whether these connections follow a specific wiring diagram, and if so, to identify possible computational functions that emerge as a result. Many studies have shown that across multiple neocortical regions, layer 5 (L5) pyramidal neurons can be divided into at least two subtypes (Brown and Hestrin, 2009; Dembrow et al., 2010; Gee et al., 2012; Hattox and Nelson, 2007; Morishima and Kawaguchi, 2006; Seong and Carter, 2012; Sheets et al., 2011; Wang et al., 2006). One subtype, which we call "Type A" neurons, has thick-tufted apical dendrites, projects subcortically, and has a prominent h-current (I_h). The other subtype – "Type B neurons" – projects to the contralateral cortex or striatum, has thin tufted apical dendrites, and lacks prominent I_h.

Several groups have studied differences in local connections between these two subtypes (Brown and Hestrin, 2009; Morishima and Kawaguchi, 2006; Morishima et al., 2011; Wang et al., 2006). However, it remains unknown whether long-range excitatory inputs or local inhibitory connections also differ between these subtypes. Two recent studies found that neocortical interneurons nonspecifically target nearby pyramidal neurons (Fino and Yuste, 2011; Packer and Yuste, 2011) but these studies did not examine subtypes of L5 pyramidal neurons. By contrast, studies in other regions suggest that inhibitory interneurons can selectively innervate pyramidal neurons that project to specific targets, while sparing neighboring pyramidal neurons that project elsewhere (Krook-Magnuson et al., 2012; Varga et al., 2010).

To address these issues, we studied excitatory connections from the contralateral mPFC, and inhibitory connections from fast-spiking parvalbumin interneurons (FSINs) and somatostatin (SOM) interneurons onto Type A and B neurons in mPFC. We find that optogenetic stimulation

of callosal inputs elicits distinct patterns of responses in Type A and B neurons and that FSINs preferentially innervate Type A neurons. These findings have important implications for the normal and pathological function of prefrontal microcircuits.

2.3 Methods

2.3.1 Slice preparation

Slice preparation and intracellular recording followed our published protocol (Sohal and Huguenard, 2005). We cut 250 μm coronal slices from 8- to 11-week-old mice of either sex. Slices were cut in a chilled slicing solution in which Na^+ was replaced y sucrose, then incubated in warmed ACSF at 30-31 degC for at least one hour before being used for recordings. ACSF contained (in mM): 126 NaCl, 26 $NaHCO_3$, 2.5 KCl, 1.25 NaH_2PO_4, 1 $MgCl_2$, 2 CaCl, and 10 glucose. We used the following mouse lines: wild-type C57BL/6 mice (Charles River) and B6;129P2-*Pvalbtm1(cre)Arbr*/J (line 008069; www.jaxmice.jax.org). We secured the slice by placing a harp along the midline between the two hemispheres.

2.3.2 Intracellular recording

We obtained somatic whole-cell patch recordings from visually identified pyramidal cells in layer V of infralimbic or prelimbic cortex using differential contrast video microscopy on an upright microscope (BX51WI; Olympus). Recordings were made using a Multiclamp 700A (Molecular Devices). Except when otherwise noted, patch electrodes (tip resistance = 2–6 MOhms) were filled with the following (in mM): 130 K-gluconate, 10 KCl, 10 HEPES, 10 EGTA, 2 MgCl, 2 MgATP, and 0.3 NaGTP (pH adjusted to 7.3 with KOH). All recordings were

at 32.5±1°C. Series resistance was usually 10–20 MΩ, and experiments were discontinued above 30 MΩ.

2.3.3 Injection of virus for ChR2 or EYFP expression

For Cre-dependent expression of ChR2 or EFYP, we used a previously described adeno-associated virus (AAV) vector that drives Cre-dependent expression of a ChR2-EFYP fusion protein (Sohal et al., 2009). In other cases, we expressed ChR2-EFYP in pyramidal neurons using a previously described AAV vector that contains a gene encoding ChR2-EYFP under control of the promoter for CaMKIIα (Yizhar et al., 2011). In each case, we injected 0.5– 0.75 µl of virus following previously described procedures (Sohal et al., 2009). For experiments in which we recorded from ChR2-negative neurons while stimulating ChR2-positive axons, we injected virus into the contralateral medial PFC (mPFC), and verified that we observed fluorescent soma on the injected side, but not on the contralateral side (which was the location for recording). For experiments where we recorded from pyramidal neuron-interneuron pairs, we injected Cre-dependent ChR2-EYFP virus into ipsilateral mPFC. We waited at least 4 weeks after virus injection before preparing brain slices. Coordinates for injection into mPFC were (in millimeters relative to bregma): 1.7 anterior-posterior (AP), 0.3 mediolateral (ML), and -2.75 dorsoventral (DV).

2.3.4 Injection of retrogradely transported microspheres for projection targeting experiments

Procedures for injection of these microspheres were similar to those for virus injection. We waited at least 48 h after each injection before preparing brain slices. Coordinates for mPFC injections were the same as for virus injections. For injections into mediodorsal (MD) thalamus,

coordinates were (in millimeters relative to bregma): +1.7 AP, 0.3 ML, and -3.5 DV. For each experiment, we verified that microspheres were present in the correct target (MD thalamus or mPFC). For injections into MD thalamus we specifically verified that microspheres were not present in nearby structures (e.g., striatum).

2.3.5 Electrophysiologic identification of Type A and B neurons

Type A neurons were distinguished from Type B neurons by their voltage sag and rebound afterdepolarization following hyperpolarizing current pulses, as well as their prominent afterhyperolarization (AHP) following depolarizing current pulses. The voltage sag was determined by the difference between the minimum and steady state membrane potential during a hyperpolarizing current pulse (-200 pA, 250 msec). The rebound afterdepolarization the amount by which the membrane potential overshot the baseline value immediately following this current pulse. Similarly, the AHP was the difference between the minimum membrane potential following a depolarization current pulse (250 pA, 250 msec) and the baseline value. Type A neurons were defined strictly as cells with combined sag, rebound, and afterhyperpolarization greater than 6.5 mV.

2.3.6 Electrophysiologic identification of fast spiking interneurons

Fast-spiking interneurons were first preliminarily identified through an AAV-Dlxi12b enhancer-mCherry. This enhancer element marks a diverse population of interneuron subtypes (Potter et al., 2009). All putative interneurons were then identified as fast-spiking interneurons based on electrophysiological properties. Specifically, the action potential halfwidth was ≤ 0.5 msec, and

during responses to a depolarizing current pulse (400 pA, 250 msec), the ratio between the first and last interspike interval was < 2.

2.3.7 Drug application

For electrophysiology, all drugs were dissolved in water (DL-AP5, 4AP, bicuculline methiodide) or dimethylsulfoxide (mibefradil, nimodipine, nickel) before being diluted in ACSF, except for tetrodotoxin (TTX) which was dissolved in a pH 4.8 citrate buffer.

2.3.8 ChR2 stimulation

We stimulated ChR2 in pyramidal neurons using ~2mW flashes of light generated by a Lambda DG-4 high-speed optical switch with a 300W Xenon lamp (Sutter Instruments), and an excitation filter set centered around 470 nm, delivered to the slice through a 40x objective (Olympus). Illumination was delivered across a full high-power (40x) field.

2.3.9 Integrate and fire simulations

We first constructed a model for the short term dynamics of callosal inputs to Type A or B neurons, based on our voltage-clamp recordings of EPSCs to these two pyramidal neuron subtypes. For Type A inputs, the strength of a particular input fiber underwent slight facilitation after each input pulse according to the following equation:

$$s = \left(s_0 + \alpha_{fac}\right) e^{-(t-t_0)/\tau_{fac}}$$

where the relative synaptic strength at time t is $1 + s$, t_0 is the time of the last pulse on this fiber, s_0 is amount of facilitation at that time, α_{fac} represents the amount of facilitation, and τ_{fac} represents the time constant for facilitation. By selecting values of α_{fac} and τ_{fac} which best fit the

averaged voltage clamp recordings from Type A neurons, we obtained α_{fac} = 0.9 and τ_{fac} = 100 msec. Similarly, for Type B inputs, the strength of a particular input fiber underwent depression after each input pulse according to the equation:

$$s = \left(s_0 - \alpha_{dep}(1 - s_0)\right) e^{-(t-t_0)/\tau_{dep}}$$

where the relative synaptic strength at time t is 1 - s, t_0 is the time of the last pulse on this fiber, s_0 is amount of depression at that time, α_{dep} represents the amount of depression, and τ_{dep} represents the time constant for depression. By selecting values of α_{dep} and τ_{dep} which best fit the averaged voltage clamp recordings from Type B neurons, we obtained α_{dep} = 0.3 and τ_{dep} = 425 msec.

The integrate and fire simulations used a timestep of 0.1 msec. Simulated neurons had an input resistance of 150 MΩ, capacitance of 100 pF, spiking threshold of 15 mV, and reset potential of -10 mV (all voltages are relative to rest). Each EPSC had a rise time of 2 msec, decay time constant of 6 msec, conductance of 5 nS, and reversed at 70 mV (again relative to rest). In addition, to incorporate noise, we multiplied the amplitude of each EPSC by a pseudorandom value drawn from a normal distribution with a mean of 1 and standard deviation of 0.2.

2.3.10 Statistical analysis

We used Student's t-tests to compare pairs of groups, unless there were repeated measurements or more than 2 groups, in which case we used ANOVA. In one case, as noted in the text, we used the chi-squared test to compare the frequency of connections between two groups. Error bars indicate ± 1 SEM unless otherwise specified.

2.4 Results

To compare responses of Type A and B neurons to callosal inputs, we performed dual whole cell recordings in pairs of Type A and B neurons while optogenetically stimulating inputs from the contralateral mPFC (n=11 pairs; Fig. 2.1). We differentiated Type A and B neurons by the prominence of the I_h induced sag and rebound in response to hyperpolarizing current pulses and the presence of an afterhyperpolarization following depolarizing current pulses (Methods; Fig. 2.2A) (Gee et al., 2012). We expressed ChR2 in pyramidal neurons in the mPFC in one hemisphere (Methods; Fig. 2.1A), then stimulated the terminals of their callosal projections via rhythmic trains of light flashes (470nm; ~2 mW/mm^2, 5ms; 5 or 10 Hz, 10 flashes/train). Some studies optogenetically stimulate terminals in TTX + 4-AP to block polysynaptic activity (Petreanu et al., 2007). However, in TTX + 4-AP, synaptic release is triggered by the ChR2-driven depolarization of terminals rather than by spiking. This would not be suitable for studying the short-term dynamics of synaptic responses, therefore, by design, we did not use TTX + 4-AP to block polysynaptic activity. This also enabled us to measure how callosal inputs recruit different levels of spiking and feedforward inhibition in Type A and B neurons. We did attempt experiments using TTX + 4-AP, but found that optogenetically-evoked synaptic release was completely abolished (6/6 neurons; Fig. 2.2B), indicating that, in our preparation, optogenetically-evoked synaptic release is mediated by spiking. Although we could not use TTX + 4-AP to isolate monosynaptic responses, several observations described below suggest that

monosynaptic callosal input dominated the responses we recorded.

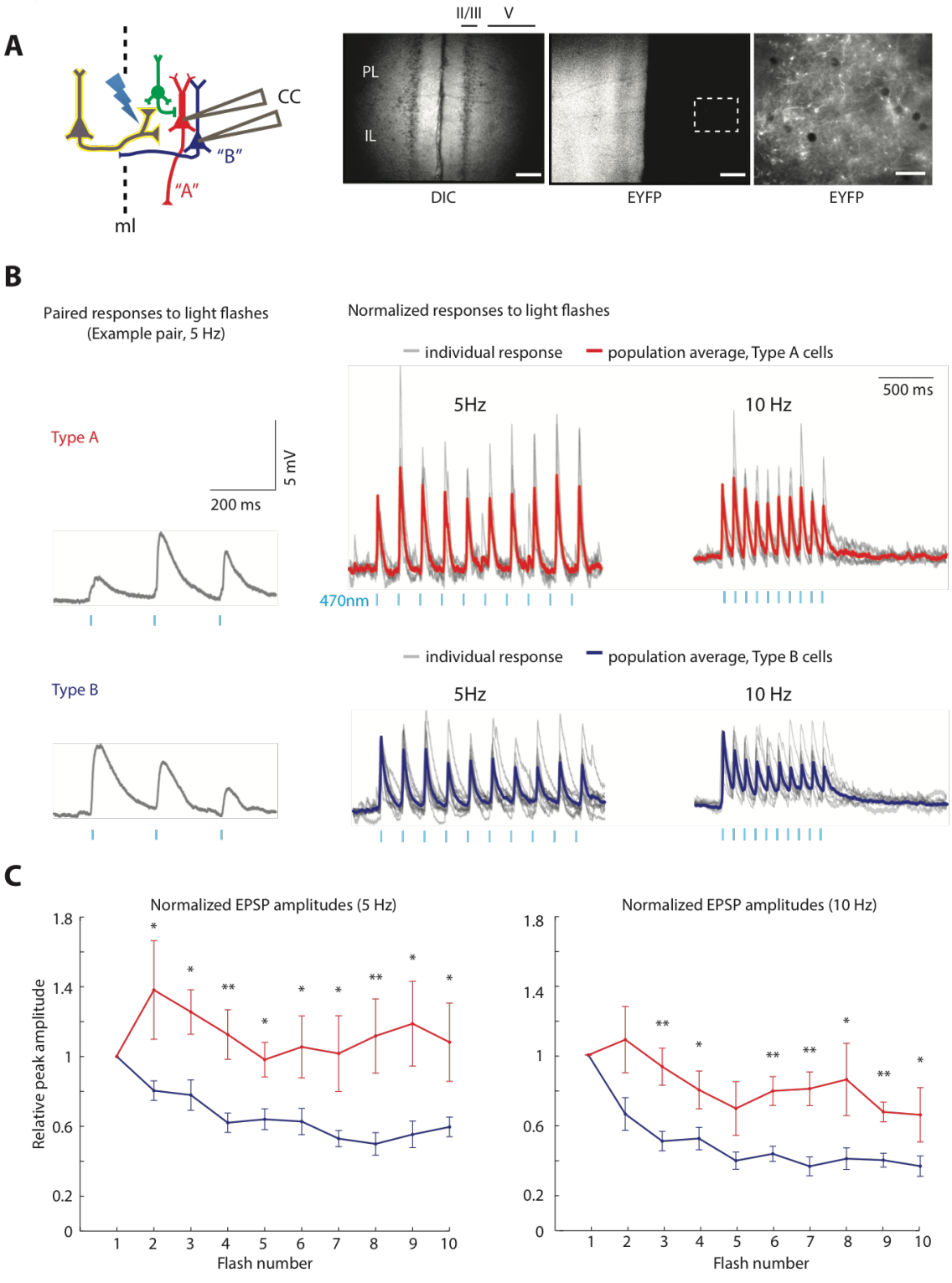

Figure 2.1. EPSP dynamics differ across subtypes of L5 pyramidal neurons.

(A) Experimental design: we simultaneously recorded from a Type A (red) and Type B (blue) pyramidal neuron while activating ChR2-expressing inputs (yellow) from the contralateral mPFC. Low-power images of mPFC, including the prelimbic and infralimbic cortices (PL and IL), showing a DIC image (left) and ChR2-EYFP expression (middle) (scale bar=50 μm). Right: High-power image of the dotted region in the middle panel, showing ChR2-EYFP expression in axon terminals from the contralateral mPFC (scale bar=12.5 μm). **(B)** Paired responses of Type A and B neurons to 5 Hz light stimulation in current clamp (left). Population average (bold) and individual (gray) current clamp responses to 5 Hz (middle) and 10 Hz (right) stimulation. **(C)** Normalized EPSP amplitudes during trains of light flashes in Type A and B neurons with subthreshold responses (n=8/11 pairs). *=$p<0.05$, **=$p<0.01$. See also Fig. 2.2.

2.4.1 Callosal stimulation elicits subtype-specific excitatory responses

Trains of optogenetic stimulation delivered to callosal inputs elicited EPSPs in Type A/B pairs. In 3/11 pairs, at least one cell spiked. In the remaining 8 pairs, all EPSPs were subthreshold. Notably, the pattern of subthreshold EPSPs differed in Type A and B neurons (Fig. 2.1B). We observed marked depression of subthreshold EPSP responses to successive light flashes in Type B neurons, i.e. the responses to light flashes 2-10 were consistently weaker than the first response ($p<0.001$ for an effect of response number on EPSP amplitude by ANOVA; EPSPs 2-10 were each weaker than the first EPSP, $p<0.05$ by t-test; n=8 cells). No such depression occurred in Type A neurons, and normalized EPSP responses to light flashes 2-10 were significantly greater in Type A than Type B neurons ($p<10^{-4}$ for 5 Hz, $p<0.01$ for 10 Hz via ANOVA using cell subtype, recording pair, and flash number as factors; n=8 pairs; Fig. 2.1C). In fact, in some Type A neurons, the first few responses to light flashes at 5 Hz were facilitating, i.e. they grew progressively larger (gray traces in Fig. 2.1B). The average amplitude of the first

EPSP was not significantly different in Type A and B neurons ($p=0.18$ for 5 Hz; $p=0.41$ for 10 Hz; $n=8$ pairs). To confirm that Type A and B neurons have different projection targets, we also made recordings after injecting fluorescent retrogradely transported microspheres (Lumafluor) into MD thalamus (red) and contralateral mPFC (green). In 3/3 pairs consisting of one corticothalamic (CT) and one corticocortical (CC) neuron, we observed the same pattern – strong depression of EPSPs in CC (Type B) neurons but not in CT (Type A) neurons (Fig. 2.2D-F).

Subtype-specific patterns of EPSPs could reflect differences in monosynaptic callosal inputs, or effects of polysynaptic activity. Three observations suggest that these differences arise at the level of monosynaptic callosal inputs. First, in all of the recordings used to analyze EPSPs, callosal stimulation failed to evoke spikes in either simultaneously recorded neuron, suggesting that in these recordings polysynaptic activity was limited. If one considers *all* recordings, including those in which we observed spiking, then on average, each neuron spikes in response to a light flash 7.5% of the time (there were 33 spikes in response to 440 light flashes, based on 22 cells, 2 sweeps per cell, and 10 light flashes per sweep). Of course, such an average obscures the fact that due to variable ChR2 expression across slices, a few experiments contained high levels of spiking while others contained minimal polysynaptic activity. Indeed, in 3 recordings, light stimulation failed to evoke appreciable inhibitory currents in either cell (measured in voltage clamp at +10 mV). These recordings presumably represent cases with the least ChR2 expression and minimal polysynaptic activity, but they still exhibit EPSP depression in Type B but not Type A neurons (Fig. 2.2C). This represents a second line of evidence that differences in EPSPs arise at the level of monosynaptic inputs.

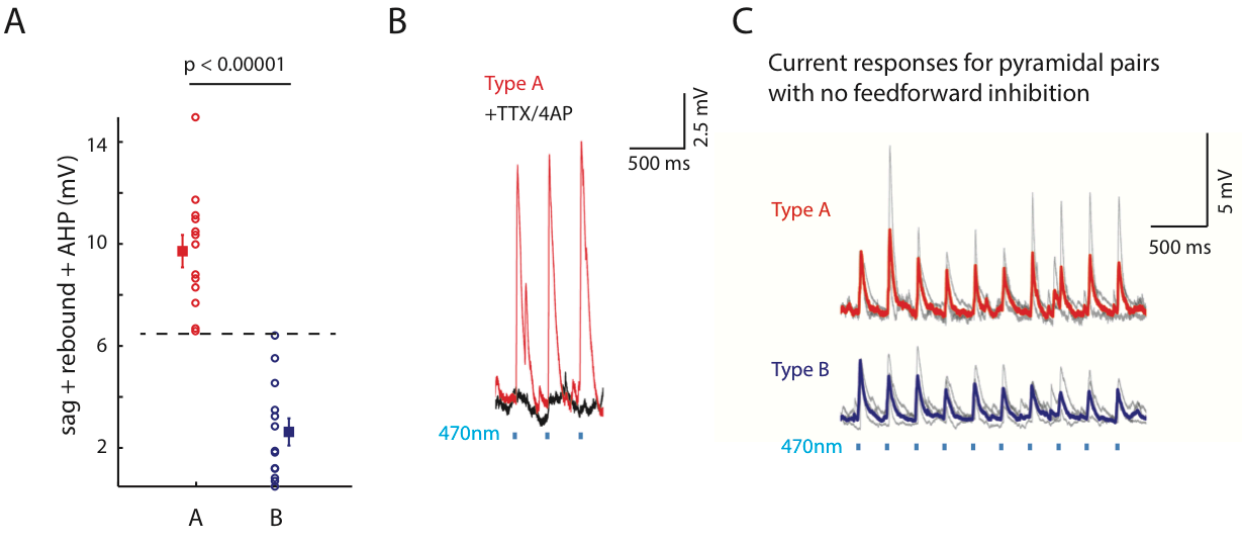

D

Dual-patch projection-specific layer V mPFC pyramidal cells.
Retrobeads injected into MD thalamus (green) and contralateral PFC (red)

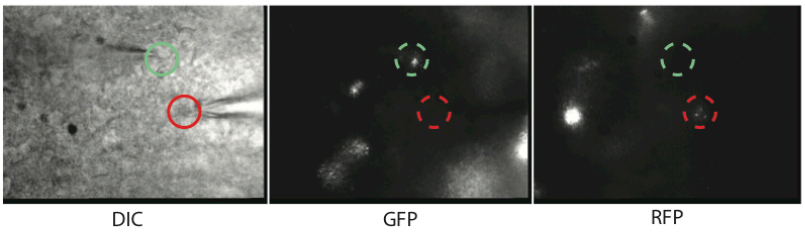

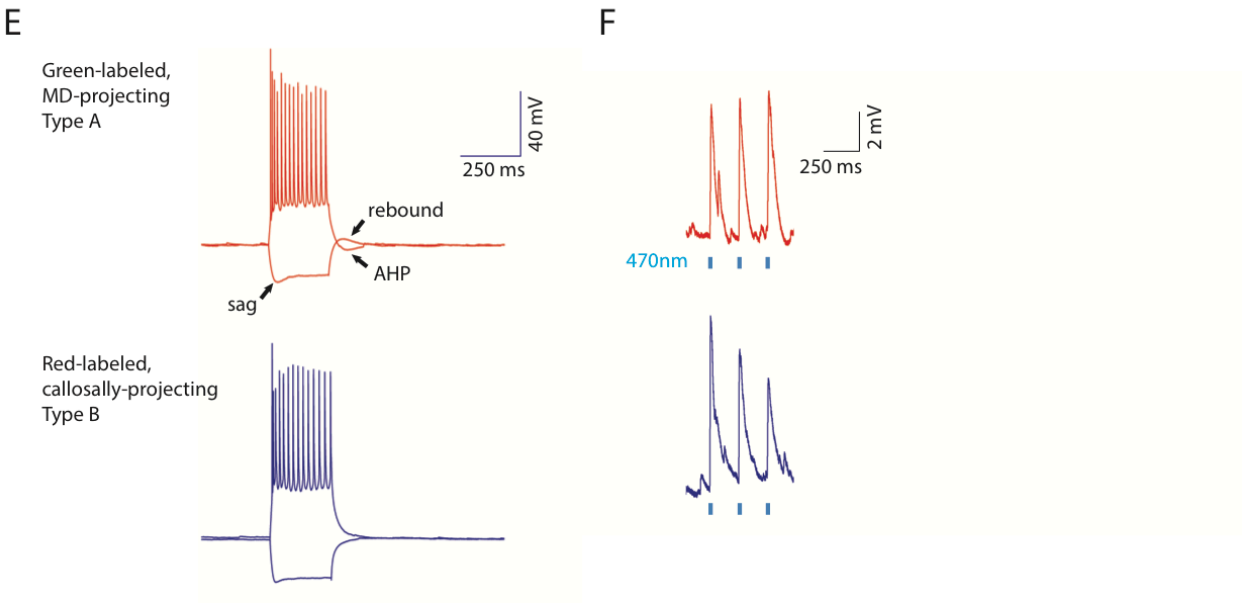

Figure 2.2. Classification of Type A and B neurons, and differences between callosal EPSPs in Type A and B neurons

(A) Classification of Type A and Type B neurons based on a combination of the sag and rebound in response to a -250 pA pulse, and the afterhyperolarization (AHP) following a +250pA current pulse. Type A neurons were classified as cells with combined values >6.5 mV (dotted line). **(B)** Application of TTX and 4-AP eliminates excitatory responses to optogenetic stimulation of callosal projections. **(C)** EPSP dynamics in simultaneously recorded Type A and B neurons in cases that failed to evoke circuit inhibition (n = 3 pairs). These experiments have a similar latency to EPSP peak as our other experiments (15.4 ± 2.1 msec in these experiments, compared to 13.8 ± 1.8 msec in our complete dataset; p = 0.64). In these experiments, the difference between the pattern of EPSPs in Type A and B neurons was also similar to our other experiments. Specifically, the ratio between the second and first response was 1.57 ± 0.57 in Type A cells, and 0.77 ± 0.13 and in Type B cells, compared to 1.25 ± 0.18 and 0.78 ± 0.15 respectively in our complete dataset**. (D)** Representative image of Type A (green) and Type B (red) neurons labeled with retrogradely transported fluorescent microspheres injected into the MD thalamus (red) and contralateral mPFC (green), respectively. **(E)** Current clamp responses of labeled Type A (coticothalamic, CT) and B (cortiocallosal, CC) neurons to injection of -250pA. **(F)** Optogenetic stimulation of callosal inputs elicit depressing EPSPs in labeled Type B (CC) neurons, but not in labeled Type A (CT) neurons.

Finally, even when we did observe spiking (in current clamp), these spikes occurred 11.3 ± 1.7 msec after the light flash – well *after* the peak of the EPSC response, measured in voltage clamp (7.3 ± 0.5 msec after the light flash; n=6 cells). Thus, peak responses are likely to be dominated by monosynaptic input (though polysynaptic activity may also contribute). In summary, multiple factors suggest that differences in EPSP dynamics originate at the level of monosynaptic callosal inputs. Regardless, we have found that callosal inputs recruit distinct patterns of excitation in Type A and B neurons.

2.4.2 Differences in presynaptic input explain subtype-specific differences in EPSPs

We next asked whether the different EPSP dynamics in Type A and B neurons reflect pre- or postsynaptic mechanisms. When dual-patching onto A/B pairs in voltage clamp at -70 mV (Fig. 2.3A, top), we did not find significant differences in peak excitatory currents or charge transfer (Fig. 2.3B). Normalized, averaged excitatory currents elicited by light stimulation show that Type A or B neurons receive slightly facilitating or depressing currents, respectively (Fig. 2.3C). We asked whether these facilitating and depressing currents suffice to reproduce the subtype-specific EPSP patterns in Fig. 2.1. This would suggest that subtype-specific patterns of presynaptic input account for differences in EPSP dynamics. Alternatively, different postsynaptic properties of Type A and B neurons, e.g. differences in resonance properties (Dembrow et al., 2010), may contribute to different EPSP responses. To address this, we averaged the input waveform recorded in voltage clamp from Type A neurons, and the waveform recorded from Type B neurons (Fig. 2.3C). Then we played back each waveform to both Type A and B neurons in current clamp (Fig. 2.3D). If cell-intrinsic properties contribute to differences in EPSP dynamics, voltage responses to the injected inputs should depend on the identity of the patched neuron (A or B). However, the response of Type A and B neurons depended only on the identity of the injected current waveform (Fig. 2.3E). Both Type A and B neurons showed EPSP depression in response to the “Type B” input waveform but not the “Type A” waveform (Fig. 2.3F).

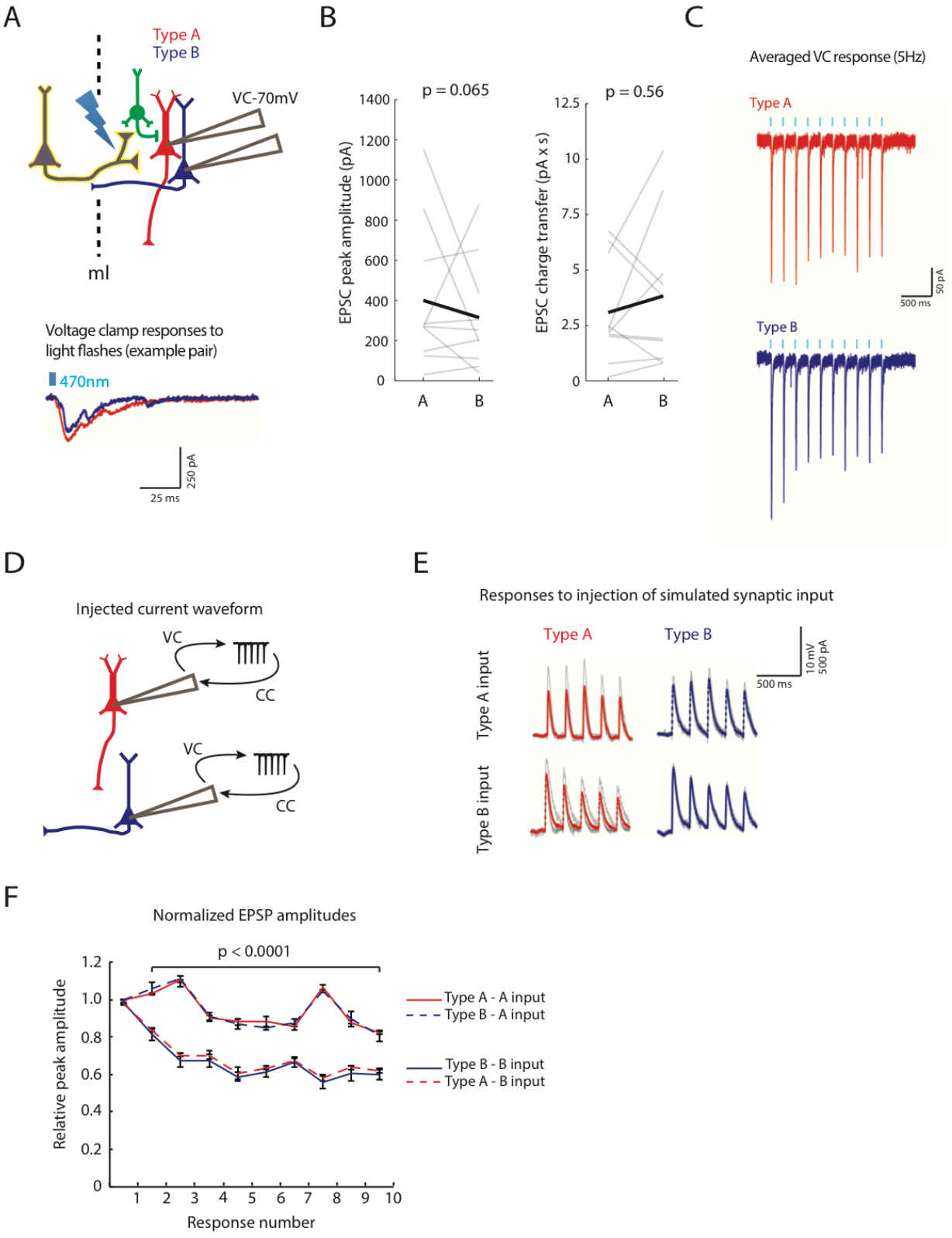
A
Type A
Type B
VC-70mV
ml
Voltage clamp responses to
light flashes (example pair)
470nm
250 pA
25 ms
B
p = 0.065
EPSC peak amplitude (pA)
1400
1200
1000
800
600
400
200
0
A
B
p = 0.56
EPSC charge transfer (pA x s)
12.5
10
7.5
5
2.5
0
A
B
C
Averaged VC response (5Hz)
Type A
50 pA
500 ms
Type B
D
Injected current waveform
VC
CC
VC
CC
E
Responses to injection of simulated synaptic input
Type A
Type B
10 mV
500 pA
500 ms
Type A input
Type B input
F
Normalized EPSP amplitudes
p < 0.0001
Relative peak amplitude
1.2
1.0
0.8
0.6
0.4
0.2
0
1
2
3
4
5
6
7
8
9
10
Response number
Type A - A input
Type B - A input
Type B - B input
Type A - B input

Figure 2.3. Subtype-specific synaptic responses in L5 pyramidal cells depend on presynaptic inputs.

(A) Top: simultaneous recordings were made from Type A (red) and B (blue) neurons in voltage clamp at -70 mV while optogenetically stimulating callosal inputs (yellow). Example voltage traces from a Type A/B pair (bottom). **(B)** EPSC peak amplitude (left) and charge transfer (right) for each cell type**. (C)** Normalized, averaged voltage clamp responses to 5 Hz light stimulation in Type A (red) and B (blue) neurons (n=11 pairs). **(D)** Normalized, averaged voltage clamp responses of Type A and B neurons to callosal input were played back in current clamp to Type A or B neurons. **(E)** Population (bold) and individual (gray) current clamp responses to these averaged waveforms representing callosal inputs to either Type A or B neurons. **(F)** Normalized EPSP amplitudes in response to injection of Type A or B waveforms (n=4 for each condition). See also Fig. 2.4.

Of course, the current waveforms we recorded in voltage clamp may not accurately reflect synaptic input. These waveforms could be contaminated by unclamped dendritic currents in Type A and B neurons, and such voltage-dependent Ca^{2+} currents in the dendrites might enhance temporal summation between EPSPs in Type A neurons, masking the sort of EPSP depression observed in Type B neurons (Branco and Hausser, 2011; Schiller et al., 2000). To rule this out, we recorded Type A neuron responses to callosal stimulation before and after blocking T-type Ca^{2+} channels, L-type Ca^{2+} channels, and NMDARs with mibefradil (5 μM) + nimodipine (5 μM) + AP5 (50 μM). We found no alteration in the paired-pulse ratio after blocking these postsynaptic voltage-dependent Ca^{2+} channels ($p=0.19$, n=4, Fig. 2.4), i.e. even after blocking these channels, EPSPs in Type A neurons were still non-depressing. This suggests that differences between the pattern of callosally-evoked EPSPs in Type A and B neurons reflect differences in their presynaptic input, not postsynaptic factors.

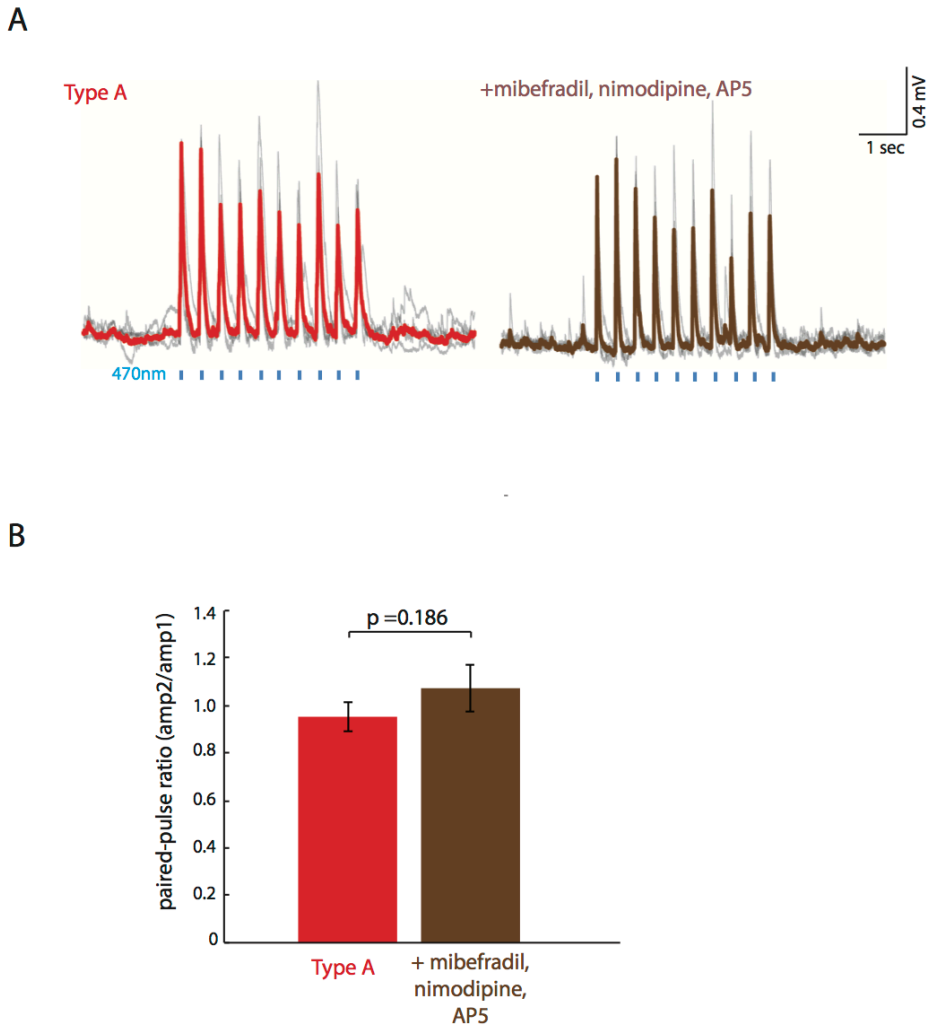

Figure 2.4. Blocking post-synaptic voltage-dependent Ca2+ channels and NMDARs does not alter EPSP dynamics in Type A neurons.

(A) Application of mibefradil (5 M) + nimodipine (5 M) + AP5 (50 M) does not alter EPSP dynamics in Type A during optogenetic stimulation of callosal inputs (n = 4). **(B)** The paired-pulse ratio is not significantly different after applying these Ca2+ channel blockers (p = 0.19, n = 4).

2.4.3 Differences in callosally-evoked spiking depend on postsynaptic Ca^{2+} currents

During paired-recordings of callosal stimulation (described above), we observed more spikes in Type A neurons than Type B neurons (Fig. 2.5A; spiking occurred in 3/11 pairs;

whereas we used 5-10 Hz trains to minimize ChR2 inactivation while studying EPSP depression, for studying spiking we used 20 Hz trains which led to greater EPSP summation and spiking). We asked whether greater Type A neuron spiking reflects differences in presynaptic inputs or postsynaptic excitability. To test this, we injected current waveforms resembling those in Fig 2.3C, but scaled up by a factor of 2 to elicit spikes. The waveforms in Fig. 2.3C reflect averages across all experiments, whereas EPSPs were larger in recordings that elicited spiking. Thus the "scaled up" waveforms were consistent with the EPSPs that elicited spiking. We also injected tonic current to maintain resting membrane potentials near -65 mV (neither the injected current nor the resulting resting potentials differed between type A and B neurons; resting potential, Type A: -65.7 ± 1.4 mV, Type B: -66.7 ± 0.3 mV, p=0.5; average current, Type A: 8.7 ± 4.1 pA, Type B: 15 ± 6.1 pA, p=0.4). Type A neurons spiked more than Type B neurons, regardless of whether we injected input waveforms derived from Type A or B neurons, suggesting that postsynaptic differences between Type A and B neurons contribute to differences in spiking (Fig. 2.5B,C).

We have previously found that Ca^{2+} and Ca^{2+}-dependent currents profoundly influence the excitability of Type A neurons (Gee et al., 2012). To test whether similar mechanisms might enhance Type A neuron spiking here, we recorded the voltage responses of Type A neurons to input waveforms derived from both Type A and B neurons before and after applying Ni^{2+} (0.5 mM) to block voltage-gated Ca^{2+} channels. The increased firing observed in Type A neurons was significantly reduced when voltage-gated calcium channels were blocked ($p<0.01$; Fig 2.5B-D), suggesting that voltage-gated Ca^{2+}channels contribute to increased spiking in Type A neurons.

We also tested whether the more prominent I_h in Type A neurons affects their responses to these input waveforms, but found minimal changes in spiking and EPSP dynamics after blocking I_h with ZD7288 (25 μM; Fig. 2.6).

2.4.4 Callosal stimulation elicits more circuit inhibition in Type A neurons

Excitatory callosal inputs recruit local feedforward inhibitory circuits. Thus we tested if Type A and B neurons receive different levels of feedforward inhibition. In the previously described experiments, in which we excited ChR2-expressing callosal projections while dual-patching Type A and B neurons, we also recorded IPSCs in voltage-clamp at +10mV. Surprisingly, Type A neurons received significantly more inhibitory current than Type B neurons (Fig. 2.7A,B). Both the peak IPSC amplitude (Type A: 1.0 ± 0.3 nA, Type B: 0.4 ± 0.2 nA; $p<0.01$) and inhibitory charge transfer (Type A: 18.9 ± 6.0 pC, Type B: 10.5 ± 5.5 pC; $p<0.05$) were significantly greater in Type A than B neurons (n=11 pairs). Fast outward currents were completely blocked by picrotoxin (10 μM; n=3; Fig. 2.8A). The latency from the beginning of each light flash to the peak of the IPSC was ~2 msec longer than the corresponding latency for EPSCs (9.7 ± 0.8 msec vs. 7.3 ± 0.5 ms; Fig 2.8D), consistent with primarily feedforward (as opposed to feedback) inhibition.

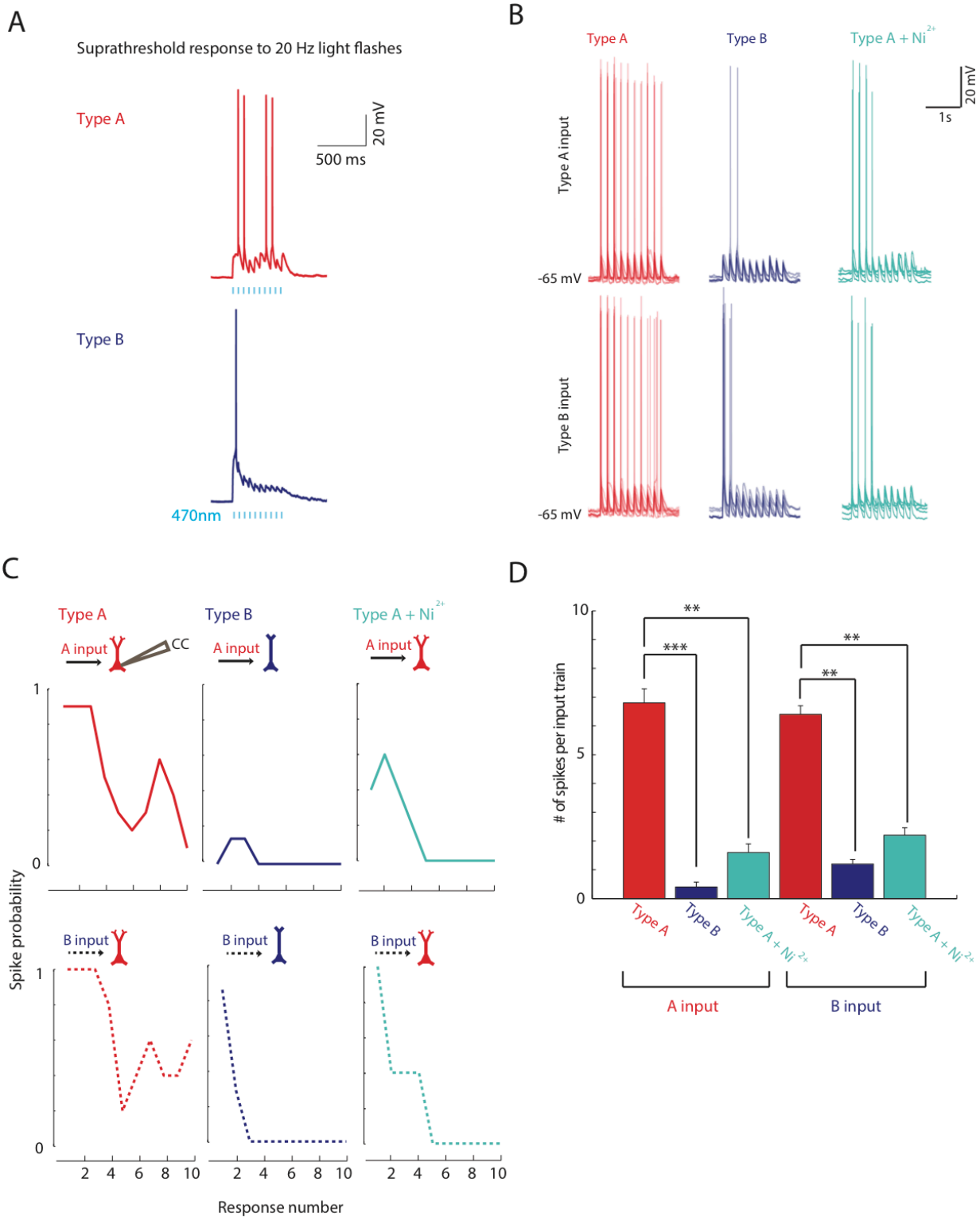
A
Suprathreshold response to 20 Hz light flashes
Type A
20 mV
500 ms
Type B
470nm
B
Type A
Type B
Type A + Ni2+
20 mV
1s
Type A input
-65 mV
Type B input
-65 mV
C
Type A
Type B
Type A + Ni2+
A input
CC
A input
A input
B input
B input
B input
Spike probability
1
0
1
0
2 4 6 8 10
2 4 6 8 10
2 4 6 8 10
Response number
D
# of spikes per input train
10
5
0
**
***
**
**
Type A
Type B
Type A + Ni2+
Type A
Type B
Type A + Ni2+
A input
B input

Figure 2.5. Postsynaptic Ca^{2+} currents contribute to increased spiking in Type A neurons. **(A)** Example of paired Type A/B responses illustrating greater spiking in Type A neurons. **(B)** Population overlay of responses of either Type A (red) or B (blue) neurons to Type A or B current waveforms. Type A neuron responses in Ni^{2+} are in teal. Steady current was injected to maintain all resting membrane potentials around -65 mV. **(C)** Spike probability for each simulated light pulse during injection of Type A or B current waveforms into postsynaptic Type A or B neurons. Type A neurons spiked more, regardless of the type of input waveform (A vs. B). Ni^{2+} dramatically reduces spiking in Type A neurons. **(D)** Number of spikes per train of ten simulated inputs. **=p<0.01, ***=p<0.001, n=5 for each condition. See also Fig. 2.6.

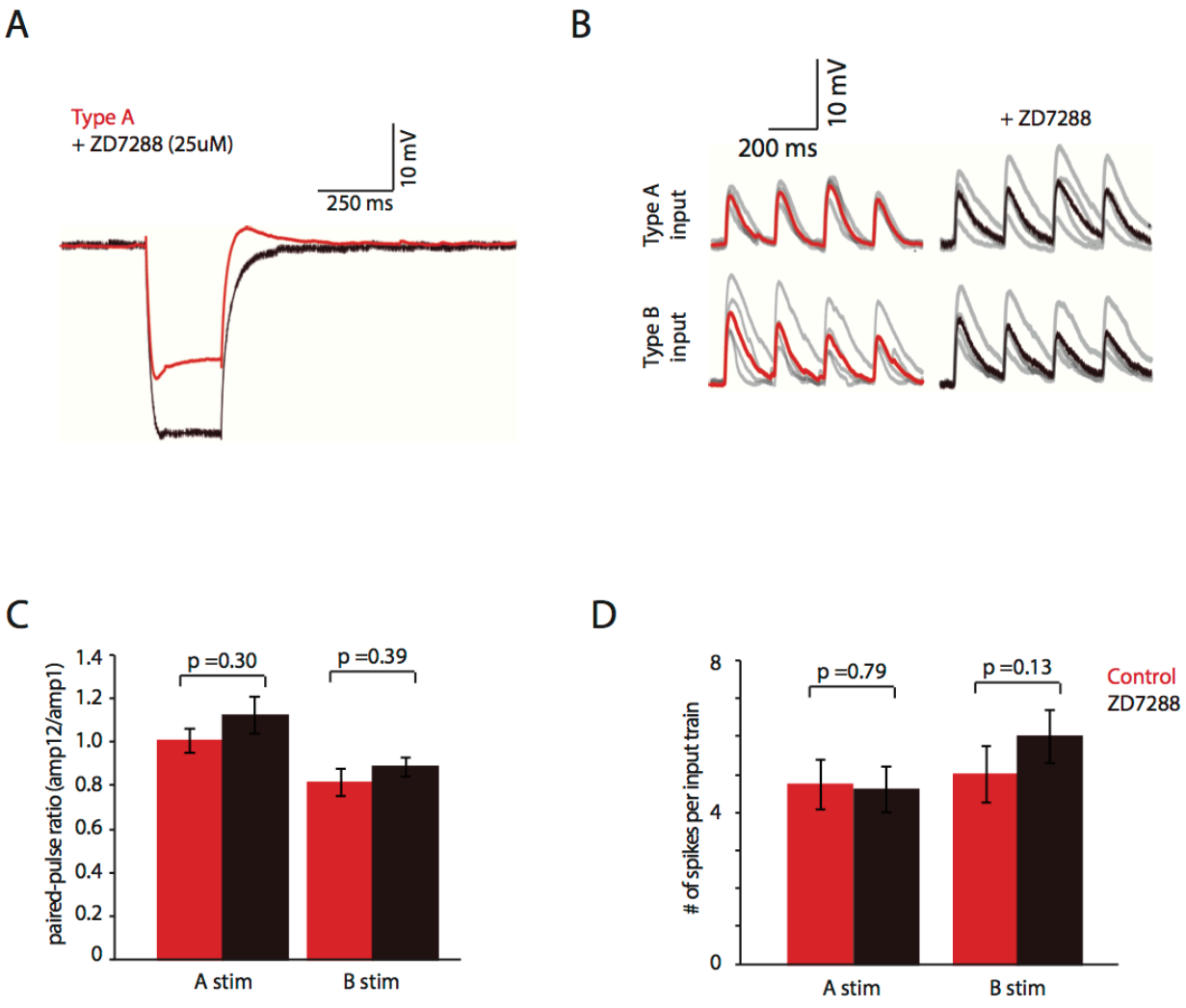

Figure 2.6. Blocking h-current has minimal effects on simulated EPSPs and spiking in Type A neurons.

(A) ZD7288 (25 M) blocks Ih in Type A neurons. **(B)** ZD7288 (brown) has minimal effects on the current clamp responses of Type A neurons to injection of Type A or B current waveforms (averaged response shown in black, individual responses shown in gray). **(C)** The paired-pulse ratio during responses of Type A neurons to simulated EPSCs in these current waveforms is not significantly altered by blocking Ih current ($p = 0.30$ and 0.39 for Type A and B waveforms, respectively; n=4 cells). **(D)** Blocking Ih with ZD7288 also fails to significantly alter the amount of spiking in Type A neurons in response to scaled up, suprathreshold current waveforms ($p = 0.79$ and 0.13 for Type A and B waveforms, respectively; n=4 cells).

2.4.5 Fast-spiking parvalbumin interneurons preferentially inhibit Type A neurons

Differences in inhibition might reflect different connectivity between inhibitory interneurons (INs) and these two pyramidal neuron subtypes. To explore this possibility, we recorded from fast-spiking parvalbumin interneurons (FSINs) in current clamp while simultaneously recording from either Type A or B neurons in voltage clamp at +10mV (Fig. 2.7C). We initially selected putative INs based on expression of mCherry driven by an AAV with the DlxI12b enhancer (Methods) (Potter et al., 2009), then confirmed FSIN identity based on electrophysiological criteria (Methods). FSINs had significantly greater probabilities of connecting onto Type A than Type B neurons (6/11 vs 1/12, $p=0.027$, Fisher's exact test). Importantly, the average distance between FSINs and Type A or B neurons was not significantly different (Fig. 2.8E).

To further investigate inhibitory output from FSINs onto different L5 pyramidal neuron subtypes, we optogenetically activated FSINs while simultaneously recording from a pair of Type A and B neurons. We injected AAV to drive Cre-dependent ChR2 expression into the

mPFC of parvalbumin (PV)::Cre mice (Sohal et al., 2009) (Fig. 2.7E), in which Cre expression is limited to PV-positive INs, which in neocortex are FSINs. Optogenetic stimulation of PV INs elicited significantly greater peak inhibitory current (Type A: 2.6 ± 0.7 nA; Type B: 1.3 ± 0.5 nA, $p<0.05$) and charge transfer (Type A: 60 ± 16 pC; Type B: 36 ± 13 pC, $p<0.01$) in Type A compared to Type B neurons. Again, we confirmed that this pattern of greater inhibition in Type A neurons was also present in pairs of retrogradely-labeled CT/CC neurons (data not shown; n=2 pairs).

Finally, to determine whether this preferential inhibition of Type A neurons was specific to FS/PV INs, we also recorded from pairs of Type A and B neurons in somatostatin (SOM)::Cre mice injected with the same AAV (Fig. 2.8F). In this case, we evoked inhibition by stimulating ChR2 in SOM INs, and found no consistent difference between peak inhibitory currents (Type A: 1.2 ± 0.3 nA; Type B: 1.0 ± 0.3 nA, $p=0.6$) or inhibitory charge transfer in Type A and B neurons (Type A: 37 ± 10 pC; Type B: 34 ± 10 pC, $p=0.8$) (Fig. 2.8F-G).

2.4.6 Inhibition sharpens Type A neuron responses to callosal input

If callosal inputs preferentially recruit feedforward inhibition in Type A neurons, this may accelerate the return to baseline following EPSPs in Type A neurons. We revisited our current clamp traces (Fig. 2.1B) and calculated the decay time constant for the falling phase of EPSPs (Fig. 2.7G). Indeed, Type A neurons had sharper responses to callosal inputs as indicated by their significantly shorter decay time constant (Fig. 2.5H, Type A: 41 ± 7 ms; Type B: 92 ± 19 ms, $p<0.05$).

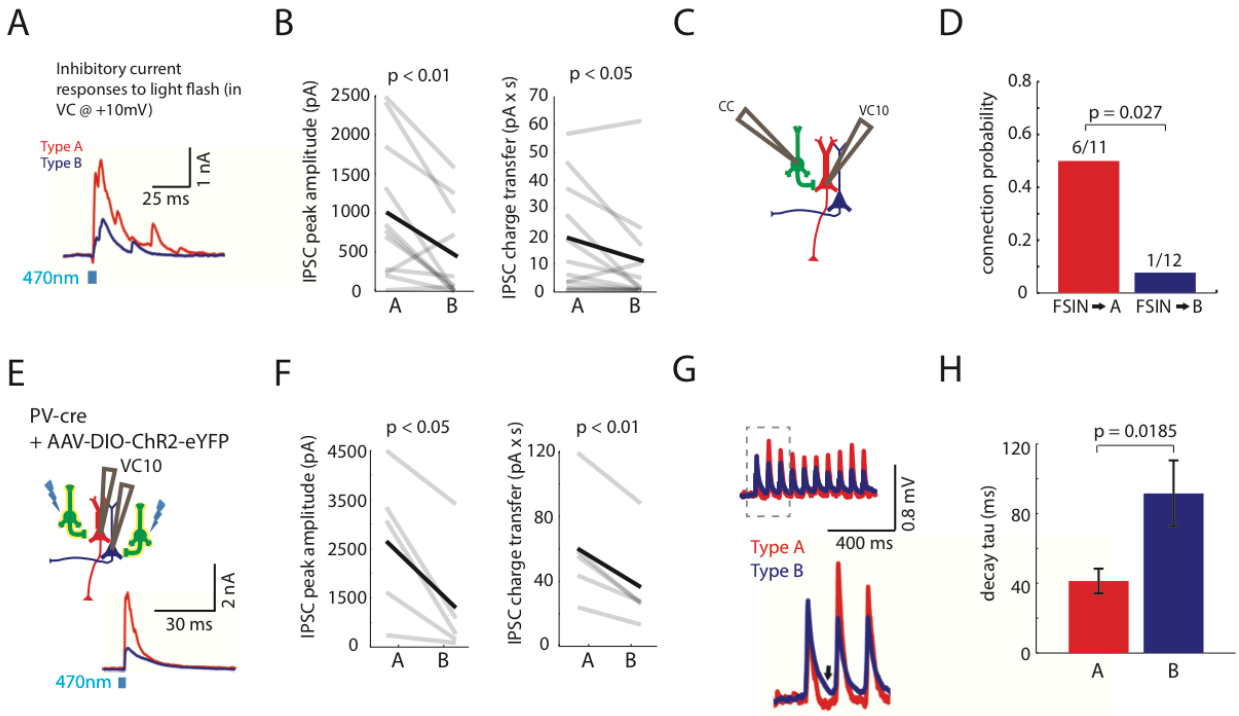

Figure 2.7. Fast-spiking parvalbumin interneurons preferentially inhibit Type A neurons. **(A)** Simultaneous recordings of IPSCs in a Type A and B neuron during optogenetic stimulation of callosal inputs. Cells were voltage clamped at +10mV. **(B)** Peak IPSC amplitude (left) and inhibitory charge transfer (right) were larger in Type A neurons compared to simultaneously recorded Type B neurons (respectively, n=11 pairs). **(C)** We made simultaneous current clamp (CC) recordings from a fast-spiking interneuron (FSIN, green) and voltage clamp recordings from either a Type A or B neuron. Current was injected to elicit FSIN spiking while recording from the pyramidal neuron in voltage clamp at +10 mV (VC10). **(D)** The connection probability from FSINs was greater onto Type A neurons than Type B neurons (n=23 pairs). **(E)** Experimental design: We recorded simultaneously from a Type A and B neuron in PV::Cre mice injected with virus to drive Cre-dependent ChR2-EYFP expression (yellow, left). During optogenetic stimulation of ChR2-expressing PV interneurons, we recorded simultaneous IPSCs in Type A and B neurons (bottom right). **(F)** PV interneuron-mediated IPSC peak amplitude (left) and inhibitory charge transfer (right) were greater in Type A than Type B neurons (n=5 pairs). **(G)** Normalized, averaged EPSPs in Type A and B neurons following optogenetic stimulation of callosal inputs. Type A neurons (red) repolarize faster (arrow

marks repolarization). **(H)** The decay time constant of callosally-evoked EPSPs is faster in Type A neurons (n=11 pairs). See also Fig. 2.8.

Feedforward inhibition might also influence the facilitation or depression of EPSPs in Type A neurons. To test this, we recorded EPSPs in Type A neurons before and after applying picrotoxin (PTX) to block $GABA_A$ currents. To avoid epileptiform discharges we applied 10 μM PTX for 10-16 min. While this eliminated most feedforward IPSCs (Fig. 2.8A), PTX had minimal effects on the facilitation or depression of Type A neuron EPSPs (Fig. 2.8B-C). However, PTX did significantly prolong the decay time constant of Type A neuron EPSPs (from 29 ± 6 msec to 45 ± 8 msec; Fig. S4A; n=4 cells; $p<0.001$ by repeated measures ANOVA), confirming that inhibition sharpens Type A neuron responses to callosal input.

2.5 Discussion

These results build on earlier studies that divided L5 pyramidal neurons in the mPFC into two subtypes. We found that callosal inputs elicit depressing EPSPs in Type B neurons while EPSPs both fail to depress and evoke more spikes in Type A neurons. Differences in the dynamics of EPSPs can be explained by differences in presynaptic inputs to Type A and B neurons whereas postsynaptic differences, including voltage-dependent Ca^{2+} currents in Type A neurons, drive the higher level of spiking in these neurons. Several observations suggest these differences derive primarily from monosynaptic callosal inputs. In particular, these differences are present even when polysynaptic activity is minimal (indicated by the absence of evoked inhibition). Regardless, callosal input elicits excitatory circuit activity that manifests differently in Type A and B neurons. Callosal inputs also elicit approximately twice as much circuit

inhibition in Type A neurons compared to Type B neurons. We found that FSINs (but not SOM INs) preferentially innervate Type A neurons, which may explain this difference.

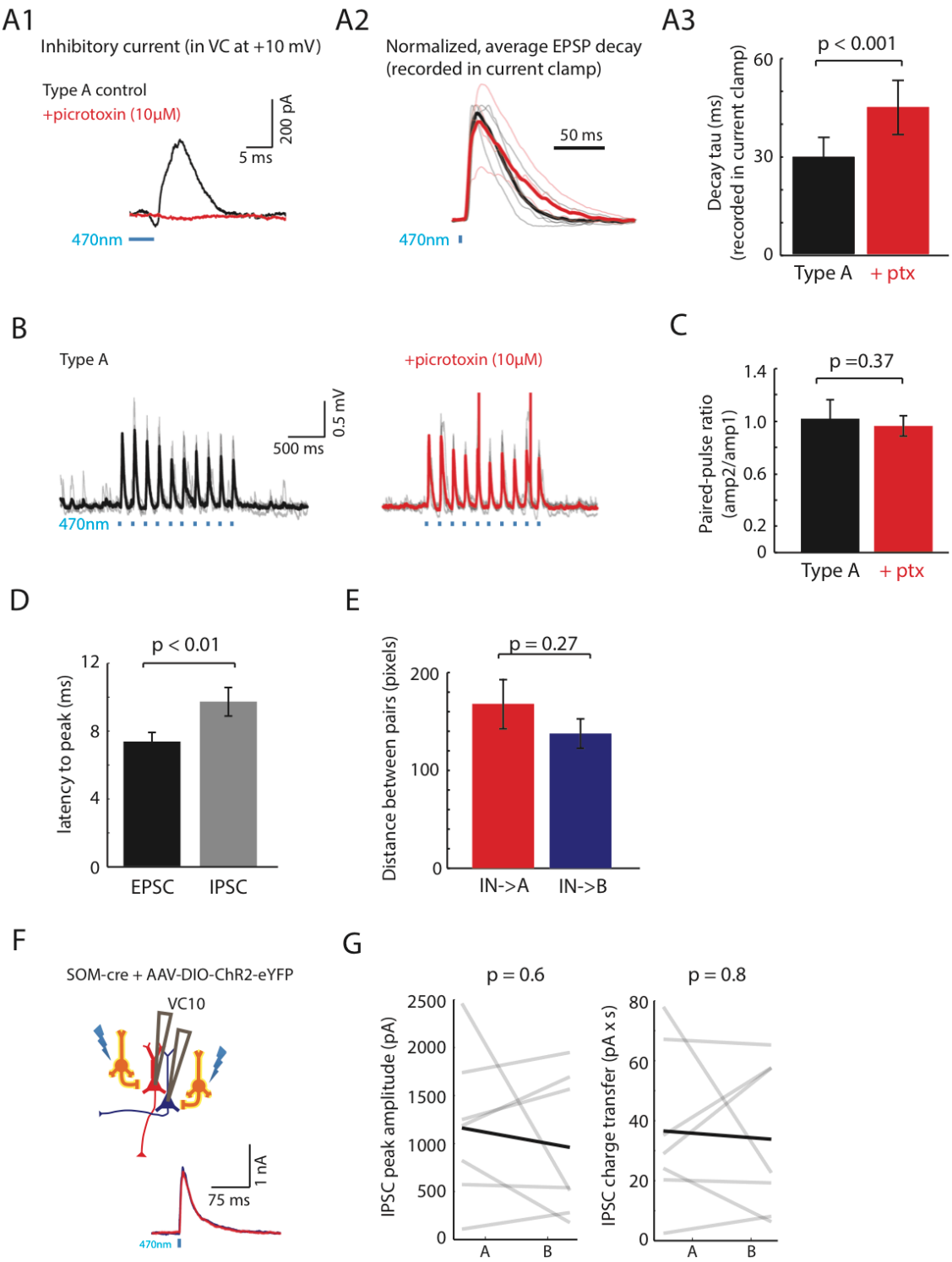

Figure 2.8. Effects of blocking GABAARs on EPSPs, and measuring inhibitory inputs to Type A and B neurons.

(A) *A1:* Picrotoxin (ptx; 10 M) blocks outward currents that follow optogenetic stimulation of callosal inputs and represent feedforward inhibition in Type A neurons. *A2:* Ptx application prolongs EPSPs in Type A neurons evoked by optogenetic stimulation of callosal inputs. Thick lines represent the averaged EPSPs before (black) and after (red) ptx application. Before averaging, each EPSP trace was normalized by the average amplitude of control EPSPs in that cell. Thin lines show individual normalized responses. *A3:* Ptx significantly prolongs the decay time constant for callosal EPSPs in Type A neurons (n=4 cells; $p<0.001$ by repeated measures ANOVA). (B) The dynamics of callosal EPSPs in Type A neurons are not significantly altered by application of ptx (black). To avoid epileptiform discharges, the light power was reduced to ~0.2 mW/mm2, i.e. 10% of the typical power, for some of these experiments. Spikes during responses in ptx have been truncated. (C) Ptx does not significantly alter the paired-pulse ratio for Type A neuron responses to optogenetic stimulation of callosal inputs ($p = 0.37$, n=4 cells). (D) Inhibitory currents peak ~2 msec after excitatory currents during optogenetic stimulation of callosal inputs ($p < 0.01$). (E) The average distance between FSINs and Type A or B neurons during experiments to measure connectivity from FSIN to these two subtypes ($p = 0.271$). (F) Experimental design: We simultaneously recorded from a pair of Type A (red) and B (blue) neurons in SOM::Cre mice injected with virus to drive Cre-dependent ChR2-EYFP expression (orange). During optogenetic stimulation of ChR2-expressing SOM interneurons, we recorded simultaneous IPSCs in Type A and B neurons in voltage clamp at +10 mV (bottom). (G) The peak amplitude of SOM interneuron-mediated IPSCs (left) and the corresponding inhibitory charge transfer (right) were similar in Type A and B neurons ($p = 0.6$ and $p = 0.8$, respectively; n=7 pairs).

2.5.1 Relationship to previous studies

Previous studies have found differences in local connections between subtypes of L5 pyramidal neurons (Brown and Hestrin, 2009; Morishima and Kawaguchi, 2006; Morishima et al., 2011; Wang et al., 2006). Our findings suggest that similar differences are also present for

long-range inputs, in this case, from the contralateral mPFC. Notably, callosal stimulation elicits EPSPs which depress in Type B but not Type A neurons, consistent with previous findings that local excitatory connections between neurons resembling either Type A or B neurons exhibit facilitation and depression, respectively (Morishima et al., 2011; Wang et al., 2006).

Our result that FSINs preferentially inhibit Type A neurons may explain an earlier observation that disynaptic inhibition occurs more frequently between pairs of thick-tufted L5 pyramidal neurons than between pairs of callosally projecting L5 pyramidal neurons (Le Be et al., 2007). However, our result contrasts with an older anatomical study in cat visual cortex, showing that corticocortical neurons receive more inhibitory synapses onto their somata and axon initial segments than do corticothalamic neurons (Farinas and DeFelipe, 1991). It will be important to determine whether this reflects species or regional differences, or differences between anatomical and physiologic measurements.

Our finding of differential FSIN output onto neighboring subtypes of L5 pyramidal neurons parallels similar findings in entorhinal cortex (Varga et al., 2010), but contrasts with another study of neocortical FSINs (Packer and Yuste, 2011). There are several differences between the latter study and this one, including the methods for measuring interneuron connectivity (glutamate uncaging vs. paired recording), ages (P12-17 vs. adult), neocortical regions (primarily somatosensory vs. prefrontal), and layers studied (primarily L2/3 vs. L5). It will be important to determine which factors explain the differences between these studies.

2.5.2 Implications for normal and pathological prefrontal microcircuit function

Increased circuit inhibition in Type A neurons, likely mediated by increased FSIN innervation, sharpens Type A neuron responses to callosal input. By contrast, the relative

absence of such inhibition results in an approximate doubling of EPSP duration in Type B neurons, which could enhance temporal summation. These differences could act in concert with differences in EPSP facilitation or depression to render Type A and B neurons maximally sensitive to distinct patterns of input. Specifically, if inputs to Type A neurons facilitate even weakly, then Type A neurons will respond more when inputs are concentrated on a single fiber, eliciting facilitation, than when inputs are distributed across many fibers, in which case no facilitation occurs. Depressing inputs elicit the opposite pattern: input concentrated on a single fiber cause depression, and as a consequence, Type B neurons should respond more strongly when inputs are distributed across many fibers. These differences may endow Type A and B neurons with distinct computational properties. Specifically, Type B neurons, which project callosally, may integrate intracortical signals from many input fibers over time to accumulate evidence as part of decision making (Curtis and Lee, 2010), or maintain persistent activity that stores items in working memory (Funahashi et al., 1989). By contrast, Type A neurons may be sensitive to strong, focal inputs that are concentrated onto a small number of input fibers and occur close together in time. This may enable Type A neurons to transmit signals about particularly salient events to downstream subcortical structures, e.g. MD thalamus, as part of corollary discharge (Wang et al., 2004). Activation of dopamine D2 receptors may further amplify Type A neuron responses to salient inputs (Gee et al., 2012).

Greater FSIN innervation of Type A neurons suggests that FSIN dysfunction, hypothesized to play a major roles in schizophrenia (Lewis et al., 2005), may cause relatively more severe disruptions in Type A neuron function. Within prefrontal cortex, Type A neurons represent a point of convergence for FSIN-mediated inhibition, L-type Ca^{2+} channels, outputs to MD thalamus, and D2 receptors, all of which have been strongly linked to schizophrenia

(Marenco et al., 2012; Ripke et al., 2011). Thus, abnormal Type A neuron excitability may represent a specific physiological substrate that contributes to prefrontal dysfunction in schizophrenia.

2.5.3 Limitations and future directions

Although we recorded simultaneous responses of Type A and B neurons to callosal inputs, we do not know whether the same callosal fibers synapsed onto both Type A and B neurons, or whether subpopulations of callosal fibers, originating from different neurons, innervate these two subtypes. Future experiments might selectively stimulate various subpopulations of callosally-projecting prefrontal neurons, while measuring the responses of Type A and B neurons to disambiguate these two possibilities.

2.5.4 Conclusions

Callosal inputs elicit circuit excitation and inhibition that manifest differently in two subtypes of L5 pyramidal neurons within the mPFC, possibly contributing to distinct computational functions. It will be important for future studies to determine whether other long-range inputs also differentially innervate these and other subtypes of prefrontal neurons.

3. A class of GABAergic neurons in the prefrontal cortex sends long-range projections to the nucleus accumbens and elicits acute avoidance behavior

3.1 Abstract

GABAergic projections from the neocortex to subcortical structures have been poorly characterized. Using Dlxi12b-Cre mice, we found anatomical evidence for GABAergic neurons that project from the mouse medial prefrontal cortex (mPFC) to multiple subcortical targets. We used a combination of patch-clamp electrophysiology, optogenetics, and pharmacology to confirm that Dlxi12b-labeled projections from the mPFC to the nucleus accumbens (NAcc) release GABA and do not co-release glutamate. Furthermore, optogenetic stimulation of these GABAergic projections from mPFC to NAcc induces avoidance behavior in a real-time place preference task, suggesting that these long-range projecting GABAergic neurons can transmit aversive signals. Finally, we found evidence for heterogeneous histochemical and/or electrophysiological properties of long-range projecting GABAergic neurons in the mPFC. Some of these neurons were labeled in PV-Cre and VIP-Cre mice. We also used a novel intersectional targeting strategy to label GABAergic neurons in the mPFC that project to NAcc, and found that these neurons have fast-spiking properties and express parvalbumin. These results define possible functions and properties for a class of long-range projecting GABAergic neurons in the neocortex.

3.2 Introduction

Knowledge about GABAergic neurons in the neocortex that send long-range projections to other structures remains sparse. Anatomical studies using retrograde tracing and immunohistochemistry have estimated that in mice, cats, and monkeys, <1-10% of all neocortical GABAergic cells give rise to long-range projections (Peters, Payne, and Josephson 1990; Higo et al. 2009; Tomioka and Rockland 2007; Tamamaki and Tomioka 2010; Tomioka et al. 2005). Neocortical long-range projecting GABAergic neurons appear to constitute a heterogeneous population based on histochemical markers (PV+, SOM+, NPY+, nNOS+, NADPH+, M2R+) and morphology (Tomioka et al., 2005; Jinno et al., 2007; Higo et al., 2009). Previous studies have not examined possible physiological or behavioral functions for neocortical long-range GABAergic projection neurons, but their connectivity onto GABAergic neurons in distant cortical regions suggests that they may synchronize oscillatory activity (Caputi et al., 2013).

Recent applications of optogenetics have advanced our understanding of GABAergic projection neurons in subcortical structures and the hippocampus. GABAergic neurons in the medial septum form reciprocal circuits with hippocampal GABAergic neurons, signaling salient sensory events and controlling hippocampal theta oscillations (Jinno et al., 2007; Hangya et al., 2009; Kaifosh et al., 2013). Further modulation of rhythmic oscillations occurs via a bi-directional GABAergic circuit comprising the hippocampus and entorhinal cortex (Melzer et al., 2012; Caputi et al., 2013). GABAergic projections from the ventral tegmental area to the nucleus accumbens (NAcc) can enhance associative learning (Brown et al., 2012); similar projections also regulate striatal output (Tritsch et al., 2012).

"Top-down" control by the prefrontal cortex (PFC) can influence emotional valence and motivated actions, often by inhibiting innate "bottom-up" processing (Miller, 2000; Shin and Liberzon, 2010; Lammel et al., 2014). Thus, if subcortically-projecting GABAergic neurons exist in the PFC, they would be well positioned to exert top-down inhibitory control on subcortical processes. Indeed, here we describe evidence for long-range projecting GABAergic neurons in the medial PFC (mPFC) and demonstrate that stimulation of their projections to NAcc elicits avoidance behavior.

3.3 Methods

All experiments were conducted in accordance with procedures established by the Administrative Panels on Laboratory Animal Care at the University of California, San Francisco.

3.3.1 Cloning of viral constructs

To produce the inhibitory intersectional retrograde tracer, we introduced MluI and BamHI compatible sticky ends to the Dlxi12b-BG sequence with PCR. The AAV-EF1a-DIO-Chr2-eYFP (from Karl Deisseroth) was then cut with MluI/BamHI and ligated to the PCR insert to exchange the EF1a promoter for Dlxi12b-BG. Virus was packaged by UNC Vector Core with serotype AAV5.

3.3.2 Slice preparation

Slice preparation and intracellular recording followed our published protocol (Sohal and Huguenard, 2005). We cut 250 μm coronal slices from 8- to 11-week-old mice of either sex. ACSF contained (in mM): 126 NaCl, 26 $NaHCO_3$, 2.5 KCl, 1.25 NaH_2PO_4, 1 $MgCl_2$, 2 CaCl, and 10 glucose. We used the following mouse lines: wild-type C57BL/6 mice (Charles River)

B6;129P2-*Pvalbtm1(cre)Arbr*/J (line 008069, Jax), *Viptm1(cre)Zjh/*J (line 010908, Jax), *Ssttm2.1(cre)Zjh/J* (line 013044, Jax) and *Tg(I12b-cre)1Jlr*.

3.3.3 Intracellular recording

We obtained somatic whole-cell patch recordings using a Multiclamp 700A (Molecular Devices) and differential contrast video microscopy on an upright microscope (BX51WI; Olympus). Patch electrodes (tip resistance = 2–6 MOhms) were filled with the following (in mM): 130 K-gluconate, 10 KCl, 10 HEPES, 10 EGTA, 2 MgCl, 2 MgATP, and 0.3 NaGTP (pH adjusted to 7.3 with KOH). All recordings were at 32.5±1°C. Series resistance was usually 10–20 MΩ, and experiments were discontinued above 30 MΩ.

3.3.4 Injection of opsin-containing virus or retrograde tracers

For Cre-dependent expression of ChR2 or EFYP, we injected 600nl of a previously described adeno- associated virus (AAV) vector that drives Cre-dependent expression of a ChR2-EFYP fusion protein via previously described procedures (Sohal et al., 2009). Before stimulating ChR2-containing terminals in the NAc, we first verified the absence of fluorescent soma in the field of view. Coordinates for injection into mPFC were (in millimeters relative to bregma): 1.7 anterior-posterior (AP), 0.3 mediolateral (ML), and -2.50-2.7 dorsoventral (DV). CTb-488 (Molecular Probes, Life Technologies) was injected as above with the following NAc coordinates: 0.90 AP, 0.65 ML, -4.75 DV. We waited 2-3 days after injecting CTb before preparing brains slices.

3.3.5 ChR2 stimulation

We stimulated ChR2 in neurons using ~5mW flashes of light generated by a Lambda DG-4 high-speed optical switch with a 300W Xenon lamp (Sutter Instruments), and an excitation filter set centered around 470 nm, delivered through a 40x objective (Olympus).

3.3.6 Behavioral tests

For social and novel object exploration, a juvenile mouse (<4 wks) or 50mL Falcon tube cap, respectively, was placed with the experimental mouse in its home cage for 5 minutes. Exploration time was scored by the duration of nose-juvenile or nose-object contacts, and reviewer was blinded to the virus identity and laser condition.

Real time place preference (RTPP) occurred during three 20 min sessions over 3 days. On day 1, mice were habituated to the 2-chamber apparatus. On day 2, mice were placed into one chamber and its movement was tracked by Anymaze (Stoelting Co., IL). On day 3 mice were placed in the chamber opposite to one that was randomly designated to trigger 20Hz laser pulses (470nm, 15-20mW, 5ms) upon entry. The sides of the stimulated chambers were counterbalanced across all mice, and the experimenter was blind to the injected virus (control vs. ChR2).

3.3.7 Drug application

Drugs were dissolved in water (DL-AP5, CGP 35348) or dimethylsulfoxide (CNQX, gabazine) before being diluted in ACSF.

3.3.8 Immunohistochemistry

After patch clamp, slices were fixed in 4% PFA for at least one day. Primary antibody used was mouse monoclonal anti-parvalbumin (Millipore). Alexa Fluor 488 goat anti-mouse (Life

Technology) was first applied then washed for at least two days before addition of CF405 monoclonal mouse anti-biotin (Biotium).

3.3.9 Statistical analysis

We used Student's t-tests to compare across conditions or N-way ANOVA unless noted otherwise. Error bars indicate ± 1 SEM.

3.4 Results

3.4.1 Verification of GABAergic-specific Dlxi12b-Cre transgenic mouse line

To visualize candidate long-range GABAergic projections originating from the neocortex, we first injected a Dlxi12b-cre mouse with AAV-DIO-ChR2-EYFP in the mPFC (Figure 3.1A). *Dlx1* and *Dlx2* are expressed by developing GABAergic neurons as they mature and migrate out of the ganglionic eminences in embryonic mice, and are expressed predominately, if not exclusively, by GABAergic neurons (Anderson et al., 1997; Marin and Rubenstein, 2003). Indeed, many studies have used Dlxi12b-Cre mice to selectively label GABAergic neurons (Potter et al., 2009; Flandin et al., 2011; Han et al., 2012; Arguello et al., 2013). More recently, our laboratory has used the Dlxi12b enhancer to selectively express mCherry or ChR2 in cortical GABAergic neurons (Lee et al., 2014).

To confirm that, as in previous studies, Dlxi12b-labeled neurons are GABAergic and not glutamatergic, we recorded optogenetically evoked synaptic responses (470nm; 5 msec; ~5 mW/mm^2) from mPFC pyramidal neurons of Dlxi12b-Cre mice injected with AAV-DIO-ChR2-EYFP. Thus, we used patched pyramidal neurons as "biosensors" to detect neurotransmitters released by nearby Dlxi12b-labeled neurons (Figure 3.1C). During voltage-clamp recordings at

both -70 mV and +10 mV, application of gabazine (10 μM) + CGP35348 (5 μM) essentially abolished all optogenetically evoked synaptic currents (Figure 3.1C; the small residual outward current in one recording at -70 mV presumably represents incompletely blocked $GABA_BR$-mediated current). This confirms that no glutamatergic neurons were labeled in the mPFC of Dlxi12b-Cre mice.

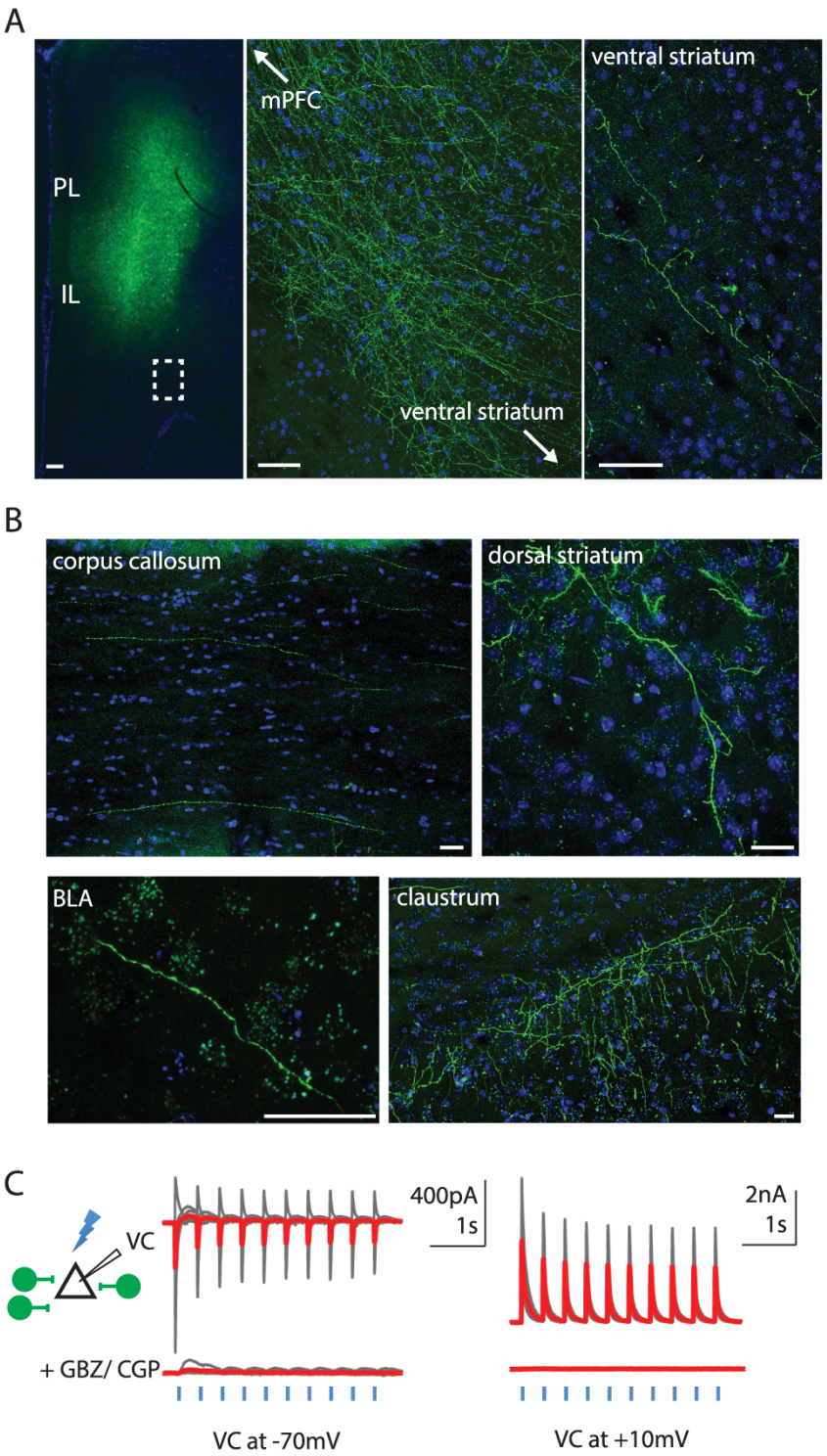

Figure 3.1. GABAergic neurons in the prefrontal cortex project to subcortical targets.

(A) *Left*, AAV-DIO-ChR2 was injected into the cingulate (Cg), prelimbic (PL), and infralimbic (IL) of mPFC in Dlxi12b-Cre mice. *Middle*, magnified view of the region of the left panel indicated by the dashed box. No labeled cell bodies were present in areas

adjacent to the injection site, suggesting limited viral spread. *Right*, Dlxi12b-labeled fibers were found in ventral striatum (scale bars: 50 μm). **(B)** Dlxi12b-labeled fibers from prefrontal cortex are found in corpus callosum, dorsal striatum, claustrum, and basolateral amygdala (BLA) (scale bars: 30 μm). **(C)** Dlxi12b-labeled cells are exclusively GABAergic. *Left*, experimental design: we made voltage-clamp recordings from pyramidal cells (triangle) while optogenetically stimulating ChR2-expressing neurons (green) in Dlxi12b-Cre mice injected with AAV-DIO-ChR2-eFYP. *Right*, optogenetically evoked synaptic currents were abolished by gabazine (GBZ) + CGP35348 (CGP) (n=6 pyramidal neurons).

3.4.2 Dlxi12b-labeled fibers project from mPFC to distant subcortical brain regions

Our injection site spanned the mPFC, including the anterior cingulate, prelimbic, and infralimbic regions (Figure 3.1A, left). Surprisingly, we observed labeled fibers several millimeters from the injection site within corpus callosum and subcortical structures including dorsal striatum, ventral striatum (nucleus accumbens; NAcc), claustrum, and basolateral amygdala (Figure 3.1A, B). Importantly, no labeled cell bodies were found in these distant sites, including fields of view that were directly adjacent to the injection site (Figure 3.1A, middle).

3.4.3 Dlxi12b-labeled projections to the nucleus accumbens release GABA but not glutamate

Out of the candidate regions identified as possible targets for long-range GABAergic projections by Figure 3.1, we decided to focus on projections to the NAcc, because its distance from the mPFC minimizes the probability of virus leakage. To determine whether long-range Dlxi12b-labeled projections from mPFC to NAcc release GABA and/or glutamate, Dlxi12b-Cre mice were injected with AAV-DIO-ChR2-EYFP in the mPFC. After waiting at least 4 weeks for expression, we made whole cell recordings from neurons within the NAcc shell in acute brain slices. We recorded in voltage-clamp at +10mV while stimulating ChR2-containing terminals

with blue light (470nm, 5 Hz, 5 msec, ~5 mW; Figure 3.2A). No ChR2-labeled cell bodies were observed within NAcc during any of our recordings (Figure 3.2B). Light-evoked IPSCs were detected in 13/29 patched neurons within NAcc (average peak IPSC amplitude: 391 ± 95 pA; n = 13). To confirm that these projections release GABA, in a subset of recordings, we bath applied glutamate receptor antagonists (10 μM CNQX + 50 μM AP5) followed by gabazine (GBZ, 10 μM). Whereas CNQX+AP5 exerted inconsistent effects on light-evoked IPSCs, the addition of GBZ essentially abolished them, demonstrating that these outward currents were GABAergic (control: 521 ± 160 pA; CNQX+AP5: 424 ± 135 pA; GBZ+CNQX+AP5: 9.4 ± 1.8 pA; $t(6) = 1.84$, $p = 0.12$ for control vs CNQX+AP5; $t(6) = 3.19$, $p=0.02$ for control vs GBZ+CNQX+AP5; $t(6) = 3.09$, $p=0.02$ for CNQX+AP5 vs GBZ+CNQX+AP5; n=7 cells; interaction by drug condition: $F(2,6) = 9.52$, $p = 0.003$; Figure 3.2C,D). Furthermore, in separate experiments, GBZ alone abolished light-evoked currents recorded at either -70 mV or +10 mV, demonstrating the absence of glutamate co-release (currents at -70 mV: control: 12 ± 7 pA, GBZ: 2 ± 1 pA. $F(3,1) = 8.21$, $p = 0.001$; currents at +10 mV: control: 203 ± 53 pA, gabazine: 12 ± 4pA. $F(3,1) = 4.77$, $p = 0.01$; n = 4 cells; Figure 3.2E,F).

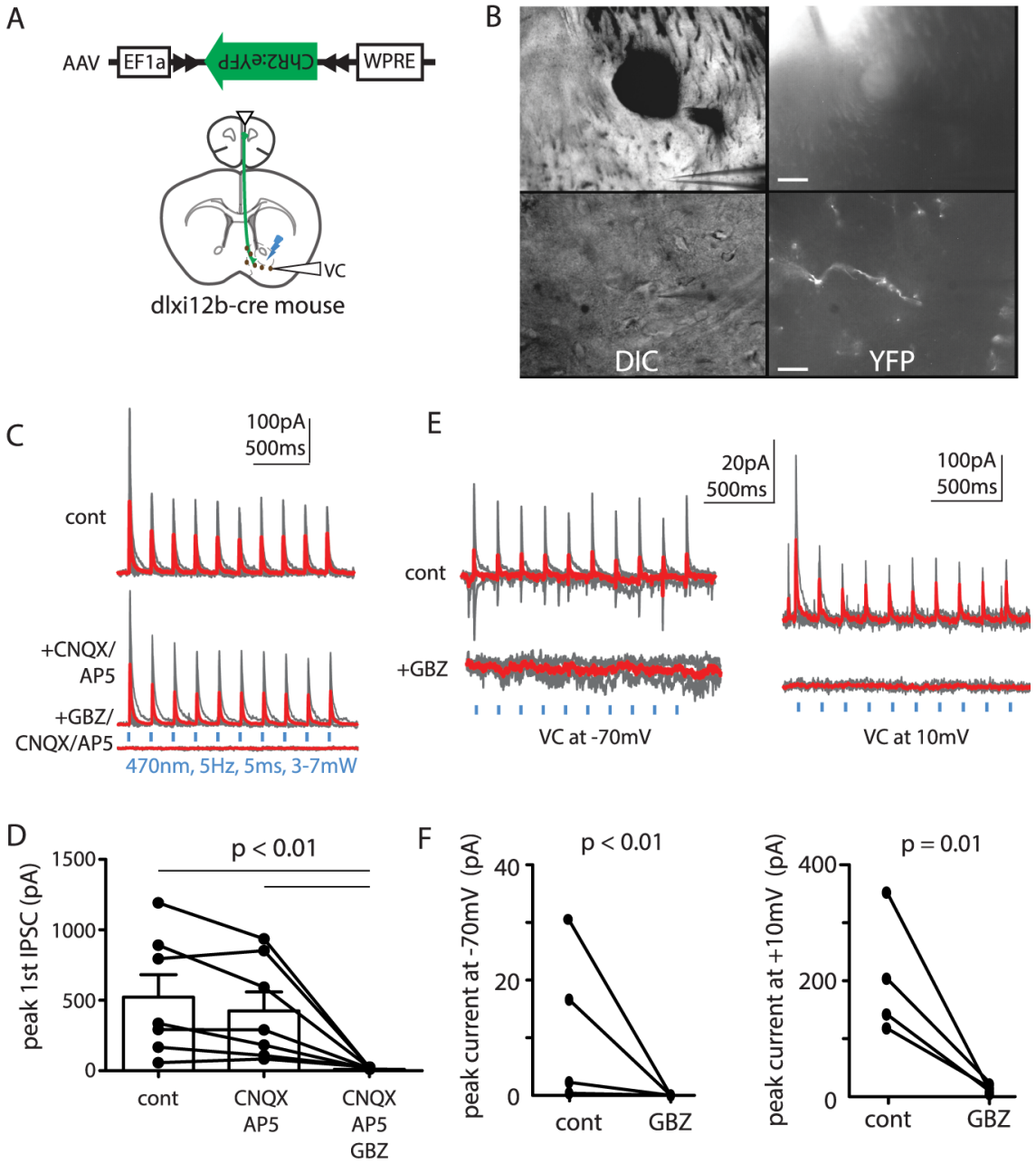

Figure 3.2. Dlxi12b-labeled PFC neurons projecting to ventral striatum exclusively release GABA.

(A) Experimental design: Dlxi12b-cre mice were injected with AAV-DIO-ChR2-eYFP into the mPFC. Recordings were made from NAcc neurons during optogenetic stimulation. **(B)** Images of ChR2-expressing GABAergic fibers projecting from mPFC within NAcc at low- and high-power (upper and lower rows, scale bars: 60 and 15 µm, respectively). **(C, D)** Long-range Dlxi12b-labeled projections from mPFC release GABA. Light-evoked outward currents were inconsistently affected by CNQX/AP5 but

completely blocked by adding gabazine (n=7 cells). **(E, F)** Dlxi12b-labeled fibers do not release glutamate as GBZ alone completely blocked currents recorded at -70 and +10 mV (n=4 cells).

3.4.4 Stimulating GABAergic projections from mPFC to NAcc elicits avoidance behavior

We hypothesized that stimulating long-range GABAergic inputs to NAcc would modulate motivational valence. To test this, we delivered optogenetic stimulation (470nm, 20 Hz, 5 ms, 15-20 mW/mm^2) into the NAcc of Dlxi12b-Cre mice that had been injected at least 4 weeks earlier with AAV to drive Cre-dependent ChR2 expression in the mPFC (Figure 3.3A). We measured the effects of this stimulation on behavior within a two-chamber "real-time" place preference task (Jennings et al., 2013) (RTPP; Figure 3.3B). In RTPP, the two chambers are contextually identical and the stimulation occurs in real-time, i.e. the light turns on whenever a mouse enters the designated stimulation chamber. Thus, in some ways, RTPP resembles self-stimulation more than conditioned place preference, and RTPP can be used to assay acute behavioral effects of stimulation. Importantly, mice do not exhibit an inherent place-bias in the two-chamber RTPP (Figure 3.3F; time spent in placed side/total time: 0.50 ± 0.03; $t(18) = 0.009$, $p = 0.99$; n = 19 mice).

We habituated mice to the RTPP chambers on Day 1, measured the time spent in each chamber in the absence of stimulation on Day 2 (baseline condition), and finally, measured the time spent in each chamber in the presence of stimulation on Day 3 (test condition). Compared to the baseline condition (Day 2), mice spend significantly less time in the stimulated side on Day 3 (test condition) (Figure 3.3C; fraction time spent in stimulated side at baseline: 0.51 ± 0.04, in presence of stimulation: 0.29 ± 0.04; $t(9) = 4.246$, $p = 0.002$, n = 10 mice). ChR2-expressing mice also spend less time on the stimulated side compared to control (ChR2-negative) mice which received light stimulation but had been injected with either DIO-eYFP or Dlxi12b-

mCherry viruses (control-mice: 0.51 ± 0.07, ChR2-expressing mice: 0.29 ± 0.04; $t(14) = 2.94$, $p = 0.01$; n=6 and 10, respectively; Figure 3.3D). We also computed the "difference score," which measures the difference between time spent on the stimulated side on Day 2 vs. Day 3. Again, ChR2-expressing mice that receive optogenetic stimulation of GABAergic projections from mPFC to NAcc spent significantly less time in the stimulated chamber on Day 3 compared to the baseline condition on Day 2 ($t(9) = 4.22$, $p = 0.002$). By contrast, there is no significant difference between time spent on the stimulated side on Days 2 and 3 in control mice that lack ChR2 (for control mice compared to baseline: $t(5) = 0.857$, $p = 0.43$; for a difference in the difference score between ChR2-expressing and control mice: $t(14) = 3.208$, $p = 0.0063$; Figure 3.3E). This acute avoidance behavior elicited by optogenetic stimulation does not appear to reflect changes in locomotion or anxiety, as testing using an open field did not reveal significant effects of stimulation on either the total distance traveled or time spent in the center of the open field (data not shown). NAcc terminal stimulation also had no effect on the time mice spend exploring a social target or novel object (data not shown) – the former is particularly notable, since social exploration is sensitive to optogenetic stimulation within the mPFC (Yizhar et al., 2011). Together these data demonstrate that long-range GABAergic projections from mPFC to NAcc modulate motivational valence and elicit acute avoidance behavior.

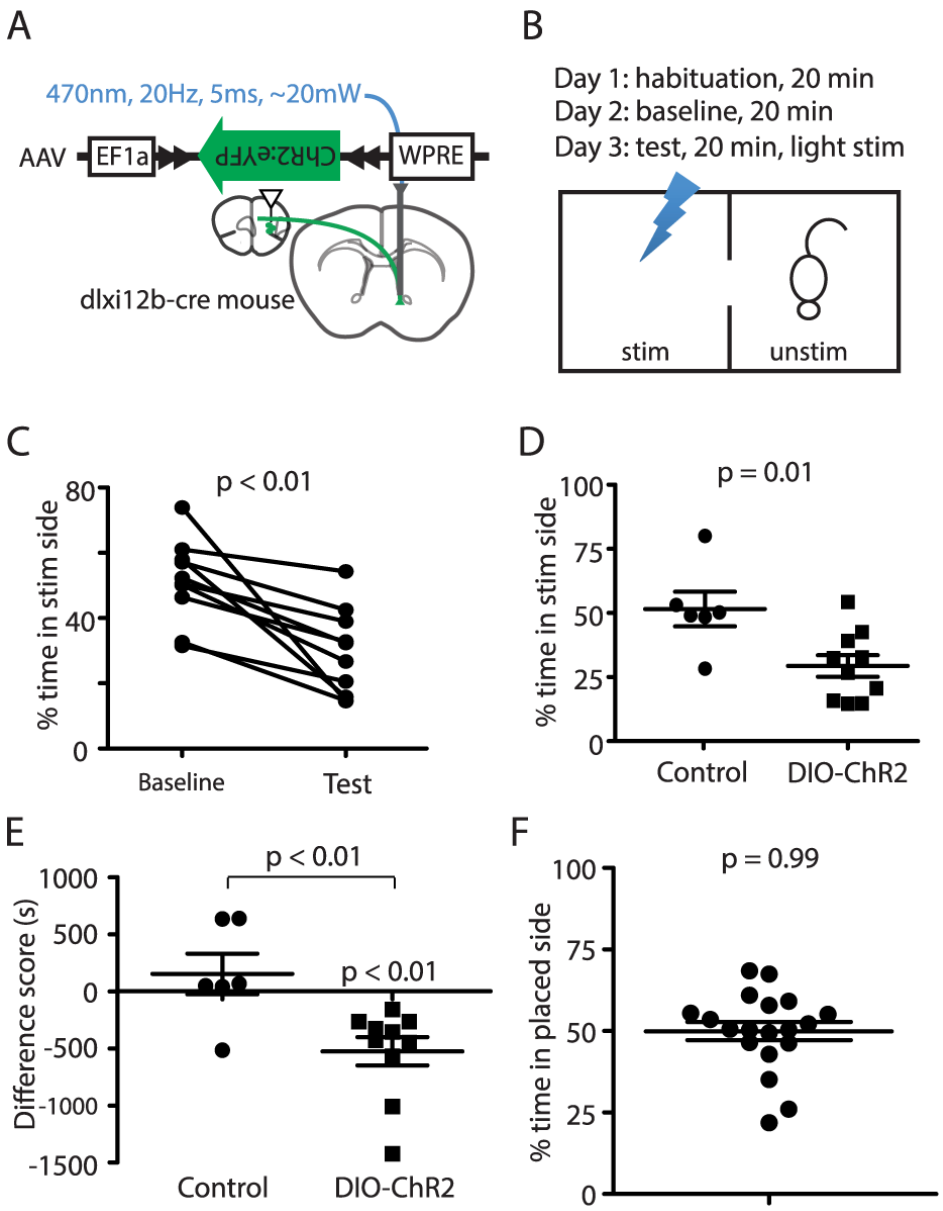

Figure 3.3. Stimulation of PFC GABAergic projections to NAcc elicits avoidance.

(A) Experimental design: AAV-DIO-ChR2-eYFP was injected into mPFC of Dlxi12b-cre mice, and optical fibers were implanted in the NAcc. **(B)** Real-time place preference paradigm. Mice were placed into a 2-chamber box for 3 days. On the test day one chamber triggered immediate light stimulation. **(C)** Mice spend less time in the stimulated side during activation of Dlxi12b-labeled mPFC-to-NAcc projections on the test day compared to baseline ($p<0.01$, n=10 mice). **(D, E)** Compared to control mice, Dlxi12b-cre mice injected with DIO-ChR2 spend less time in the stimulated side ($p<0.01$). **(F)** Mice are not biased towards the placed-side in the 2-chamber RTPP.

3.4.5 Prefrontal long-range projecting GABAergic neurons are heterogenous

We next sought to determine whether at least some long-range projecting GABAergic neurons belong to well-characterized classes of cortical GABAergic neurons. First, we crossed PV-Cre, SOM-Cre, and VIP-Cre mice to a TdTomato reporter line (Ai14) and injected CTB-488 retrograde tracer (Molecular Probes) into the NAcc (Figure 3.4A,B). Co-labeling was found in 6/144 and 5/100 TdTomato+ cells within the mPFC of PV-Cre × Ai14 and VIP-Cre × Ai14 mice, respectively (Figure 3.4A, B); 0/156 co-labeled cells were found SOM-Cre × Ai14 mice. Although the PV-cre and VIP-Cre lines both have greater than ~90% specificity for labeling their respective classes of GABAergic neurons (Sohal et al., 2009; Taniguchi et al., 2011), it is possible that these labeled cells may not actually represent PV or VIP neurons ("false positives"). Conversely, these lines may not label all GABAergic neurons belonging to a particular histochemical class ("false negatives"). To at least partially address these concerns, we devised a viral strategy that combines intersectional genetics with retrograde tracing to label long-range projecting GABAergic neurons (Figure 3.4C). We first replaced the EF1a promoter of an AAV-EF1a-DIO-ChR2-eYFP construct (Addgene) with the GABAergic neuron-specific Dlxi12b enhancer driving a minimal beta-globin promoter. This AAV-i12b-DIO-ChR2-eYFP virus was injected into the mPFC while AAV-mCherry-IRES-WGA-Cre, which drives expression of a transynaptically transported Cre-recombinase fusion protein, was injected into the NAcc of C57BL7 mice (Xu and Sudhof, 2013). Because the Dlxi12b enhancer limits the expression of ChR2-eYFP to GABAergic neurons, only GABAergic neurons that are synaptically connected to the NAcc should be labeled by WGA, despite widespread Cre-recombination of loxP/lox2272.

The five cells labeled with this intersectional retrograde tracing strategy all exhibited fast-spiking properties, as defined by narrow spikes (mean half width: 0.42 ms; range: 0.28-0.71ms) and minimal spike frequency adaptation (mean ratio of 10^{th}:1^{st} ISI: 1.05; range: 0.85-1.19) (Figure 3.4E,F). After fixing one of these brain slices, we found that 5/7 neurons labeled by this intersectional retrograde tracing strategy, including two biocytin-filled fast-spiking neurons that we had recorded from, were PV+ (Figure 3.4F).

Of course, it is theoretically possible for WGA-Cre to traverse multiple synapses, labeling neurons that are disynaptically coupled to the injection site, but do not project directly to it. However, WGA-Cre crosses each synapse with relatively low efficiency, thus the fraction of labeling should be exponentially lower for polysynaptically connected neurons than for directly projecting ones. This fact, together with the observation that all five cells we patched had fast-spiking phenotypes, suggests that this phenotype is found among GABAergic neurons projecting directly to NAcc. Furthermore, the majority of cells labeled by our intersection approach resided in layer 2/3 of mPFC (Figure 3.4A,D). By contrast, if significant polysynaptic spread had occurred, we would have expected to see additional labeled cells in L5.

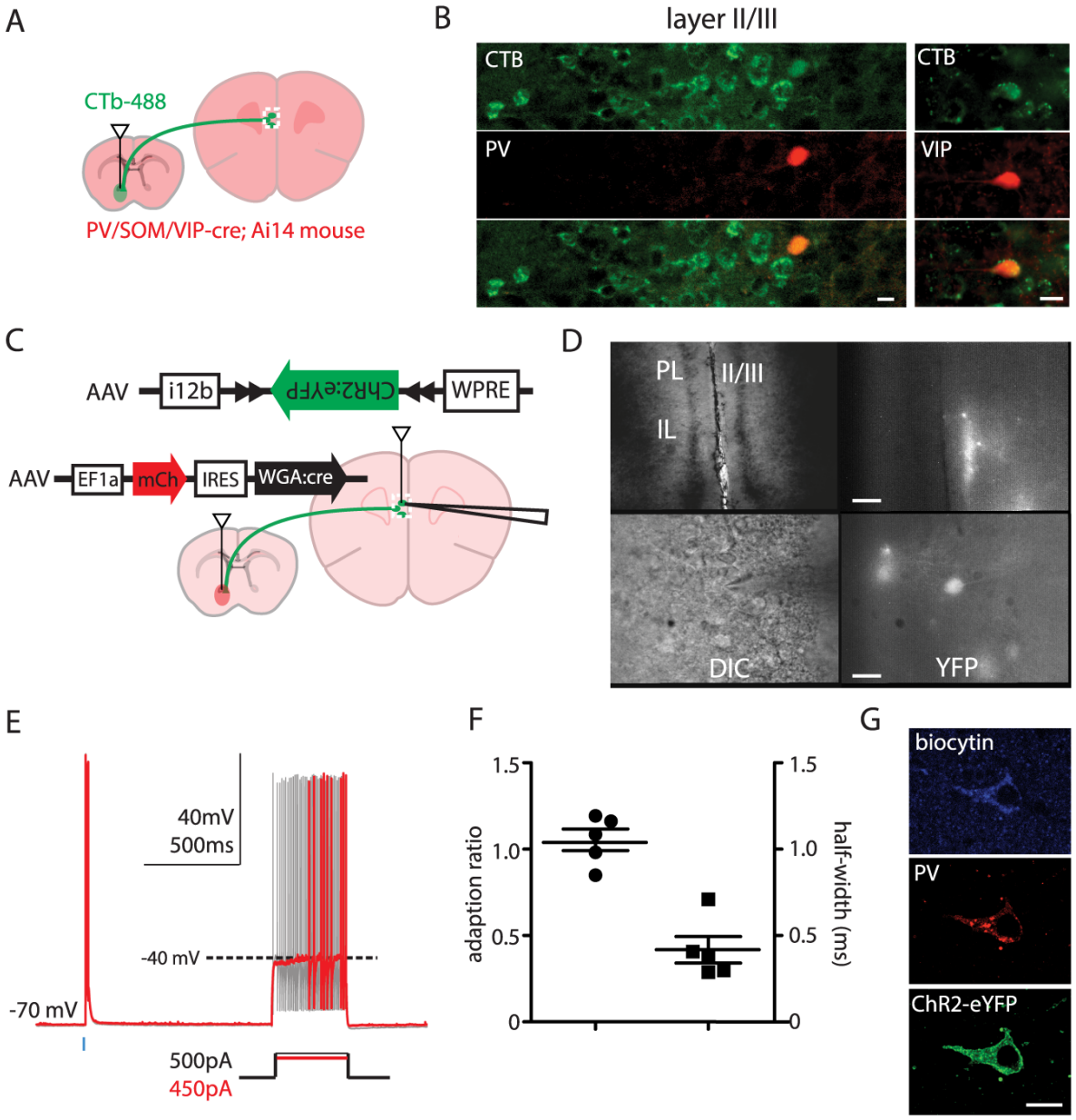

Figure 3.4. Long-range GABAergic projection neurons in PFC to NAcc are heterogeneous.

(A) Experimental design: Retrograde tracer, CTb-488, was injected into the NAcc of PV-Cre, SOM-cre, or VIP-cre mice crossed with Ai14 mice. **(B)** PV-Cre and VIP-Cre labeled neurons in mPFC (red) co-label with the retrograde tracer (green) (scale bars:15 µm). **(C)** Experimental design of a transynaptic-intersectional GABAergic neuron marker: AAV-mCh-IRES-WGA::Cre and AAV-i12b-DIO-ChR2-eYFP virus were injected into NAcc and mPFC, respectively. **(D)** Images of GABAergic neurons labeled by transynaptic-intersectional GABAergic marker in layers 2/3 at low- and high-power (upper and lower rows, scale bars: 60 and 15 µm, respectively). **(E)** Cells labeled by the transynaptic

intersectional tracer were fast-spiking. **(F)** The adaption ratios and action potential half-widths for cells labeled in E. **(G)** Transynaptically-labeled cells stain for parvalbumin (PV) (scale bar: 10 μm).

3.5 Discussion

We combined viral tracing methods, patch clamp electrophysiology, and behavior with optogenetics to establish the existence, properties, and possible functions of long-range projecting GABAergic neurons in the neocortex.

3.5.1 Classification of cortical long-range GABAergic neuron

Our initial attempts to identify known classes of cortical GABAergic neurons that contribute to long-range projections focused on PV, SST, and VIP-expressing neurons. Although these comprise ~80% of cortical GABAergic neurons, other subtypes could also contribute to long-range projections (Rudy et al., 2011). In particular, some anatomical evidence suggest that a small population of nNos+/NPY+ neurons project callosally and subcortically (Tomioka et al., 2005; Tomioka and Rockland, 2007; Higo et al., 2009; Taniguchi et al., 2011). Similar to distinct classes of neocortical pyramidal neurons, additional subtypes of long-range projecting GABAergic neurons may target distinct subcortical structures (Shepherd, 2013).

3.5.2 Roles for prefrontal long-range GABAergic neurons on modulating motivated behavior

We focused our study on long-range inhibition of the NAcc, because of its well-appreciated role in reward-seeking and motivated behavior. We find that long-range prefrontal inhibition of the NAc results in acute avoidance behavior in a RTPP paradigm. Interestingly, this aversion occurs in the absence of prior contextual associations, suggesting that these long-range inhibitory projections may act to rapidly transmit aversive signals in parallel to, or in lieu of, conditioned

associations. Of course, it is theoretically possible that stimulating projections within NAcc could elicit backpropagating action potentials that release GABA in other locations, contributing to the aversion we observed in the RTPP task. We consider such effects to be extremely unlikely in light of the relatively long distance between mPFC and NAcc, and the absence of stimulation-induced effects on other behavioral assays that measure the function of the mPFC, dorsal striatum, and amygdala. Regardless of whether stimulation in the NAcc leads to GABA release elsewhere, our results clearly demonstrate that long-range projecting GABAergic neurons, despite being relatively small in number, can powerfully shape behavior.

Notably, we failed to observe effects of tonically stimulating long-range GABAergic projections to NAcc on social exploration. This may reflect 1) inadequate recruitment of mPFC-NAcc GABAergic inputs due to unilateral stimulation, 2) a discrepancy between the effects of tonic vs phasic patterns of input (i.e., during RTPP, stimulation may be effectively phasic, because the mouse is free to move away from the stimulated chamber at any time), or 3) the absence of a role for PFC-NAcc GABAergic projections in social exploration. Future experiments could utilize "real-time" stimulation of these projections during epochs of various behaviors, e.g. social interaction, to clarify potential ways in which these projections could modulate additional behaviors.

Together, we find evidence for long-range GABAergic projections from the mPFC to subcortical targets, including the nucleus accumbens. This mPFC-NAcc projection releases GABA but not glutamate, and can elicit acute avoidance behavior. Our results suggest that these long-range projecting GABAergic neurons may comprise heterogeneous subpopulations: some are labeled in VIP-Cre mice, while others are fast-spiking and express PV. Future studies may uncover additional subtypes of long-range projecting GABAergic neurons in the neocortex.

4. Roles for prefrontal VIP neurons in local and distributed anxiety networks

4.1 Abstract and introduction

In rodents, the medial prefrontal cortex (mPFC) interacts with the ventral hippocampus (vHPC) and basolateral amygdala (BLA) to regulate anxiety-related avoidance in the elevated plus maze (EPM) (Adhikari et al., 2010; Adhikari et al., 2011; Stujenske et al., 2014; Ciocchi et al., 2015; Padilla-Coreano et al., 2016; Felix-Ortiz et al., 2016). Vasoactive intestinal polypeptide (VIP)-expressing interneurons mediate disinhibition (Lee et al., 2013; Pfeffer et al., 2013; Pi et al., 2013), and mPFC VIP interneurons are recruited by rewards and punishments [9]. However, specific ways in which prefrontal VIP interneurons modulate activity in neuronal circuits to regulate behavior remain largely unknown. To elucidate these relationships, we used a combination of calcium imaging, optogenetics, in vitro patch-clamp electrophysiology, and in vivo electrophysiology in freely moving mice as they explored the EPM. We show that VIP interneurons in the mPFC are specifically activated within anxiogenic regions of the elevated plus maze (EPM), shape future decisions to explore these anxiogenic regions, regulate electrophysiological markers of anxiety-related interactions between the mPFC and vHPC, and control the gain of anxiety-related changes in prefrontal microcircuit activity. In particular, VIP interneurons gate both mPFC spiking in response to theta-frequency vHPC input and theta-frequency vHPC-mPFC synchronization, which normally serves to transmit anxiety-related information that is necessary for the avoidance of anxiogenic regions of the EPM (Adhikari et al., 2010; Adhikari et al., 2011; Padilla-Coreano et al., 2016). These results show that even though VIP interneurons represent a small fraction of prefrontal neurons, they can reshape activity at both the microcircuit and distributed network levels in ways that explain their ability to regulate anxiety-related avoidance.

4.2 Methods

All experiments were conducted in accordance with procedures established by the Administrative Panels on Laboratory Animal Care at the University of California, San Francisco.

4.2.1 Virus injection and fiber implantation for photometry and optogenetic experiments

After isofluorane anesthesia, the scalp and periosteum were removed from the dorsal surface of the skull and scored with a scalpel to improve implant adhesion. For animals used in photometry experiments, 4 x 0.150ul of AAV2/1-Syn-FLEX-GCaMP6s (UPenn Virus Core) was injected unilaterally at 4 depths (DV: -2.0, -2.25, -2.5, -2.75) at the following AP/ML (millimeters relative to bregma) coordinates for mPFC: 1.7 anterior-posterior (AP), 0.3 mediolateral (ML). We waited 2-3 weeks before beginning behavioral experiments. For behavioral experiments using cre-dependent optogenetic opsins (Sohal et al., 2009), 0.750 µl of AAV5-EF1a-DIO-ChR2-eYFP (UNC Virus Core) or AAV5-EF1a-DIO-eArch3.0-eYFP (UNC Virus Core) was injected bilaterally into the medial PFC (mPFC). Coordinates for injection into mPFC were 1.7 (AP), 0.3 (ML), and -2.6 dorsoventral (DV). We waited at least 4 weeks after injection before behavioral experiments to allow for viral expression.

Surgical methods for fiber photometry implantation were based from protocols from Gunaydin et al., 2014. After injection of GCaMP virus, a 400/430 µm (core/outer) diameter 0.48-NA multimode fiber implant (Doric Lenses: #400/430-0.48) was slowly inserted into the mPFC until the tip of the fiber reached a DV depth of -2.25. For optogenetic behavior experiments, 200/240 µm 0.22NA dual-fiber cannulas were inserted into the mPFC at a DV depth of -2.25. Implants were affixed onto the skull using Metabond dental cement (Parkell).

The following mouse lines (7-10 weeks old) were used for behavior or photometry experiments: Vip<tm1(cre)Zjh>/J (line 010908; www.jax.org), Sst<tm2.1(cre)Zjh>/J (line 013044; www.jax.org), and B6;129P2-Pvalb<tm1(cre)Arbr>/J (line 008069; www.jax.org).

4.2.2 Fiber photometry design and analysis

The photometry apparatus was based on the design described by Gunaydin et al., 2014. A 100mW Omicron 470mW laser was optically chopped (Thorlabs, MC2000) and cleaned-up by a 470/20nm filter (Thorlabs) before hitting a 495 nm dichroic mirror (Semrock) and focused onto a custom-made 0.48-NA, 400µm multimode patch cable (Thorlabs, BFH48-400) via a FC/PC fiber collimator (Thorlabs, F240FC-A). The patch cable was friction-fit via a ferrule sleeve (Thorlabs) onto an optical fiber (Doric Lenses, #400/430-0.48) implanted into the brain as described above. A 530/20nm lens (Thorlabs) filtered the emitted light before being detected by a femtowatt photoreceiver (Newport, Model 2151). The photoreceiver was attached to a X-Y translator (Thorlabs, ST1XY-A) and adjustable lens tube (Thorlabs, SM1NR1) to assist in aligning the light path. Emitted light was focused onto the photoreceiver via a plano-convex lens (Thorlabs, F = 50.0, N-BK7) housed in the lens tube. All optical equipment were mounted onto an aluminum breadboard (Thorlabs). A lock-in amplifier (Stanford Research Systems, SR810 DSP) whose sampling interval was locked to the optical chopper filtered the signals from the photoreceiver. A digital acquisition board (Labjack) streamed the data onto a personal computer for off-line data analysis.

For calculating mean GCaMP signals during eventual open vs. closed arm runs, an observer scored each run (as an eventual open vs. closed arm run) and marked the frames where

the animal initiated its run, entered/exited the center zone, and ended its run. The observer was blinded to the corresponding GCaMP signals during this analysis.

4.2.3 Optogenetic assessment of anxiety behaviors

After sufficient time for surgical recovery and viral expression, mice underwent multiple rounds of habituation. Mice were habituated to touch with at least 3 days of handling for ~5 min each day, followed by 1-2 days of habituation to the optical tether in their home cage for 10 min. Next, mice were placed into a larger housing cage for 1-2 days for 10 min where they habituated to the tether as they explored the novel environment.

After habituation, mice were assessed for anxiety behaviors using open field (OF) and elevated plus maze (EPM) assays. Both OF and EPM sessions lasted 9 minutes, with the laser stimulation delivered during the second three-minute epoch to activate either ChR2 (473nm, 5ms pulses, 10-15mW total) or Arch (6-8mW total). Real-time optogenetic stimulation was based on the location in the EPM apparatus, with the stimulation zones demarcated as the open arms, center zone, and the closed arm zone proximal (within one quarter-length) to the center zone.

A USB webcam (Logitech) connected to a computer running ANY-maze (Stoelting) was used to track the position of the mouse in behavioral apparatuses, trigger optogenetic stimulation, and sync electrophysiology data to animal position. Behavioral data (e.g. time spent in open arm, open arm entries, etc.) was collected by ANY-maze, and additional analyses were performed offline using custom MATLAB code. The sample sizes of our cohorts are in ranges commonly found in experiments using elevated plus maze to assay anxiety-like behaviors. Animals were randomly assigned to a virus cohort (ChR2 vs eArch vs eYFP), and the experimenter was blinded to each mouse's virus assignment when the behavioral assessment was performed.

4.2.4 Slice preparation and in vitro recording parameters

Slice preparation and intracellular recording followed our published protocol (Sohal and Hugenard, 2005). Briefly, we cut 250 μm coronal slices from 8- to 11-week-old mice of either sex and secured the tissue onto the recording platform using a harp. Whole-cell patch recordings were obtained from VIP cells expressing fluorophore-labeled opsins or visually identified pyramidal cells in layer II/III of infralimbic or prelimbic cortex using differential contrast video microscopy on an upright microscope (BX51WI; Olympus). Recordings were made using a Multiclamp 700A (Molecular Devices). Patch electrodes (tip resistance = 1–4 MOhms) were filled with the following (in mM): 130 K-gluconate, 10 KCl, 10 HEPES, 10 EGTA, 2 MgCl, 2 MgATP, and 0.3 NaGTP (pH adjusted to 7.3 with KOH). All recordings were at 32.0±1°C. Series resistance was usually 10–20 MΩ, and experiments were discontinued above 25 MΩ.

The Vip<tm1(cre)Zjh>/J (line 010908; www.jax.org) mouse line was used for slice experiments.

A light-emitting LED engine (Lumencor) was used to elicit photo-induced currents. We stimulated ChR2-infected fibers or cell bodies with ~1-3 mW of 470 nm light with pulses of 5 ms in duration. eArch-infected cell bodies were stimulated with ~4-5 mW of 550/15 nm light. The light path was delivered to the slice via a 40x objective (Olympus) and illuminated across the full high-power (40x) field.

For patch-clamp experiments measuring the effects of VIP interneuron inhibition on responses to theta frequency stimulation of vHPC inputs, VIP-ires cre mice were injected with 2x 0.450ul of AAV5-EF1a-DIO-eNpHR3.0-mCh (“eNpHR”; DV: -2.3, -2.6; UNC Virus Core) using the stereotactic coordinates for mPFC listed earlier, and 0.650ul of AAV5-CaMKII-ChR2-

eYFP into the vHPC (-3.25 AP, 3.1 ML, -4.1 DV). Coronal slices were prepared ~5 weeks later. To increase the spontaneous network activity in vitro, active aCSF (3.5mM KCl, 11mM glucose, 123mM NaCl, 1.25 NaH_2PO_4, 1mM $MgCl_2$, 1mM $CaCl_2$, 1mM $MgSO_4$) was washed on for five minutes after initiating each recording from a layer 2/3 pyramidal neuron. We targeted visually-identified layer 2/3 pyramidal neurons adjacent to eNpHR-infected VIP neurons for recording (Fig 3E). The optogenetic stimulation protocol comprised of 80sec long sweeps. Each sweep was broken up as follows: a 10 sec period of ChR2 stimulation (1-5mW, 5ms light flashes delivered at 10 or 25Hz using a LED engine (Lumencor) emitting 440/20 nm and 470/24nm), followed by a 30sec recovery period, then another 10 sec period of concurrent ChR2 + eNpHR stimulation (constant 2mW light, with the LED engine emitting 640/30nm). DC current (20-60pA) was injected to elicit submaximal levels of spiking. Cells with unstable resting membrane potentials were excluded from analyses.

For patch-clamp experiments verifying levels of cross-activation by GCaMP excitation wavelength on halorhodopsin photocurrents, VIP-ires-cre mice were injected with 2x 0.450ul of AAV5-EF1a-DIO-eNpHR3.0-mCh (DV: -2.3, -2.6; UNC Virus Core) using mPFC stereotactic coordinates described earlier, and coronal sections were harvested ~5 weeks later. We then patched clamped prefrontal VIP neurons infected with Cre-dependent halorhodopsin while administering light approximating in vivo recording conditions: GCaMP excitation light (470nm, 200uW) and halorhodopsin excitation light (640/30nm, 2.25mW). Our LED engine was unable to deliver greater than 2.25mW of 600nm light in vitro.

4.2.5 Surgery and analysis of LFP experiments

Following virus injection, standard-tip 0.5 MΩ-impedance stainless steel electrodes (Microprobes, SS30030.5A10) were inserted into the mPFC, vHPC, and BLA. For the mPFC location, an optrode (optical fiber + electrode) was custom-made by affixing the electrode to the right optical fiber of a dual-fiber cannula. The tip of the electrode protruded beyond the fiber tip by 200-500 μm. The coordinates for vHPC and BLA were as follows: vHPC, -3.25 (AP), 3.1(ML), -4.1 (DV); BLA, -1.34 (AP), 3.12 (ML), -4.74 (DV). A common reference screw was implanted into the cerebellum (500 μm posterior to lambda) and a silver ground wire was placed underneath the left lateral scalp. After affixing the electrodes in place using Metabond, connections were made to the headstage of a multi-channel recording system (Pinnacle). All channels shared a common reference (cerebellum). Data was collected at 2000 Hz and band-pass filtered 1-200Hz at the pre-amp.

Analysis of LFP data was facilitated using Chronux toolbox (Chronux.org) and custom MATLAB code. Coherence calculations between electrode pairs were measured using coherencyc (Chronux). For measurements of amplitude and phase, the LFP signals were FIR-filtered (filter length 3x period corresponding to minimum frequency of frequency band) and Hilbert transformed to yield the instantaneous amplitudes (magnitude) and phases (angle). The strength of phase-locking and the phase-locking angle between two signals were calculated by the magnitude and angle of the instantaneous phase difference, respectively. Correlations for instantaneous amplitudes and phase-locking were obtained using a window size 10 times the central frequency of each frequency band. One mouse was excluded from all analyses because of a defect in the installation of the electrodes, which resulted in uniform and complete coherence (i.e., coherence equal to one) across all three electrode pairs.

4.2.6 Surgery and analysis of optogenetic endoscope experiments

For endoscope experiments, 4x 0.150ul of AAV1-Syn-GCaMP6m (DV: -2.0, -2.25, -2.5, -2.75; diluted 1:4; UPenn Virus Core) and 2x 0.450ul of AAV5-EF1a-DIO-eNpHR3.0-mCh (DV: -2.3, -2.6; UNC Virus Core) were injected into the mPFC using stereotactic coordinates described earlier. Following viral injection, a 0.5mm diameter x 6.1mm long GRIN lens (Inscopix) was slowly advanced into the mPFC until the tip was placed at DV -2.25 and cemented in place with Metabond dental cement. After 2-3 weeks of viral expression, an imaging baseplate was positioned over the GRIN lens and cemented in place. The mice were allowed to recover for another 2 weeks before the beginning of habituation.

nVistaHD software (Inscopix) was used to control the microscope and collect imaging data. Images were acquired at 20 frames per second using an imaging LED power of ~150-250 μW and stored off-line for data processing. An input TTL from a separate Anymaze computer triggered the optogenetic LED (6-8 mW) and synced imaging timestamps to positional tracking.

Imaging data was downsampled 2x in the x- and y- directions. To increase contrast for motion correction, frames were FFT bandpass filtered (3-40 pixels; ImageJ) and an unsharp mask (radius 10 pixels, 0.60 mask weight; ImageJ) was applied. Motion correction was then performed using a template-matching algorithm (normalized correlation coefficient; ImageJ) with a high-contrast subregion selected as the reference. Analysis of the dataset using a modified PCA/ICA approach (Luongo et al 2016a; Luongo et al 2016b) detected 80-90 ROIs per field of view (Fig. 4.7B).

To describe patterns of local microcircuit activity, correlation matrices of de-correlated VIP signals were calculated with a window of 2.5 sec and matched to the mouse's EPM position

(in closed vs open arm). The example closed and open arm correlation matrices in Fig. 4.7D were generated by finding the mean of twenty randomly selected correlation matrices from in-closed and in-open arm periods for one mouse. To calculate the similarity of open arm correlation matrices to other open or closed arm correlation matrices in Fig. 4.7E, we calculated the matrix dot-product of an individual open arm correlation matrix with every other open or closed arm matrix and plotted the mean matrix dot-product for open (x-axis) and closed (y-axis) arm comparisons. Thus, each point in Fig. 4.7E marks the average similarity of a given open arm correlation matrix to all other closed (y-axis) or open (x-axis) arms. Likewise, each open arm epoch was assigned either a left or right open arm position, and the similarity was computed for each left open arm correlation matrix with every right open (x-axis) or closed arm (y-axis) matrix in Fig 4.7F. Fig. 4.7G describes how the distribution of correlations with significant ($p < 0.01$) differences between closed and open arm is altered by VIP inhibition. First, open and closed arm correlation matrices were collected for each three-minute epoch. For each ROI, an unpaired student's t-test was used to determine if that given ROI had correlations that were statistically significant ($p < 0.01$) between closed and open arms. To determine the change in correlation between open and closed arms, the mean correlation of closed arms was subtracted from the mean correlation of open arms for each ROI. Thus, each panel in Fig 4.7G shows the distribution of correlations that significantly increased or decreased between closed and open arms in epoch one (top), two (middle), and three (bottom). To correlate the effect of VIP inhibition on the distribution of significantly different correlations, a correlation modulation index was calculated that is one-half the ratio of the sum of the absolute correlation change in epochs one and three to epoch two (Fig 4.7H).

4.2.7 Statistics

Unless otherwise specificed, nonparametric tests or ANOVA was used to assess signficance. The variance among cohorts (eYFP vs ChR2 vs Arch) appeared to be similar. Statistics were calculated using either custom MATLAB code or Graphpad Prism.

4.3 Results

4.3.1 Activity of prefrontal VIP neurons reflects anxiogenic regions of elevated plus maze

VIP interneurons comprise only ~2% of neurons in the neocortex; therefore, we used fiber photometry (Fig. 4.1A) (Gunaydin et al., 2014; Cui et al., 2013) to efficiently capture signals from VIP interneurons in freely moving mice (Khoshkhoo et al., 2017). Knock-in mice expressing Cre recombinase under control of the endogenous VIP promoter (VIP-ires-cre) were injected with adenoassociated-virus (AAV1) encoding a cre-dependent form of GCaMP6s (VIP GCaMP) in the mPFC. A multimode fiber for transmitting and collecting the excitation and emission wavelengths for GCaMP6 was also implanted above the site of virus injection (Fig 4.1B). We studied behaviorally-relevant modulation of VIP interneuron activity using the elevated plus maze (EPM), a common assay for innate anxiety. In the EPM, mice naturally avoid the center and exposed open arms, which are considered relatively anxiogenic, instead preferring the closed arms. Two weeks after surgery, mice were allowed to explore the EPM while we measured GCaMP signals from VIP interneurons using fiber photometry. Heat maps for individual mice, which plot the average VIP GCaMP signals in different regions of the EPM, showed higher VIP GCaMP signals in the center and open arms than the closed arms (Fig 4.1C). When looking at individual traces, VIP GCaMP signals appeared to closely track movement along the closed arm axis into the center or open arms of the EPM (Fig 4.1E). To quantify the relationship between VIP GCaMP signals and EPM location, we plotted the probability

distributions for VIP GCaMP signals in each EPM zone (closed, center, and open). The distributions of VIP GCaMP signals were skewed to the right, indicating higher GCaMP signals, in the open arms and center compared to the closed arms (Fig 4.1D). This difference was specific for VIP interneurons; differences between GCaMP signals in the open vs. closed arms were markedly smaller for somatostatin (SOM) or parvalbumin (PV) interneurons (Fig 4.2A).

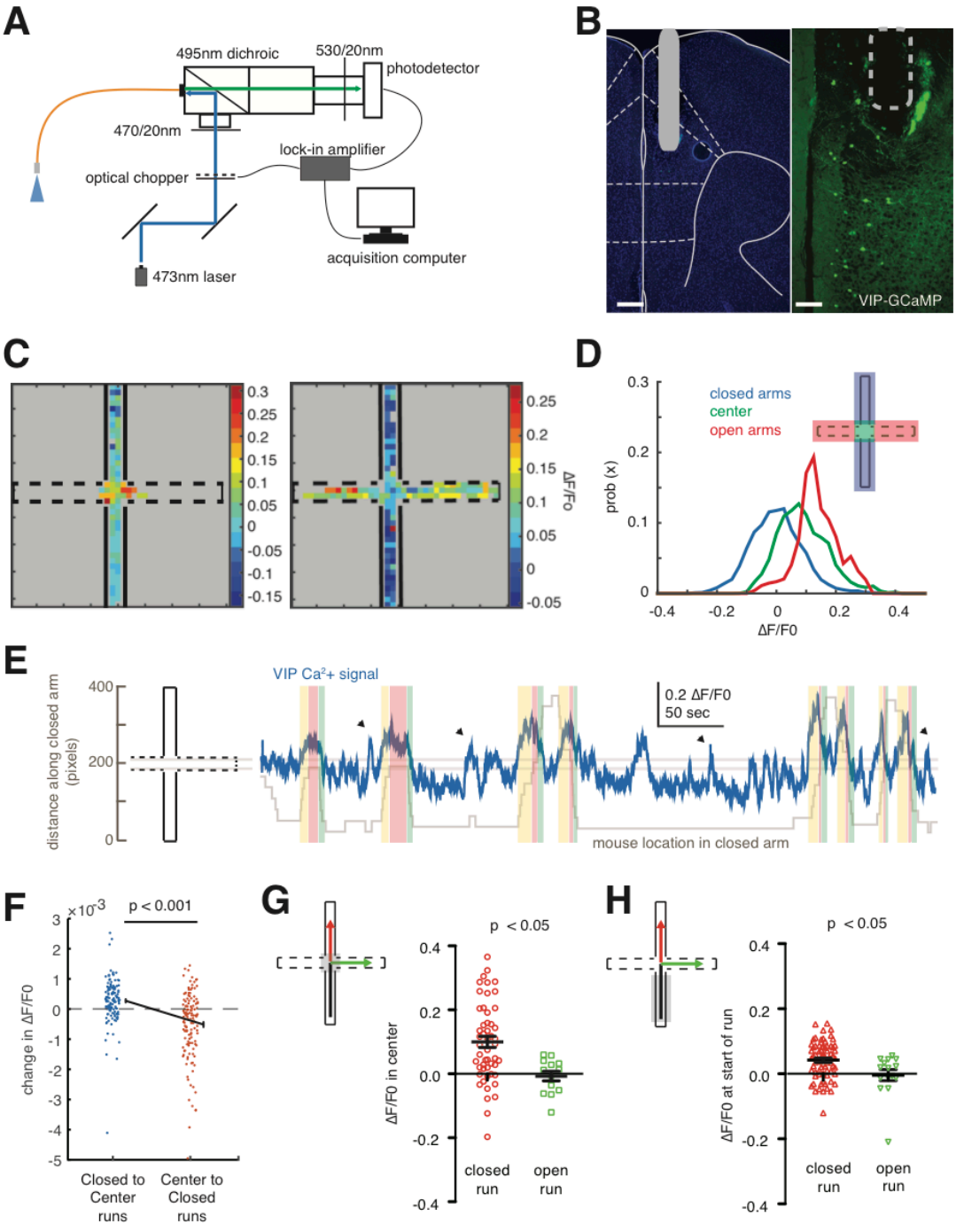

Figure 4.1. The population activity of prefrontal VIP neurons reflects behavior in the elevated plus maze.

(A) Fiber photometry design. 473nm light was delivered to the mPFC via a fiberoptic patch cable to excite the genetically encoded calcium indicator GCaMP6s. GCaMP6s fluorescence was detected and streamed to an acquisition computer using a lock-in

amplifier synchronized to an optical chopper. **(B)** VIP-ires-cre mice were injected with a cre-dependent AAV-hSyn-FLEX-GCaMP6s virus. A 400μm optical fiber was implanted with its tip near the prelimbic/infralimbic border (left, DAPI; right, VIP-GCaMP; scale bars, 300 and 90 μm, respectively). **(C)** Heatmaps showing the average GCaMP signal from VIP neurons in individual mice as a function of location within the elevated plus maze (EPM). VIP GCaMP signals were highest in the center zone for a mouse that did not explore the open arms (left); for a mouse that did explore the open arms, VIP GCaMP signals were highest in the open arms (right). **(D)** Distributions of GCaMP signals (dF/F0) from VIP neurons obtained within different zones of the EPM. Each distribution was calculated for times when the mouse was either in the closed arms (blue), center zone (green), or open arms (red), and plotted as a probability distribution function (n = 5 mice). **(E)** An example trace showing GCaMP signals from VIP neurons in a mouse during EPM exploration. The GCaMP signal (blue) is overlaid on top of the position of the mouse along the closed arm axis (grey). The middle two horizontal lines demarcate the center zone of the EPM. The population activity of VIP neurons largely tracks the position of the mouse (yellow, approach towards center zone; red, in center zone; green, exit from center zone). Arrowheads correspond to moments when the mouse was rearing or reorienting within the closed arm. **(F)** VIP neuron GCaMP signals as mice either entered or exited the center zone of the EPM. VIP activity was higher during closed-to-center runs compared to center-to-closed runs ($F_{1,9} = 50.1$, $p < 0.001$; n = 10 mice). **(G)** Average VIP neuron GCaMP signals in the center zone, depending on whether mice subsequently entered a closed or open arm. VIP GCaMP signals were lower just prior to runs into the open arms than runs into the closed arms ($F_{1,55} = 4.14$, $p = 0.047$; n = 8 mice). **(H)** VIP neuron GCaMP signals just before entry into the center zone, depending on whether mice subsequently entered a closed or open arm. VIP GCaMP signals were lower during runs on which mice subsequently entered the open arms compared to those on which mice subsequently entered closed arms ($F_{1,77} = 4.1$, $p = 0.046$; n = 8 mice).

Closer examination of Fig. 4.1E suggests that VIP GCaMP signals first rise as mice approach the center of the EPM, then fall sharply as mice run through the center. We quantified

this, and found that VIP GCaMP signals were significantly higher during runs in which mice were approaching the center chamber (closed-to-center run), and lower when mice were exiting the center (center-to-closed run) (Fig 4.1F; $F_{1,9} = 50.1$, $p < 10^{-3}$). Importantly, although VIP interneuron activity can be linked to the speed of locomotion (Fig 4.2B) (Fu et al., 2014), we did not find any relationship between speed and prefrontal VIP GCaMP signals when mice were in the EPM (Fig 4.2C). Comparison of the two VIP GCaMP heatmaps in Fig. 4.1C suggested an interesting possibility. The heatmap on the left corresponds to a mouse with minimal open arm exploration, and shows relatively high VIP GCaMP signals in the center chamber. By contrast, the heatmap on the right corresponds to a mouse that extensively explored the open arms; in this case, VIP GCaMP signals increased only modestly in the center chamber, and maximal signals were only observed near the edges of the open arms (Fig 4.1C). These patterns suggest that differences in VIP GCaMP signals may actually predict the extent of open arm exploration. To test this possibility, we identified all runs from a closed arm to the center, then classified each run according to whether the mouse subsequently entered a closed or open arm (closed-center-closed vs. closed-center-open runs). We first compared VIP GCaMP signals in the center chamber during closed-center-closed vs. closed-center-open runs. The VIP GCaMP signals in the center chamber were significantly lower for closed-center-open runs compared to closed-center-closed runs (Fig 4.1G; ANOVA using mouse and trajectory type as factors, $F_{1,55} = 4.14$, $p = 0.047$; n = 8 mice). We also looked further back in time, by comparing VIP GCaMP signals in the closed arm prior to entry into the center chamber. Again, VIP GCaMP signals were significantly lower for closed-center-open vs. closed-center-closed runs (Fig 4.1H; $F_{1,77} = 4.1$, $p = 0.046$).

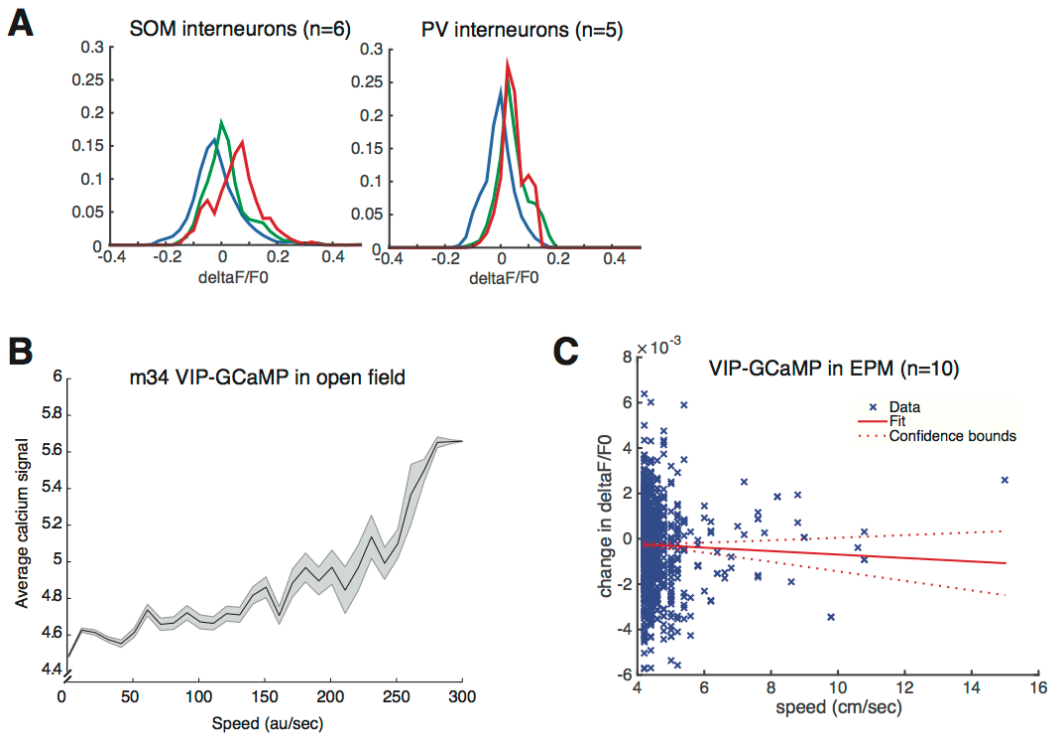

Figure 4.2. Photometry of non-VIP interneurons and effects of locomotion speed on calcium signal

(A) Distribution of prefrontal GCaMP signals from SOM interneurons (left, n = 6 animals) and PV interneurons (right, n = 5) during EPM exploration. **(B)** Example plot from a VIP-GCaMP mouse showing prefrontal GCaMP signals and locomotion speed in the open field. **(C)** Prefrontal GCaMP signals from VIP-GCaMP mice do not correlate with locomotion speed in the EPM (n = 10).

4.3.2 Inhibition of prefrontal VIP neurons increases open arm exploration in elevated plus maze

Since decreased VIP GCaMP signals predict subsequent exploration of the open arms in the EPM, we hypothesized that VIP interneurons may influence decisions to explore the open arms. To test for such a causal role of VIP interneurons in the EPM, we performed real-time optogenetic manipulations of VIP interneuron activity. Bilateral-fiberoptic implants were inserted into the mPFC of VIP-ires-cre mice injected with cre-dependent channelrhodopsin

(AAV5-DIO-hChR2-eYFP), archaerhodopsin (AAV5-DIO-eArch3.0-eYFP), or eYFP (AAV5-DIO-eYFP) (Fig 4.3A). ChR2 and Arch induced reliable excitatory and inhibitory responses in VIP interneurons *in vitro* (Fig 4.3B). Because VIP GCaMP signals specifically increased in the center and open arms of the EPM, we triggered optical activation of ChR2 or Arch whenever the mouse entered a "stimulation zone" comprising the center chamber and open arms. We then compared the behavior of mice in the EPM during three, three-minute-long epochs: light OFF, followed by light ON, followed by light OFF (Fig 4.3C). During the light ON epoch, there was a significant increase in relative time spent in the open arms and open arm entries in VIP-Arch mice compared to VIP-ChR2 mice or VIP-eYFP cohorts (Fig 4.3D; for open arm time: main effect of virus, $F_{2,108} = 4.72$, $p = 0.011$; during light ON epoch, $p < 0.05$ for VIP-Arch vs ChR2 and VIP-Arch vs VIP-eYFP; for open arm entries: main effect of virus, $F_{2,105} = 7.87$, $p < 0.001$; during light ON epoch, $p < 0.05$ for VIP-Arch vs VIP-ChR2, $p < 0.001$ for VIP-Arch vs VIP-eYFP). The change in time spent in the open arms in the light ON epoch compared to the preceding light OFF epoch was significantly greater for VIP-Arch mice (% change in open arm time: 176%±64) compared to VIP-ChR2 mice (14%±21) or VIP-YFP cohorts (32%±30) (Fig 4.3E; $F_{2,36} = 4.05$, $p = 0.026$; $p < 0.05$, Newman-Keuls Multiple comparison test). Finally, the time spent in the open arms was significantly greater during the light ON epoch than the preceding light OFF epoch for VIP-Arch mice (Fig 4.3F; $p = 0.003$, paired t-test, $n = 14$) but not for VIP-ChR2 mice ($p = 0.90$, $n = 12$) or VIP-eYFP controls ($p = 0.76$, $n = 13$). Interestingly, in VIP-Arch mice, open arm entries seemed to remain elevated during the light OFF epoch that followed the light ON epoch (Fig 4.3D; $p < 0.05$ for VIP-Arch vs VIP-eYFP). Notably, inhibition of VIP interneurons using Arch did not affect open arm exploration when light was

delivered throughout a 3-minute epoch, rather than triggered by entries into the center or open arms (Fig 4.4).

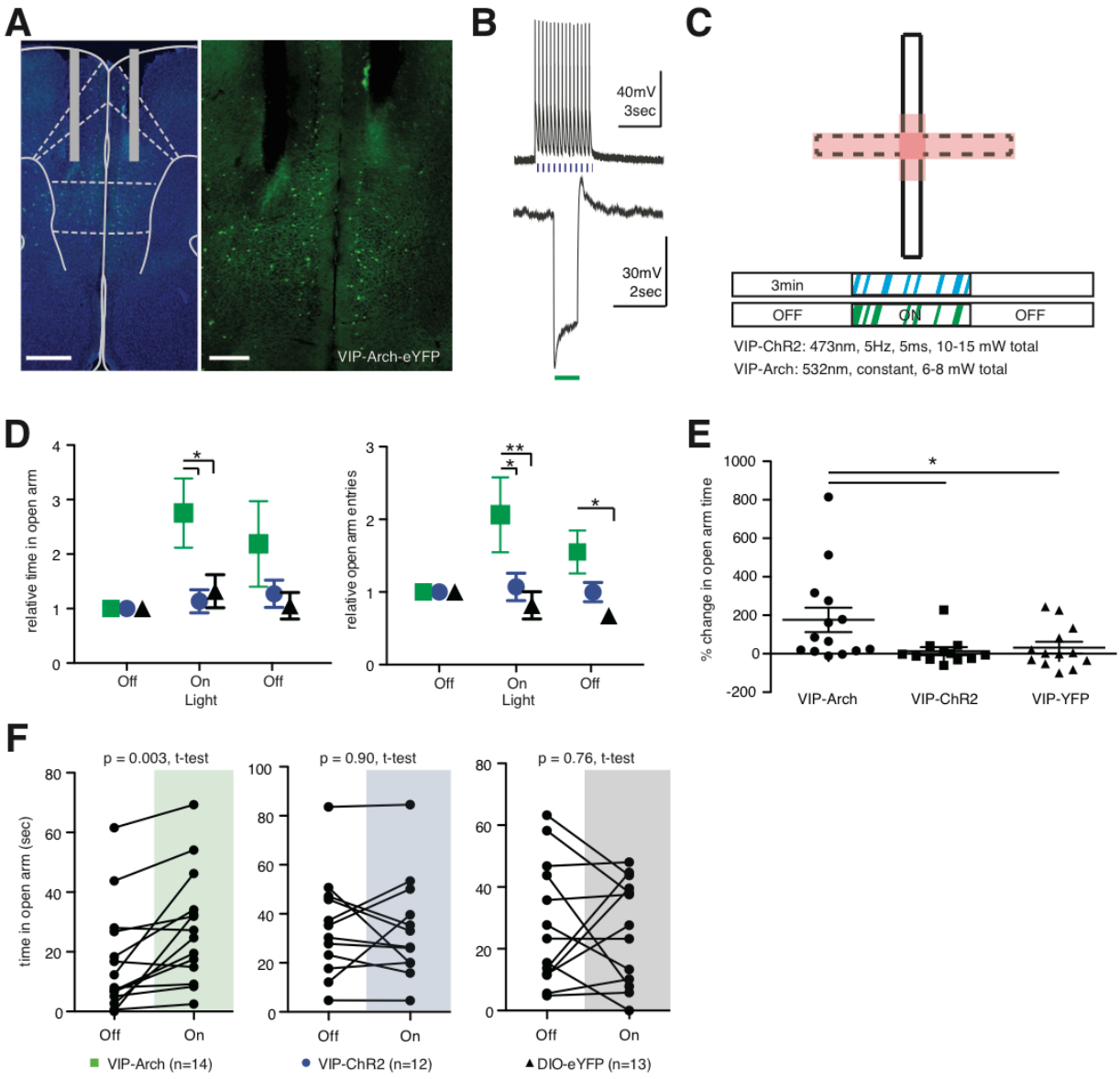

Figure 4.3 Inhibiting prefrontal VIP neurons increases open arm exploration

(A) Placement of dual-fiberoptic implants in the mPFC, with their tips near the prelimbic/infralimbic border, in VIP-ires-Cre mice injected with AAV to drive cre-dependent expression of ChR2 or Arch (scale bars, 500 and 250 μM, respectively). **(B)** *In vitro* current clamp responses of VIP neurons expressing ChR2 or Arch. Example responses of prefrontal VIP neurons to 5 ms pulses of 473nm light (~3mW) or constant

532nm green light (~5mW) to stimulate ChR2 or Arch, respectively. **(C)** Protocol for "real-time" optogenetic stimulation in the EPM. Optogenetic stimulation was triggered when the mouse entered the stimulation zone (red) during the second 3-minute epoch of EPM exploration. **(D-F)** Effects of optogenetic manipulations of VIP neurons on open arm exploration. **(D)** Inhibiting VIP neurons (green) increased the relative open arm time (left) and number of open arm entries (right) compared to control mice or mice receiving optogenetic stimulation of VIP neurons (*$p < 0.05$, **$p < 0.01$; for open arm time: main effect of virus, $F_{2,108} = 4.72$, $p = 0.011$; for open arm entries: main effect of virus, $F_{2,105} = 7.87$, $p < 0.001$). Open arm time and entries were normalized to the first 3-minute epoch of EPM exploration. **(E)** During the period of light stimulation, VIP-Arch mice increase the absolute time they spent in open arms more than VIP-ChR2 or VIP-YFP mice (*$p < 0.05$). **(F)** Inhibiting VIP neurons (green) increased the time spent in the open arm, compared to the first 3 minutes of EPM exploration, when no light was delivered. There was no significant change in open arm time for mice in which we optogenetically stimulated VIP neurons, or for control mice (VIP-Arch: p = 0.003, n = 14 mice; VIP-ChR2: p = 0.90, n = 12 mice; VIP-eYFP: p = 0.76, n = 13 mice; paired t-test).

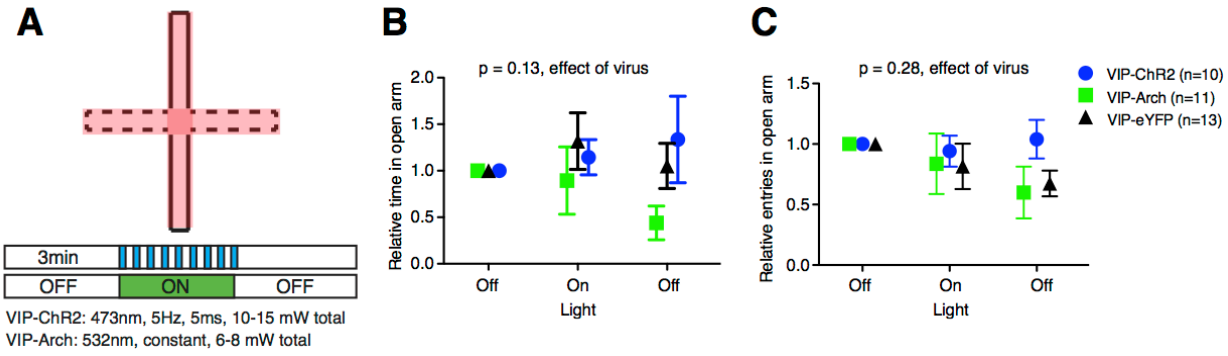

Figure 4.4. Constant, time-based VIP inhibition did not result in increased open arm exploration

(A) Experimental design: non-triggered optogenetic stimulation or inhibition was delivered throughout the second three-minute epoch, regardless of the position of the

mouse. **(B)** Non-triggered activation or inactivation of prefrontal VIP neurons did not cause significant changes in relative time spent in the open arms (p = 0.13, effect of virus). **(C)** Non-triggered activation or inactivation of prefrontal VIP neurons did not significantly alter the relative number of entries into the open arms (p = 0.28, effect of virus).

4.3.3 Prefrontal VIP inhibition disrupts vHPC-PFC theta synchrony

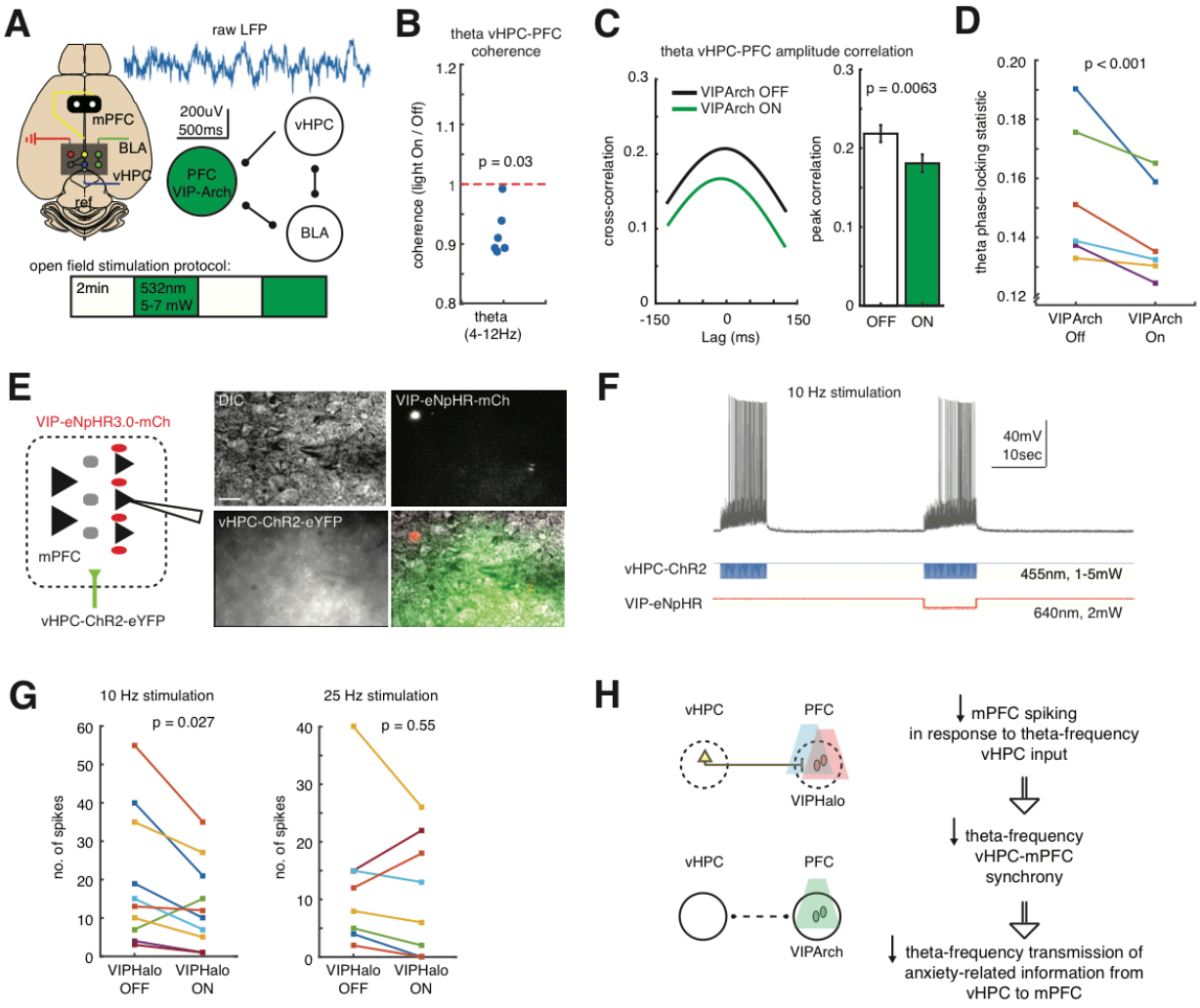

Figure 4.5. Inhibiting prefrontal VIP neurons disrupts theta-frequency synchronization between vHPC-mPFC and spike probability from theta-band vHPC inputs.

(A) Experimental design. Local field potentials were recorded from electrodes inserted into the mPFC, vHPC, and BLA of VIP-Arch mice implanted with bilateral prefrontal optical fibers. During open field exploration, VIP-Arch was activated during the second and fourth 2 min-long epochs (532nm, ~5-7 mW bilaterally). **(B)** Theta-frequency (4-12 Hz) vHPC-mPFC coherence was decreased by inhibition of prefrontal VIP neurons ($p = 0.03$, signed-rank test; $n = 6$ mice). **(C)** Left, the cross-correlogram for vHPC-PFC instantaneous theta-frequency amplitudes, averaged across experiments, in the presence or absence of inhibition of VIP neurons. Right, the peak cross-correlation of vHPC-PFC theta (4-12 Hz) amplitudes was reduced by inhibition of prefrontal VIP neurons ($p < 0.01$, effect of inhibition; $n = 6$ mice). **(D)** Inhibition of prefrontal VIP neurons decreased theta phase synchrony between vHPC and mPFC ($p < 0.01$, effect of inhibition; $n = 6$ mice). **(E)** Left, Experimental design. We made patch-clamp recordings from layer 2/3 mPFC neurons in VIP-eNpHR mice co-injected with CaMKII-ChR2 in the vHPC. Right, representative DIC and fluorescence images of patch-clamp experiments. For recordings, we specifically targeted visually identified layer 2/3 pyramidal neurons that were in the vicinity of eYFP-tagged vHPC terminals (yellow-green) and mCherry-tagged VIP-eNpHR neurons (red) (scale bar, 15 μm). **(F)** Representative traces and optogenetic stimulation protocol. Current-clamp recording from a layer 2/3 pyramidal neuron that exhibits decreased spiking in response to 10Hz ChR2 stimulation of vHPC terminals during Arch-mediated inhibition of VIP interneurons. Ten seconds of vHPC-ChR2 stimulation (5ms, 455nm, 1-5mW) and ten seconds of concurrent vHPC-ChR2 and VIP-eNpHR stimulation (constant, 640nm, 2mW) were separated by a 30 second interval. ChR2 pulses were delivered at either 10 or 25Hz. **(G)** The number of spikes in response to 10Hz (left) and 25Hz (right) stimulation of vHPC terminals in the presence or absence of VIP neuron inhibition. Inhibition of VIP neurons caused a decrease in spiking during 10Hz but not 25Hz stimulation (10Hz: $p = 0.027$, $n = 10$ cells; 25Hz: $p = 0.55$, $n = 8$ cells; sign-rank test). **(H)** Schematic model summarizing our experiments and illustrating how prefrontal VIP neurons regulate vHPC-mPFC theta synchrony.

Having found that inhibiting VIP interneurons decreased anxiety-related avoidance in the EPM, we wondered how VIP interneuron inhibition affects electrophysiological markers of distributed network interactions that have been linked to anxiety-related avoidance in the EPM. Specifically, theta-frequency (4-12 Hz) synchronization has repeatedly been shown to be necessary for the transmission of anxiety-related information from the vHPC to the mPFC (Adhikari et al., 2010; Adhikari et al., 2011). In particular, disrupting such synchronization by optogenetically inhibiting projections from the vHPC to mPFC suppresses anxiety-related avoidance in the EPM (Padilla-Coreano et al., 2016). To study how VIP interneurons modulate this and other network interactions, we implanted stainless steel electrodes within the vHPC, BLA, and mPFC of VIP-Arch mice to measure local field potentials (LFPs; Fig 4.5A). In the mPFC, the implanted electrode was attached to the one side of a bilateral fiber optic implant to record neural activity while optically stimulating Arch in VIP interneurons. An important consideration in these experiments, which combine an acute manipulation (e.g., activating Arch) with neural recording in freely behaving mice, is that any changes in neural activity observed following the manipulation may be direct results of that manipulation which contribute to changes in behavior, or alternatively, may reflect indirect consequences of changes in behavior (Padilla-Coreano et al., 2016). In other words, when a manipulation alters behavior and neural activity, changes in activity may be consequences, rather than causes, of altered behavior. Because of this possible confound, we could not measure the effects of inhibiting VIP interneurons on vHPC-mPFC theta synchrony in the EPM, since VIP interneuron inhibition increases exploration of the open arms. Instead, we recorded in an open field (OF) environment, because inhibiting VIP interneurons did not significantly alter anxiety-related avoidance of the center of the OF (Fig 4.6A-B). This may reflect the fact that the OF is less sensitive as an assay

of innate anxiety compared to the EPM. Alternatively, decisions about exploring anxiogenic regions may be processed differently in the OF vs. EPM, due to the very different spatial configurations of these two environments. Importantly, previous studies have confirmed that theta-frequency vHPC-mPFC synchronization is normally present in the OF (Adhikari et al., 2010). Five weeks after surgery, mice explored an OF for eight minutes, and VIP interneuron inhibition occurred during minutes 2-4 and 6-8 (Fig 4.5A). We found that inhibiting VIP interneurons suppressed vHPC-mPFC theta synchrony, measured in three different ways. First, vHPC-mPFC coherence was significantly decreased in the theta band (4-12Hz) (Fig 4.5B; $p = 0.03$, signed-rank test). Second, the cross-correlation between instantaneous theta amplitudes in the vHPC and mPFC was significantly decreased (Fig 4.5C; main effect of light on crosscorrelation, $F_{1,2275} = 7.49, p = 0.0063$). Third, the phase-locking of theta-frequency activity in the vHPC and mPFC was also significantly decreased (Fig 4.5D; main effect of light on pls, $F_{1,2275} = 15.77$, $p < 10^{-4}$). Notably, these effects were both frequency and pathway-specific: inhibiting mPFC VIP interneurons did not affect vHPC-mPFC synchronization in other frequency bands (Fig. 4.6C-E) and also had minimal effects on theta-frequency synchronization between the mPFC and BLA or between the vHPC and BLA (Fig. 4.6F-H).

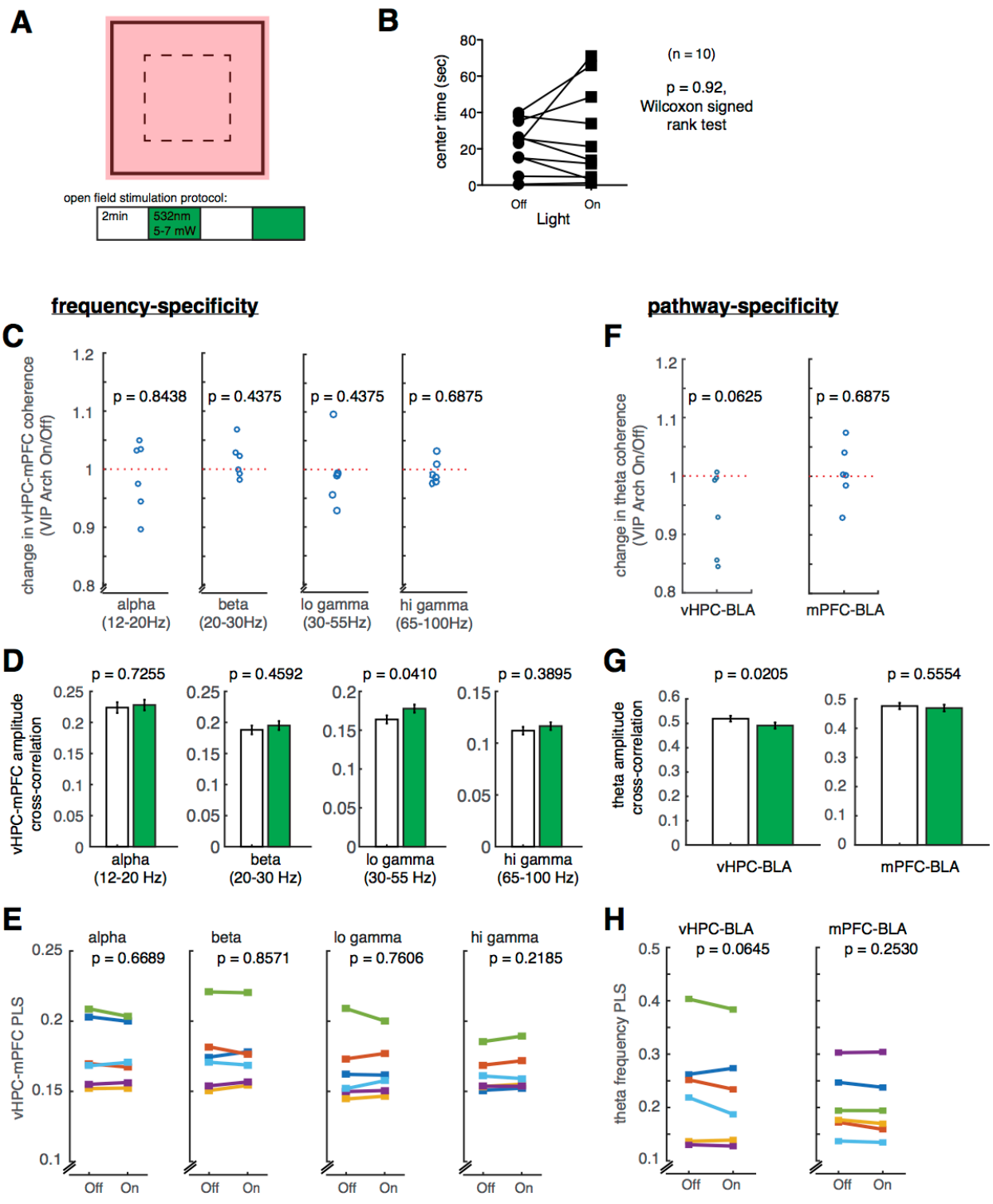

Figure 4.6. Frequency- and pathway-specificity of prefrontal VIP inhibition

(A) Experimental design: Non-triggered optogenetic inhibition was delivered throughout the second and fourth two-minute epochs. **(B)** Time in center of open field. Continuous

optogenetic inhibition of prefrontal VIP neurons did not change the amount of time spent in the center zone ($p = 0.92$, signed-rank test; $n = 10$ animals). **(C)** Frequency-specificity of the effect of prefrontal VIP neuron inhibition on vHPC-mPFC theta band coherence. Coherences across other frequency bands (alpha, beta, low gamma, high gamma) do not change during inhibition of prefrontal VIP neurons (alpha, $p = 0.84$; beta, $p = 0.44$; lo gamma, $p = 0.44$; hi gamma, $p = 0.69$; signed-rank test, $n = 6$ mice). **(D)** Frequency-specificity of prefrontal VIP inhibition on vHPC-mPFC amplitude cross-correlations. Cross correlations of amplitudes for activity outside the theta band are not strongly affected by prefrontal VIP neuron inhibition (alpha, $p = 0.73$; beta, $p = 0.46$; low gamma, $p = 0.04$; hi gamma, $p = 0.39$; effect of light on peak cross-correlation, $n = 6$ mice). **(E)** Frequency-specificity of the effect of prefrontal VIP neuron inhibition on vHPC-mPFC phase-locking. Non-theta band phase-locking is not strongly affected by prefrontal VIP neuron inhibition (alpha, $p = 0.67$; beta, $p = 0.86$; lo gamma, $p = 0.76$; hi gamma, $p = 0.22$; effect of light on PLS; $n = 6$ mice). **(F)** Pathway-specificity of the effect of prefrontal VIP neuron inhibition on theta band coherence. vHPC-BLA and mPFC-BLA coherence in the theta band do not change during inhibition of prefrontal VIP neurons (vHPC-BLA, $p = 0.06$; mPFC-BLA, $p = 0.69$, signed-rank test; $n = 6$ mice). **(G)** Pathway-specificity of the effect of prefrontal VIP inhibition on the cross correlation of theta amplitudes between the vHPC and mPFC. Cross correlation of theta amplitudes between the mPFC and BLA is not affected by inhibition of prefrontal VIP neurons. The cross correlation of theta amplitudes between the vHPC and BLA shows a marginal reduction during inhibition of prefrontal VIP neurons (6% reduction for vHPC-BLA vs. 18% reduction for vHPC-mPFC) (vHPC-BLA, $p = 0.02$; mPFC-BLA, $p = 0.56$; effect of light on peak cross-correlation, $n = 6$ mice). **(H)** Pathway-specificity of prefrontal VIP inhibition on theta frequency phase-locking. vHPC-BLA and mPFC-BLA theta frequency phase locking do not show strong changes during VIP neuron inhibition (vHPC-BLA, $p = 0.06$; mPFC-BLA, $p = 0.25$; effect of light on PLS, $n = 6$ mice).

We next looked for microcircuit-level mechanisms that could explain this effect of VIP interneuron inhibition on vHPC-mPFC theta synchrony. For this, we made whole cell patch

clamp recordings from layer 2/3 pyramidal neurons in acute mPFC slices from VIP-ires-cre mice injected with two viruses: one to drive cre-dependent expression of halorhodopsin (VIP-eNpHR) in the mPFC, and a second to express ChR2 in excitatory neurons within the vHPC (vHPC-ChR2; Fig 4.5E). By simultaneously modulating ChR2 in vHPC-mPFC terminals and eNpHR within mPFC VIP interneurons, we could test whether VIP inhibition alters prefrontal microcircuit responses to vHPC inputs at various frequencies. Optogenetic stimulation of ChR2-positive vHPC terminals was triggered by blue light flashes (5 ms) at theta (10 Hz) and non-theta frequencies (25 Hz) with or without concomitant optogenetic inhibition of VIP interneurons (Fig 4.5F). We found that spiking of layer 2/3 mPFC neurons in response to 10 Hz vHPC input was reduced by VIP inhibition (Fig 4.5G, left; $p = 0.027$, sign-rank test, $n = 10$). By contrast, VIP inhibition did not affect spiking of layer 2/3 mPFC neurons in response to 25 Hz stimulation of vHPC terminals (Fig 4.5G, right; $p = 0.55$, sign-rank test, $n = 8$).

4.3.4 Prefrontal VIP neurons attenuate anxiety-related changes in patterned activity

We divided each dataset into 2.5 sec epochs, calculated the pattern of correlations during each epoch, and classified each epoch based on whether the mouse was in the closed arms, open (left vs right) arms, or center chamber. For example, Fig 4.7D is the average correlation matrix of 20 randomly chosen closed (top) and open (bottom) epochs for a given mouse during EPM exploration. This allowed us to determine whether patterns of microcircuit activity, identified as described above, correlated with behavior in the EPM. Indeed, we found that every pattern of correlations observed during an open arm epoch was more similar to other patterns of correlations observed during different open arm epochs, than to patterns observed during closed arm epochs (Fig. 4.7E, $p < 10^{-35}$, paired t-test). Importantly, this was not simply a result of open

arm epochs being clustered together in time (Fig. 4.8B). Left open arm correlations were also more similar to right open arm correlations than to closed arm correlations (Fig 4.7F, $p < 10^{-13}$, paired t-test), further confirming that this conserved pattern of correlations was not simply an artifact of clustering in time, but rather, captures anxiety-related (as opposed to purely spatial) information. Thus, patterns of prefrontal microcircuit correlations, measured via microendoscopic GCaMP imaging, encode anxiety-related signals. Finally, we determined whether inhibiting VIP interneurons alters this encoding. Indeed, when we examined the specific correlations that differ significantly between the closed and open arms, we found that the magnitude of these differences was attenuated by VIP interneuron inhibition (Fig. 4.7G), consistent with the behavioral effect of such inhibition to attenuate the preference for the closed vs. open arms. In fact, when looked on a mouse-by-mouse basis, we found a significant correlation between the degree to which VIP interneuron inhibition attenuates closed vs. open arm differences in correlations, and the degree to which that inhibition attenuates open arm avoidance (Fig 4.7H). Taken together, these results demonstrate that it is in fact useful to characterize the current state of the prefrontal microcircuit by calculating the matrix of correlations between GCaMP signals and their derivatives, as we have done. Regardless of whether the network state, defined in this way, can be traced directly back to the spiking of specific neurons, it carries anxiety-related information about whether mice are currently in the open vs. closed arms, and more importantly, about the extent to which mice behaviorally discriminate between these arms.

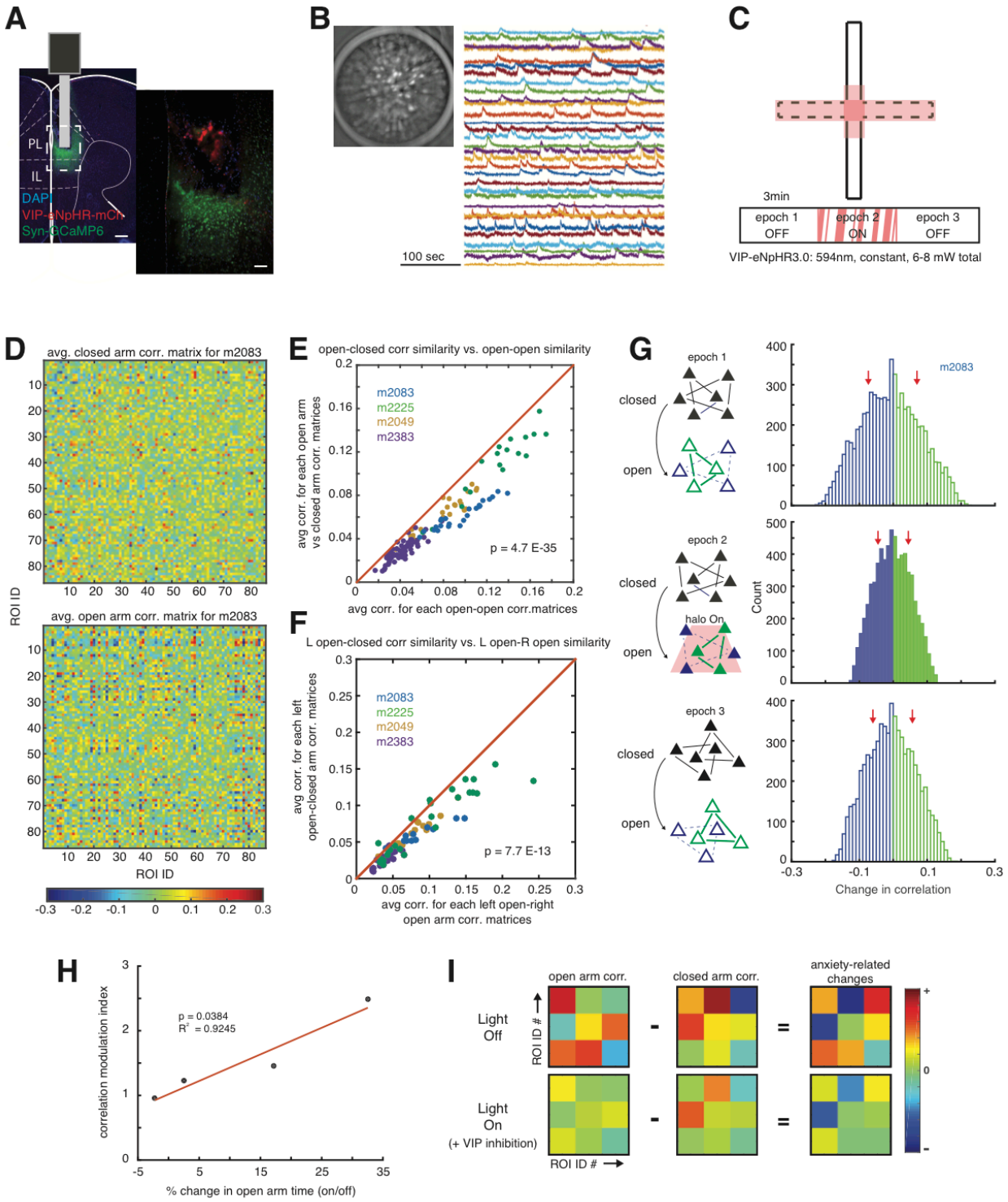
A
PL
IL
DAP
VIP-eNpHR-mCh
Syn-GCaMP6
B
100 sec
C
3min
epoch 1
OFF
epoch 2
ON
epoch 3
OFF
VIP-eNpHR3.0: 594nm, constant, 6-8 mW total
D
avg. closed arm corr. matrix for m2083
avg. open arm corr. matrix for m2083
ROI ID
E
open-closed corr similarity vs. open-open similarity
m2083
m2225
m2049
m2383
p = 4.7 E-35
avg corr. for each open arm vs closed arm corr. matrices
avg corr. for each open-open corr.matrices
F
L open-closed corr similarity vs. L open-R open similarity
p = 7.7 E-13
avg corr. for each left open-closed arm corr. matrices
avg corr. for each left open-right open arm corr. matrices
G
epoch 1
epoch 2
epoch 3
closed
open
halo On
m2083
Count
Change in correlation
H
p = 0.0384
R2 = 0.9245
correlation modulation index
% change in open arm time (on/off)
I
open arm corr.
closed arm corr.
anxiety-related changes
Light Off
Light On
(+ VIP inhibition)
ROI ID #

Figure 4.7. Inhibiting VIP neurons attenuates anxiety-driven changes in patterns of mPFC microcircuit activity

(A) A 500um diameter GRIN lens was implanted into the mPFC of VIP-cre mice injected with AAV-DIO-eNpHR3.0-mCh to drive eNpHR expression within VIP neurons, and AAV-Syn-GCaMP6m to drive pan-neuronal expression of the calcium indicator. The tip of the GRIN lens was located in ventral PL cortex (scale bars, 300 and 100 μm, respectively). **(B)** Representative calcium signals. Max-projected Z-stack (1000 frames; 50 sec) of Syn-GCaMP6m-infected cells in mPFC (left) and calcium signals from regions-of-interests (ROIs) detected using PCA/ICA (right). **(C)** Experimental design. Optogenetic inhibition (594nm, 6-8mW total) was triggered when the mouse entered the stimulation zone (red shading) during the second 3min epoch. **(D)** Averaged correlation matrix representing sample patterns of microcircuit activity in the closed vs. open arms. Twenty random correlation matrices (from one mouse) were averaged for times corresponding to exploration of the closed (top) or open (bottom) arms. **(E)** Similarity of correlations in open arms to closed arms. For each correlation matrix corresponding to periods (2.5 sec window) of open arm exploration, we computed the similarity between that matrix and other correlation matrices corresponding to exploration of either closed (y-axis) or open (x-axis) arms. Every point falls below the unity line, indicating that all open arm correlation matrices were more similar to other open arm matrices, than to closed arm correlation matrices ($p < 10^{-35}$, paired t-test). Different colors indicate data from different mice (n = 4 mice). **(F)** Similarities of left open arms to right open arms and closed arms. For each left open arm exploration correlation matrix, we computed the similarity between that matrix and other correlation matrices corresponding to exploration of either closed (y-axis) or right open (x-axis) arms. The majority of left open arm matrices were more similar to right open arm matrices than closed arm matrices ($p < 10^{-13}$, paired t-test), indicating that the similarity of open arm correlations are not simply reflecting clusters of time and suggests that the structure of mPFC activity reflects anxiety state vs. positional information. Different colors indicate data from different mice (n = 4 mice). **(G)** The distribution of correlations (from one mouse) which exhibit significant ($p < 0.01$) increases (green) or decreases (blue) between the closed and open arm during the first (top), second (middle), or third (bottom) 3-min epoch. The magnitude

of significant closed vs. open arm changes in correlations is reduced when VIP interneurons are inhibited, during the second epoch. For each epoch, red arrows indicate the mean increase or decrease in correlations. **(H)** Mice with increased open arm exploration during the period of VIP neuron inhibition also exhibit a greater reduction in the magnitude of correlation changes between the open and closed arms ($p = 0.0384$, $R^2 = 0.9245$; $n = 4$ mice). **(I)** Model of VIP inhibition and patterning of prefrontal activity. Inhibition of VIP neurons attenuates anxiety-related changes (open - closed arm correlations) in the prefrontal cortex.

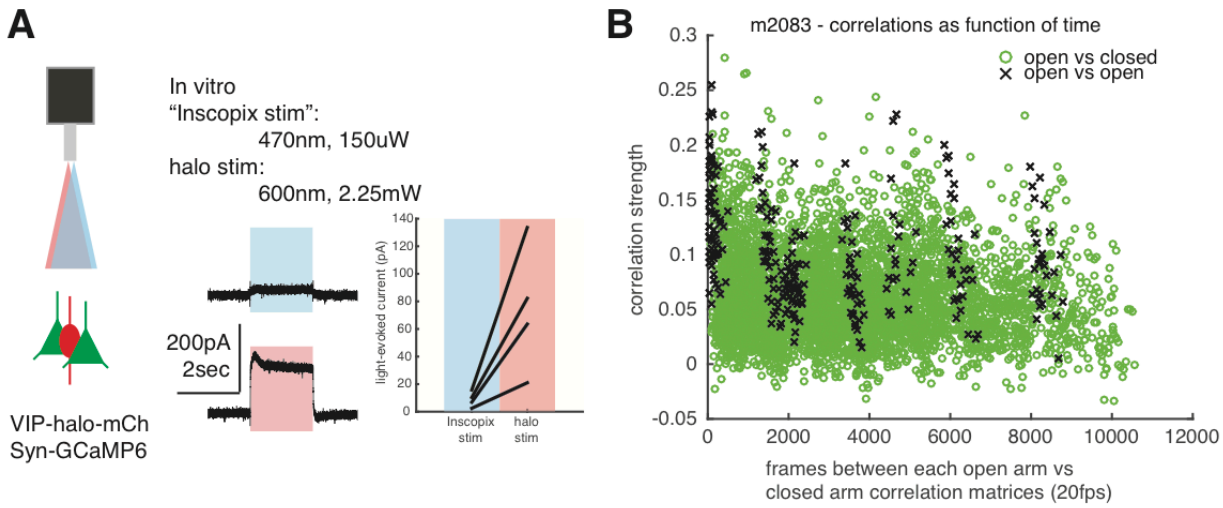

Figure 4.8. Cross-activation of Inscopix light on halorhodopsin and effect of correlation strength as function of time

(A) Effect of the excitation wavelength (470nm) for GCaMP on halorhodopsin-infected VIP cells. Light for GCaMP excitation induced minor photo-currents when compared to direct activation of halorhodopsin by 600nm light. To quantify amount of photo-induced inhibitory current due to cross-spectral halorhodopsin activation, we patch clamped prefrontal VIP neurons infected with Cre-dependent halorhodopsin while administering calcium excitation light (470nm, 200uW) and halorhodopsin excitation light (600nm, 2.25mW). This paradigm would be expected to overestimate the relative effects of cross-spectrum activation because the Inscopix optogenetic microendoscope actually delivered even stronger 600nm light to activate halorhodopsin (6-8mW

total). **(B)** Open-open (black Xs) vs. open-closed (green Os) correlation matrix similarity as a function of the number of frames (20 fps) between the two epochs (either both open or open and closed). As shown by this data from one mouse, the greater similarity between open-open correlation matrix pairs, compared to open-closed matrix pairs, was not simply due to their proximity in time.

4.4 Discussion

4.4.1 Prefrontal VIP neurons as participants in local and distributed anxiety networks

Previous studies have examined firing patterns of VIP interneurons in behaving mice (Pi et al., 2013; Fu et al., 2014), or shown that manipulating VIP interneurons affects neural responses to sensory stimuli (Fu et al., 2014; Karnani et al., 2016; Ayzenshtat et al., 2016), but linking changes in neural activity elicited by manipulating VIP interneurons to specific behavioral effects has been more challenging. Here, we have been able to establish such a link using fiber photometry, optogenetics, multi-site LFP recordings, in vitro patch-clamp electrophysiology, and combined optogenetic endoscope techniques. We specifically studied the role of VIP interneurons in the EPM, because this assay is sensitive to perturbations of mPFC, and correlations between mPFC activity and EPM behavior are well-established. We found that population activity of VIP interneurons reflects multiple aspects of anxiety-related EPM behavior, including current proximity to the open vs. closed arms, the direction of movement into or out of the center, and future propensity to explore the open arms. Inhibiting VIP interneurons increases open arm exploration while attenuating two neural correlates of anxiety-related avoidance. First, theta-frequency mPFC-vHPC synchronization is necessary for anxiety-related avoidance [5], and inhibiting VIP interneurons disrupts this synchronization, likely by suppressing mPFC responses to theta-frequency vHPC inputs (Fig 4.5H). Second, patterns of prefrontal microcircuit activity discriminate between the open and closed arms of the EPM, and

inhibiting VIP interneurons also disrupts this representation of anxiety-related information. Thus, even though VIP interneurons represent a small fraction (only ~2%) of PFC neurons, inhibiting them alters activity at both the local microcircuit and distributed network levels in ways that are consistent with the behavioral effect of VIP interneuron inhibition to reduce anxiety-related avoidance.

4.4.2 Correlation analysis of microendoscope imaging

To study prefrontal microcircuit representations of anxiety-related information, we introduced a new method for analyzing GCaMP datasets obtained via microendoscope imaging. Conventional analyses of these datasets rely on detecting "events" – large changes in fluorescence, presumably corresponding to bursts of spikes. This approach would be problematic here because such events are temporally sparse, creating problems with undersampling when the behaviors being studied, e.g., open arm entries, are rare and brief. Furthermore, event detection requires choosing parameters and making inferences about which portions of a GCaMP signal are meaningful. By contrast, the method we have introduced is unbiased and computes correlations using the entirety of a GCaMP recording, making it possible to analyze activity corresponding to rare behavioral events. We cannot assert that our method measures correlations between spikes in different cells. However, using this method, we are able to demonstrate that anxiety-related information is represented within the prefrontal microcircuit, and that this representation is disrupted when VIP cells are inhibited.

4.4.3 Prefrontal VIP neurons and gain control

Previous work has shown that VIP interneurons modulate the gain of visual responses (Fu et al., 2014). The concept of gain is not as clearly defined for prefrontal neurons, which have more complex response properties. That being said, we show that inhibiting VIP interneurons attenuates 1) mPFC responses to theta frequency vHPC input, 2) theta-frequency mPFC-vHPC synchronization, and 3) anxiety-related changes in patterns of prefrontal microcircuit activity (Fig 4.7I). Thus, by measuring activity at the level of networks (either prefrontal microcircuits or distributed limbic networks), rather than single cells, we are able to show that VIP interneurons modulate the "gain" of prefrontal responses to an anxiogenic environment. In this way, resolving patterns of activity at the network level may reveal mechanisms through which even small neuronal populations can powerfully regulate behavior.

References

Adhikari, A., Topiwala, M. A. & Gordon, J. A. Synchronized activity between the ventral hippocampus and the medial prefrontal cortex during anxiety. *Neuron* 65, 257-269 (2010).

Adhikari, A., Topiwala, M. A. & Gordon, J. A. Single units in the medial prefrontal cortex with anxiety-related firing patterns are preferentially influenced by ventral hippocampal activity. *Neuron* 71, 898-910, doi:10.1016/j.neuron.2011.07.027 (2011).

Anderson SA, Eisenstat DD, Shi L, Rubenstein JL (1997) Interneuron migration from basal forebrain to neocortex: dependence on Dlx genes. Science 278:474-476.

Arguello A, Yang X, Vogt D, Stanco A, Rubenstein JL, Cheyette BN (2013) Dapper antagonist of catenin-1 cooperates with Dishevelled-1 during postsynaptic development in mouse forebrain GABAergic interneurons. PLoS One 8:e67679.

Ayzenshtat, I., Karnani, M. M., Jackson, J. & Yuste, R. Cortical Control of Spatial Resolution by VIP+ Interneurons. *J Neurosci* 36, 11498-11509, doi:10.1523/JNEUROSCI.1920-16.2016 (2016).

Branco, T., and Hausser, M. (2011). Synaptic integration gradients in single cortical pyramidal cell dendrites. Neuron *69*, 885-892.

Brown MT, Tan KR, O'Connor EC, Nikonenko I, Muller D, Luscher C (2012) Ventral tegmental area GABA projections pause accumbal cholinergic interneurons to enhance associative learning. Nature 492:452-456.

Brown, S.P., and Hestrin, S. (2009). Intracortical circuits of pyramidal neurons reflect their long-range axonal targets. Nature *457*, 1133-1136.

Britt, J.P., Benaliouad, F., McDevitt, R.A., Stuber, G.D., Wise, R.A., and Bonci, A. Synaptic and behavioral profile of multiple glutamatergic inputs to the nucleus accumbens. *Neuron*. 2012 Nov 21;76(4):790-803.

Cardin, J.A., Carlén, M., Meletis, K., Knoblich, U., Zhang, F., Deisseroth, K., Tsai, L.H., and Moore, C.I. Driving fast-spiking cells induces gamma rhythm and controls sensory responses. *Nature*. 2009 Jun 4;459(7247):663-7.

Caputi A, Melzer S, Michael M, Monyer H (2013) The long and short of GABAergic neurons. Curr Opin Neurobiol 23:179-186.

Ciocchi, S., Passecker, J., Malagon-Vina, H., Mikus, N. & Klausberger, T. Brain computation. Selective information routing by ventral hippocampal CA1 projection neurons. *Science* 348, 560-563, doi:10.1126/science.aaa3245 (2015).

Cui, G. *et al.* Concurrent activation of striatal direct and indirect pathways during action initiation. *Nature* 494, 238-242, doi:10.1038/nature11846 (2013).

Curtis, C.E., and Lee, D. (2010). Beyond working memory: the role of persistent activity in decision making. Trends Cogn Sci *14*, 216-222.

Damasio, H., Grabowski, T., Frank, R., Galaburda, A.M., and Damasio, A.R. (1994). The return of Phineas Gage: clues about the brain from the skull of a famous patient. *Science* 5162, 1102-1105.

Dembrow, N.C., Chitwood, R.A., and Johnston, D. (2010). Projection-specific neuromodulation of medial prefrontal cortex neurons. J Neurosci *30*, 16922-16937.

Farinas, I., and DeFelipe, J. (1991). Patterns of synaptic input on corticocortical and corticothalamic cells in the cat visual cortex. I. The cell body. J Comp Neurol *304*, 53-69.

Felix-Ortiz, A. C., Burgos-Robles, A., Bhagat, N. D., Leppla, C. A. & Tye, K. M. Bidirectional modulation of anxiety-related and social behaviors by amygdala projections to the medial prefrontal cortex. *Neuroscience* 321, 197-209, doi:10.1016/j.neuroscience.2015.07.041 (2016).

Fino, E., and Yuste, R. (2011). Dense inhibitory connectivity in neocortex. Neuron *69*, 1188-1203.

Flandin P, Zhao Y, Vogt D, Jeong J, Long J, Potter G, Westphal H, Rubenstein JL (2011) Lhx6 and Lhx8 coordinately induce neuronal expression of Shh that controls the generation of interneuron progenitors. Neuron 70:939-950.

Fu, Y. *et al.* A cortical circuit for gain control by behavioral state. *Cell* 156, 1139-1152, doi:10.1016/j.cell.2014.01.050 (2014).

Funahashi, S., Bruce, C.J., and Goldman-Rakic, P.S. (1989). Mnemonic coding of visual space in the monkey's dorsolateral prefrontal cortex. J Neurophysiol *61*, 331-349.

Gabbott, P.L., Warner, T.A., Jays, P.R., and Bacon, S.J. Areal and synaptic interconnectivity of prelimbic (area 32), infralimbic (area 25) and insular cortices in the rat. *Brain Res*. 2003 Dec 12;993(1-2):59-71.

Gee, S., Ellwood, I., Patel, T., Luongo, F., Deisseroth, K., and Sohal, V.S. (2012). Synaptic activity unmasks dopamine D2 receptor modulation of a specific class of layer V pyramidal neurons in prefrontal cortex. J Neurosci *32*, 4959-4971.

Gunaydin, L. A. *et al.* Natural neural projection dynamics underlying social behavior. *Cell* 157, 1535-1551, doi:10.1016/j.cell.2014.05.017 (2014).

Han S, Tai C, Westenbroek RE, Yu FH, Cheah CS, Potter GB, Rubenstein JL, Scheuer T, de la Iglesia HO, Catterall WA (2012) Autistic-like behaviour in Scn1a+/- mice and rescue by enhanced GABA-mediated neurotransmission. Nature 489:385-390.

Hangya B, Borhegyi Z, Szilagyi N, Freund TF, Varga V (2009) GABAergic neurons of the medial septum lead the hippocampal network during theta activity. J Neurosci 29:8094-8102.

Hattox, A.M., and Nelson, S.B. (2007). Layer V neurons in mouse cortex projecting to different targets have distinct physiological properties. J Neurophysiol *98*, 3330-3340.

Harris, K.D., and Shepherd, G.M.G. The neocortical circuit: themes and variations. *Nature* Neuroscience. 2015 Feb;18(2):170–81.

Hoover WB, Vertes RP. Anatomical analysis of afferent projections to the medial prefrontal cortex in the rat. *Brain Struct Funct*. 2007 Sep;212(2):149-79.

Higo S, Akashi K, Sakimura K, Tamamaki N (2009) Subtypes of GABAergic neurons project axons in the neocortex. Front Neuroanat 3:25.

Jennings JH, Sparta DR, Stamatakis AM, Ung RL, Pleil KE, Kash TL, Stuber GD (2013) Distinct extended amygdala circuits for divergent motivational states. Nature 496:224-228.

Jinno S, Klausberger T, Marton LF, Dalezios Y, Roberts JD, Fuentealba P, Bushong EA, Henze D, Buzsaki G, Somogyi P (2007) Neuronal diversity in GABAergic long-range projections from the hippocampus. J Neurosci 27:8790-8804.

Kaifosh P, Lovett-Barron M, Turi GF, Reardon TR, Losonczy A (2013) Septo-hippocampal GABAergic signaling across multiple modalities in awake mice. Nat Neurosci 16:1182-1184.

Karnani, M. M. *et al.* Opening Holes in the Blanket of Inhibition: Localized Lateral Disinhibition by VIP Interneurons. *J Neurosci* 36, 3471-3480, doi:10.1523/JNEUROSCI.3646-15.2016 (2016).

Kauer, J.A., and Malenka, R.C. Synaptic plasticity and addiction. *Nat Rev Neurosci*. 2007 Nov;8(11):844-58.

Kjelstrup, K.G., Tuvnes, F.A., Steffenach, H.A., Murison, R., Moser, E.I., and Moser, M.B. Reduced fear expression after lesions of the ventral hippocampus. *PNAS* (2002) Aug 6;99(16):10825-30.

Khoshkhoo, S., Vogt, D. & Sohal, V. S. Dynamic, Cell-Type-Specific Roles for GABAergic Interneurons in a Mouse Model of Optogenetically Inducible Seizures. *Neuron* 93, 291-298, doi:10.1016/j.neuron.2016.11.043 (2017).

Krook-Magnuson, E., Varga, C., Lee, S.H., and Soltesz, I. (2012). New dimensions of interneuronal specialization unmasked by principal cell heterogeneity. Trends Neurosci *35*, 175-184.

Lammel S, Tye KM, Warden MR (2014) Progress in understanding mood disorders: optogenetic dissection of neural circuits. Genes Brain Behav 13:38-51.

Le Be, J.V., Silberberg, G., Wang, Y., and Markram, H. (2007). Morphological, electrophysiological, and synaptic properties of corticocallosal pyramidal cells in the neonatal rat neocortex. Cereb Cortex *17*, 2204-2213.

Lee AT, Gee SM, Vogt D, Patel T, Rubenstein JL, Sohal VS (2014) Pyramidal neurons in prefrontal cortex receive subtype-specific forms of excitation and inhibition. Neuron 81:61-68.

Lee, S., Kruglikov, I., Huang, Z. J., Fishell, G. & Rudy, B. A disinhibitory circuit mediates motor integration in the somatosensory cortex. *Nat Neurosci* 16, 1662-1670, doi:10.1038/nn.3544 (2013).

Lewis, D.A., Hashimoto, T., and Volk, D.W. (2005). Cortical inhibitory neurons and schizophrenia. Nat Rev Neurosci *6*, 312-324.

Little, J.P. and Carter, A.G. Subcellular Synaptic Connectivity of Layer 2 Pyramidal Neurons in the Medial Prefrontal Cortex. *Journal of Neuroscience* 12 September 2012, 32 (37) 12808-12819

Marenco, S., Stein, J.L., Savostyanova, A.A., Sambataro, F., Tan, H.Y., Goldman, A.L., Verchinski, B.A., Barnett, A.S., Dickinson, D., Apud, J.A.*, et al.* (2012). Investigation of anatomical thalamo-cortical connectivity and FMRI activation in schizophrenia. Neuropsychopharmacology *37*, 499-507.

Marin O, Rubenstein JL (2003) Cell migration in the forebrain. Annu Rev Neurosci 26:441-483.

Melzer S, Michael M, Caputi A, Eliava M, Fuchs EC, Whittington MA, Monyer H (2012) Long-range-projecting GABAergic neurons modulate inhibition in hippocampus and entorhinal cortex. Science 335:1506-1510.

Miller EK (2000) The prefrontal cortex and cognitive control. Nat Rev Neurosci 1:59-65.

Morishima, M., and Kawaguchi, Y. (2006). Recurrent connection patterns of corticostriatal pyramidal cells in frontal cortex. J Neurosci *26*, 4394-4405.

Morishima, M., Morita, K., Kubota, Y., and Kawaguchi, Y. (2011). Highly differentiated projection-specific cortical subnetworks. J Neurosci *31*, 10380-10391.

Packer, A.M., and Yuste, R. (2011). Dense, unspecific connectivity of neocortical parvalbumin-positive interneurons: a canonical microcircuit for inhibition? J Neurosci *31*, 13260-13271.

Padilla-Coreano, N. *et al.* Direct Ventral Hippocampal-Prefrontal Input Is Required for Anxiety-Related Neural Activity and Behavior. *Neuron* 89, 857-866, doi:10.1016/j.neuron.2016.01.011 (2016).

Peters, J., LaLumiere, R. T., and Kalivas, P. W. (2008). Infralimbic Prefrontal Cortex is Responsible for Inhibiting Cocaine Seeking in Extinguished Rats. *The Journal of Neuroscience*. 28(23), 6046–6053.

Petreanu, L., Huber, D., Sobczyk, A., and Svoboda, K. (2007). Channelrhodopsin-2-assisted circuit mapping of long-range callosal projections. Nat Neurosci *10*, 663-668.

Potter GB, Petryniak MA, Shevchenko E, McKinsey GL, Ekker M, Rubenstein JL (2009) Generation of Cre-transgenic mice using Dlx1/Dlx2 enhancers and their characterization in GABAergic interneurons. Mol Cell Neurosci 40:167-186.

Pfeffer, C. K., Xue, M., He, M., Huang, Z. J. & Scanziani, M. Inhibition of inhibition in visual cortex: the logic of connections between molecularly distinct interneurons. *Nat Neurosci* 16, 1068-1076, doi:10.1038/nn.3446 (2013).

Potter, G.B., Petryniak, M.A., Shevchenko, E., McKinsey, G.L., Ekker, M., and Rubenstein, J.L. (2009). Generation of Cre-transgenic mice using Dlx1/Dlx2 enhancers and their characterization in GABAergic interneurons. Mol Cell Neurosci *40*, 167-186.

Pi, H. J. *et al.* Cortical interneurons that specialize in disinhibitory control. *Nature* 503, 521-524, doi:10.1038/nature12676 (2013).

Ripke, S., Sanders, A.R., Kendler, K.S., Levinson, D.F., Sklar, P., Holmans, P.A., Lin, D.Y., Duan, J., Ophoff, R.A., Andreassen, O.A.*, et al.* (2011). Genome-wide association study identifies five new schizophrenia loci. Nat Genet *43*, 969-976.

Rudy B, Fishell G, Lee S, Hjerling-Leffler J (2011) Three groups of interneurons account for nearly 100% of neocortical GABAergic neurons. Dev Neurobiol 71:45-61.

Schiller, J., Major, G., Koester, H.J., and Schiller, Y. (2000). NMDA spikes in basal dendrites of cortical pyramidal neurons. Nature *404*, 285-289.

Seong, H.J., and Carter, A.G. (2012). D1 receptor modulation of action potential firing in a subpopulation of layer 5 pyramidal neurons in the prefrontal cortex. J Neurosci *32*, 10516-10521.

Sheets, P.L., Suter, B.A., Kiritani, T., Chan, C.S., Surmeier, D.J., and Shepherd, G.M. (2011). Corticospinal-specific HCN expression in mouse motor cortex: Ih-dependent synaptic integration as a candidate microcircuit mechanism involved in motor control. J Neurophysiol.

Shepherd GM (2013) Corticostriatal connectivity and its role in disease. Nat Rev Neurosci 14:278-291.

Shin LM, Liberzon I (2010) The neurocircuitry of fear, stress, and anxiety disorders. Neuropsychopharmacology 35:169-191.

Sierra-Mercado, D., Padilla-Coreano, N., & Quirk, G. J. (2011). Dissociable Roles of Prelimbic and Infralimbic Cortices, Ventral Hippocampus, and Basolateral Amygdala in the Expression and Extinction of Conditioned Fear. *Neuropsychopharmacology*, 36(2), 529–538. http://doi.org/10.1038/npp.2010.184

Sohal VS, Huguenard JR (2005) Inhibitory coupling specifically generates emergent gamma oscillations in diverse cell types. Proc Natl Acad Sci U S A 102:18638-18643.

Sohal VS, Zhang F, Yizhar O, Deisseroth K (2009) Parvalbumin neurons and gamma rhythms enhance cortical circuit performance. Nature 459:698-702.

Stujenske, J. M., Likhtik, E., Topiwala, M. A. & Gordon, J. A. Fear and safety engage competing patterns of theta-gamma coupling in the basolateral amygdala. *Neuron* 83, 919-933, doi:10.1016/j.neuron.2014.07.026 (2014).

Taniguchi H, He M, Wu P, Kim S, Paik R, Sugino K, Kvitsiani D, Fu Y, Lu J, Lin Y, Miyoshi G, Shima Y, Fishell G, Nelson SB, Huang ZJ (2011) A resource of Cre driver lines for genetic targeting of GABAergic neurons in cerebral cortex. Neuron 71:995-1013.

Tomioka R, Rockland KS (2007) Long-distance corticocortical GABAergic neurons in the adult monkey white and gray matter. J Comp Neurol 505:526-538.

Tomioka R, Okamoto K, Furuta T, Fujiyama F, Iwasato T, Yanagawa Y, Obata K, Kaneko T, Tamamaki N (2005) Demonstration of long-range GABAergic connections distributed throughout the mouse neocortex. Eur J Neurosci 21:1587-1600.

Tritsch NX, Ding JB, Sabatini BL (2012) Dopaminergic neurons inhibit striatal output through non-canonical release of GABA. Nature 490:262-266.

Varga, C., Lee, S.Y., and Soltesz, I. (2010). Target-selective GABAergic control of entorhinal cortex output. Nat Neurosci *13*, 822-824.

Vertes RP. Differential projections of the infralimbic and prelimbic cortex inthe rat. *Synapse*. 2004 Jan;51(1):32-58.

Wang, M., Vijayraghavan, S., and Goldman-Rakic, P.S. (2004). Selective D2 receptor actions on the functional circuitry of working memory. Science *303*, 853-856.

Wang, Y., Markram, H., Goodman, P.H., Berger, T.K., Ma, J., and Goldman-Rakic, P.S. (2006). Heterogeneity in the pyramidal network of the medial prefrontal cortex. Nat Neurosci *9*, 534-542.

Xu W, Sudhof TC (2013) A neural circuit for memory specificity and generalization. Science 339:1290-1295.

Yizhar O, Fenno LE, Prigge M, Schneider F, Davidson TJ, O'Shea DJ, Sohal VS, Goshen I, Finkelstein J, Paz JT, Stehfest K, Fudim R, Ramakrishnan C, Huguenard JR, Hegemann P, Deisseroth K (2011) Neocortical excitation/inhibition balance in information processing and social dysfunction. Nature 477:171-178.

Publishing Agreement

It is the policy of the University to encourage the distribution of all theses, dissertations, and manuscripts. Copies of all UCSF theses, dissertations, and manuscripts will be routed to the library via the Graduate Division. The library will make all theses, dissertations, and manuscripts accessible to the public and will preserve these to the best of their abilities, in perpetuity.

Please sign the following statement:

I hereby grant permission to the Graduate Division of the University of California, San Francisco to release copies of my thesis, dissertation, or manuscript to the Campus Library to provide access and preservation, in whole or in part, in perpetuity.

Author Signature

Print Form

3/30/17

Date

UCSF Publishing Agreement Form Instructions

On the UCSF Publishing Agreement Form, enter the number for this page (should be the last page of your thesis / dissertation / manuscript document) in one of the 6 highlighted areas on the form (this should be consistent with the pagination formatting properties of the remainder of your thesis / dissertation / manuscript).
For example, if the pagination occurs in the bottom center of the rest of your document, then you should either click in the bottom center highlighted box (or use your TAB key on your keyboard to advance to this location) and enter in the final page number - then click on the PRINT button on the document.

Once you have the UCSF Publishing Agreement Page printed, you will need to sign and date it - then it must be scanned and combined with the rest of your document as the final page in your PDF that you will upload to Proquest/UMI when submitting your work to the Graduate Division.